Master Thesis

Development and commissioning of MEG II Radiative Decay Counter

by

Ryoto Iwai

March, 2017

The University of Tokyo

Department of Physics, School of Science

Abstract

The MEG experiment has been searching for the lepton flavor violating process, $\mu^+ \to e^+\gamma$, which can be a clear evidence of new physics beyond the Standard Model if it is discovered. The upgrade experiment (MEG II) is currently being prepared to achieve one order higher branching ratio sensitivity $\sim 4 \times 10^{-14}$ by using the world's most intense muon beam up to $\sim 10^8 \mu^+/\mathrm{s}$ and upgraded detectors with considerably improved performance. One of the key for the upgrade is to suppress the background significantly increased with the higher muon decay rate. Radiative Decay Counter (RDC) will be newly installed in MEG II to identify the background photon from the radiative muon decay (RMD). The concept of the RDC is to detect the low momentum positron associated with RMD with two detectors installed on the beam axis at both upstream and downstream of the muon stopping target.

The downstream detector was successfully developed and the final detector was constructed and tested in the muon beam. We demonstrated the capability of the identification of the background photon from RMD. The upstream detector, which is more difficult, is still under development. The main issues such as the influence on the muon beam and the detection efficiency for the RMD positrons were studied. We concluded that the influence on the muon beam transportation and the muon stopping rate is expected to be small. We evaluated the detection efficiencies expected in various configurations and the final sensitivities for the possible scenarios.

Contents

Abstract **i**

1 Introduction **1**
1.1 Standard Model . . . 1
1.1.1 Flavor conservation . . . 1
1.1.2 Muon decay modes . . . 2
1.1.3 Neutrino oscillation and $\mu \to e\gamma$ decay . . . 3
1.2 Beyond the Standard Model . . . 3
1.3 History of $\mu \to e\gamma$ search . . . 5

2 MEG II experiment **6**
2.1 Signal and background . . . 6
2.1.1 Signal . . . 6
2.1.2 Background . . . 7
2.2 Requirements for the $\mu^+ \to e^+\gamma$ search . . . 8
2.3 Experimental apparatus . . . 9
2.3.1 Proton accelerator complex and πE5 beam line . . . 9
2.3.2 Beam transport system . . . 9
2.3.3 Target . . . 11
2.3.4 MEG II detector overview . . . 12
2.3.5 Positron Spectrometer . . . 12
2.3.6 Photon detector . . . 15
2.3.7 Radiative Decay Counter . . . 16
2.3.8 DAQ boards . . . 16
2.4 Expected performance and sensitivity . . . 17

3 Radiative Decay Counter **19**
3.1 Principle of background identification . . . 19
3.2 Concepts of the RDC detector . . . 20
3.3 Downstream detector design . . . 21
3.3.1 Timing Counter . . . 22
3.3.2 Calorimeter . . . 25
3.4 Upstream detector design . . . 28

4 Development of LYSO calorimeter **31**
4.1 Mass test of the LYSO crystals . . . 31
4.2 Afterglow . . . 32
4.2.1 Study with room light . . . 32
4.2.2 Study with β-ray source . . . 35

4.2.3 Influence on the energy resolution . . . 39
4.2.4 Discussion . . . 41
4.3 Optimization of optical coupling . . . 41

5 Commissioning of the Downstream Detector 43
5.1 Setup . . . 43
5.1.1 RDC installation . . . 44
5.1.2 BGO photon detector . . . 45
5.1.3 DAQ . . . 46
5.1.4 Signal check . . . 46
5.2 Calibration . . . 47
5.2.1 Non-linearlity of the WaveDREAM . . . 47
5.2.2 Energy scale calibration . . . 49
5.3 Data taking . . . 51
5.4 Analysis . . . 51
5.4.1 Event selection . . . 52
5.4.2 Timing coincidence of the RDC and BGO detector . . . 54
5.4.3 Energy cut with the calorimeter . . . 54
5.5 Issues and prospects . . . 56
5.5.1 Problematic channels in the timing counter . . . 56
5.5.2 Uncertainty of energy scale of the BGO detector . . . 59

6 Development of the Upstream Detector 62
6.1 Influence on the muon beam . . . 62
6.1.1 Beam spot size on the target . . . 62
6.1.2 Effect of the larger beam spot . . . 63
6.1.3 Muon stopping rate . . . 67
6.2 Effect of pileup muon . . . 68
6.2.1 Capability to distinguish two waveforms . . . 68
6.2.2 Effect of size and position of the fiber bundle . . . 71
6.2.3 Total inefficiency for RMD positrons of all bundles . . . 72
6.2.4 Prospects for reducing the inefficiency . . . 73
6.3 Total detection efficiency for RMD positrons . . . 74
6.3.1 Light yield of the scintillating fiber . . . 74
6.3.2 Detection efficiency and sensitivity in different configurations . . . 75

7 Summary and Outlook 79
7.1 Radiative Decay Counter . . . 79
7.2 Downstream detector . . . 79
7.3 Upstream detector . . . 80
7.4 Outlook . . . 80

A Characterization of SiPM 82
A.1 Principle of photon detection . . . 83
A.2 Current-Voltage curve . . . 83
A.3 Dark noise . . . 84
A.4 Crosstalk and after-pulse . . . 85
A.5 Gain . . . 86

Bibliography **86**

Acknowledgements **91**

List of Tables

1.1 Major decay modes of μ^+ in the Standard Model [3]. 2

2.1 Resolutions and efficiencies of the upgraded detector. 17

3.1 Properties of BC-418 [15]. 23
3.2 Properties of S13360-3050PE [16]. 23
3.3 Properties of the LYSO crystal. [17]. 25

4.1 Obtained parameters. 36
4.2 Fitting parameters. 39
4.3 Comparison of the parameters for different source intensities. 39

5.1 Light yields of the MiP peak of the cosmic-rays (45.4 MeV). 60
5.2 Peak of the charge distributions in two configurations. 61

6.1 Beam spot size at the target position 63
6.2 Fiducial volume parameters of the target 63
6.3 Efficiency for the signal positrons (%) 65
6.4 Hit rate in the inner most wire 66
6.5 Reconstructed momentum resolution 67
6.6 Optimal degrader thickness and muon stopping rate 68

A.1 Basic properties of S13360-1350CS [16]. V_{OP} is breakdown voltage + 3.0 V. The measurements were performed at 25 °C. 82

List of Figures

1.1 Elementary particles in the Standard Model . . . 1
1.2 Relative energy to the half of the muon mass (52.8 MeV). . . . 2
1.3 Feynman diagram of the $\mu \to e\gamma$ decay through the neutrino oscillation. . . . 3
1.4 Branching ratio of $\mu \to e\gamma$ and $\tau \to \mu\gamma$ processes [5]. m_{N3} is the mass of the right-handed Majonara neutrino. . . . 4
1.5 History of the upper limits at 90% C.L. on the muon CLFV channels [9]. The arrows represent target branching ratio sensitivities of the future experiments. Λ shows the energy scale of the new physics models. . . . 5

2.1 Signal event. . . . 6
2.2 Prompt background. . . . 7
2.3 Accidental background. . . . 7
2.4 Source of the background photons ($E_\gamma > 48$ MeV). . . . 8
2.5 Aerial view of the 590 MeV ring cyclotron [10]. . . . 9
2.6 Schematic view of the cyclotron facility and the beam lines at PSI [11]. . . . 10
2.7 Schematic view of the beam line from the πE5 channel to the MEG II detector. 11
2.8 Target in the MEG experiment. . . . 12
2.9 Schematic view of the MEG II detector. . . . 12
2.10 Schematic view and photograph of the COBRA. . . . 13
2.11 Distribution of the magnetic field. . . . 13
2.12 Schematic view of one of the cathode plane. . . . 14
2.13 Drift chamber under construction. . . . 14
2.14 Schematic view of the pixelated timing counter. Only half part is shown. . . . 14
2.15 Timing counter. Left : Single counter. Right : Assembled 128 counters before the installation. . . . 15
2.16 Liquid-xenon photon detector. Left : Cryostat. Right : Inner view after installing the PMTs and SiPMs. . . . 15
2.17 DRS chip. . . . 16
2.18 Schematic view of the waveform sampling. . . . 16
2.19 Pictures of the WaveDREAM. Left : Single board for 16 channels. Right : Crate for the boards. . . . 16
2.20 Simplified scheme of the WaveDREAM board. . . . 17
2.21 90% C.L. upper limit sensitivity as a function of DAQ time. . . . 18

3.1 Schematic view of MEG II detectors . . . 19
3.2 Expected hit time difference of the downstream RDC and the detected signal photon assuming timing resolution of 100 ps. (red) Accidental background. (blue) Positron from Michel decay. The last bin shows the events which have no hit in the RDC. . . . 20

3.3 Expected energy deposit in the downstream detector. (red) RMD with $E_\gamma > 48$ MeV. (blue) Michel decay. 20
3.4 Schematic view of the downstream detector. The timing counter is placed in front. 21
3.5 Schematic view of the downstream detector prototype. 21
3.6 Constructed downstream detector. The timing counter is visible in front. 22
3.7 Timing counter. 22
3.8 Left : PCB for a scintillator with a width of 2 cm. Right : PCB for three scintillators with a width of 1 cm. 23
3.9 Left : Plastic scintillator glued with 3 SiPMs. Right : Short and long PCBs after being wrapped with the reflector. 24
3.10 Schematic view of the setup. 24
3.11 Measured distribution of T. 24
3.12 LYSO crystals contained in a holder. 25
3.13 Decay scheme of ^{176}Lu and energy spectrum of the LYSO intrinsic radioactivity [18]. 26
3.14 PCB in the calorimeter. 26
3.15 Support structure in the calorimeter. Left : Between the crystals and the timing counter. Right : Between the crystals and the PCBs. 27
3.16 Chassis to fix the springs. 27
3.17 Aluminum cover for the light shielding. In order to prevent light leakage, black tapes are attached at the corner. 27
3.18 CG image of the upstream detector. 28
3.19 Schematic view of the MEG II detector. The upstream detector is installed between the drift chamber end cap and the COBRA end cap where a small space is available ($r \sim 20$ cm, $z \sim 2$ cm). 29
3.20 Provisional mechanical design. 30
3.21 Prototype of the bundled fibers (64 fibers $\times$2). 30

4.1 Schematic view of the setup. 31
4.2 Energy spectrum. 31
4.3 Distribution of the light yield and energy resolution. 32
4.4 Setup of the afterglow measurement with the room light. Left : 76 crystals exposed to the room light. Right : Schematic view of the setup for the current measurement. 33
4.5 Measured sensor current of the SiPM. The 76 crystals were measured according to the order of their serial numbers. Note that several serial numbers are skipped because we replaced several crystals in which we found some defects. The red and blue plots are corresponding to the results of the next measurement (Figure 4.6). 33
4.6 Measured sensor current of the SiPM and the serial number of the crystal. The red and blue plots show the result of the first and the second measurement, respectively. The order of the serial numbers corresponds to the order of the measurement. 34
4.7 Observed sensor current of the SiPM after exposing to the room light. The values over 100 μA are not recorded due to the current limitation of the power supply. 34
4.8 Schematic view of the setup. 35
4.9 The observed current of the SiPM during the β-ray irradiation. Left : Region that the current exponentially increases. Left : Whole measurement. 35

4.10 Expected number of emitted scintillation photons with afterglow (black). The red line shows the fitting with the below function. 36
4.11 Setup for the reproducibility test and the measured sensor current of the SiPM. Current jumps during irradiation are due to a technical problem of the power supply. 37
4.12 Examples of fitting. 37
4.13 Sensor current of the SiPM during the irradiation with 37 MBq ^{90}Sr. The order of the figures is corresponding to the order of the measurement. 38
4.14 Left : $\Delta I_{\max}$ vs. τ. Right : $\Delta I_{\max}$ vs. measured sensor current after exposing to the room light. The black plot shows the additional measurement with serial number 28. The current with the room light was measured three times in the red plots. The error bar is the standard deviation of the three results. 39
4.15 Expected energy resolution. 40
4.16 Candidates for the optical coupling. 41
4.17 Light yield of the crystal and the over voltage of the SiPM. 42
4.18 Comparison of the grease and the pad. Left : Comparison of the light yield. The arrows represent the order of the measurement. Right : The energy resolution and the light yield. 42

5.1 Schematic view of the setup. 43
5.2 Stage of the downstream RDC. 44
5.3 Positions of the detector. 44
5.4 Feed-through PCB. 45
5.5 Detector after cabling and light shielding. 45
5.6 BGO detector. Left : 16 BGO crystals. A front cover of the crystals is not attached. Right : BGO crystal attached with the PMT. 46
5.7 WavedDREAM boards after cabling. The left half part was used for the RDC and the BGO detector. 46
5.8 Boards assignment for each detector and the gain of the pre-amplifiers. 46
5.9 Problematic channels in the timing counter (red parts). 47
5.10 Schematic view of the setup. 47
5.11 Schematic view of the input pulse. Several pulse heights were used. 48
5.12 Input pulse height and the the measured pulse height of the output waveform. . 48
5.13 Example of waveform correction (calorimeter channel). Red and black shows the waveform before and after correction, respectively. 48
5.14 Simulated energy deposit (left) and measured spectrum (right). 49
5.15 Left : Expected energy spectrum (blue). The red and the green parts show the photo-peaks of the gamma-rays and the β-decay spectrum, respectively. The Q-value of the β-decay spectrum is 1192 keV [20]. Right : Example of the measured spectrum in the single channel. 50
5.16 Measured spectrum with the ^{88}Y. 50
5.17 Simulated energy deposit (left) and measured spectrum (right). The energy scale of the measured spectrum is calibrated with the gamma-rays of ^{88}Y. 51
5.18 Total energy deposit in the BGO detector of all the triggered events. The energy scale is defined by the calibration data with the ^{88}Y. 51
5.19 Event display of the RDC and the BGO detector. The marker color and the diameter represent the hit timing and the energy deposit respectively. 52
5.20 Fiducial volume of the BGO detector (red shaded part). 53

5.21 Total energy deposit in the BGO detector. The black and red spectra shows the beam on and off data, respectively. . . . 53
5.22 Total energy deposit in the BGO detector. The blue and red part shows before and after the event selections, respectively. . . . 53
5.23 Timing difference of the BGO detector and the RDC. . . . 54
5.24 Total energy deposit in the calorimeter. . . . 54
5.25 Timing difference of the BGO detector and the RDC after the energy cut with the calorimeter($> 4\,\mathrm{MeV}$). The black and the red show the events before and after the cut, respectively. . . . 55
5.26 Schematic view of the connections in the timing counter. . . . 56
5.27 PCB (top) and SiPMs (bottom) after disassembling. The red arrows show the glued areas before disassembling. . . . 57
5.28 Reflow soldering processes. . . . 57
5.29 Schematic view of the tested counter. The length of the scintillator is 11 cm. . . . 58
5.30 Example of waveforms. . . . 58
5.31 Comparison of the light yields. The red and black show the channel 1 and 2, respectively. . . . 59
5.32 Schematic views of the setup. . . . 60
5.33 Measured spectra (channel A). . . . 60
5.34 Schematic view of the setup 61
5.35 Measured spectrum. . . . 61

6.1 RDC mockup (230 μm thick Mylar foil). . . . 62
6.2 Schematic view of the setup. . . . 62
6.3 Distribution of the muon vertex on the target. Black solid line and red dashed line represent the fiducial area of the nominal and bigger target, respectively. . . . 64
6.4 Number of hit wire cells before crossing the outer shell in the drift chamber. . . . 65
6.5 Number of hit tiles in the timing counter. . . . 65
6.6 Distribution of the hit wire ID. The last 192 wires are corresponding to the inner most wires. . . . 66
6.7 Difference of the reconstructed momentum and the true momentum in the simulation. . . . 67
6.8 Muon stopping rate with several degrader thicknesses. . . . 68
6.9 Definition of ΔT. . . . 69
6.10 Prototype detector. Left : Fiber and PCB. Right : Detector at the measurement position after light shielding. . . . 69
6.11 Examples of waveform mixing. . . . 70
6.12 Probability to find a positron signal after mixing. . . . 70
6.13 Hit distribution in the upstream RDC. . . . 71
6.14 Example of the probability of the pileup in two different positions (9 fibers bundle, $y = 2$, 4 cm). The orange area represents the high muon hit rate region. . . . 71
6.15 Probability of the pileup calculated with a step size of 250 μm 72
6.16 Distribution of the inefficiency for the RMD positrons. . . . 72
6.17 Best configuration of the bundle width. Smaller widths are used in more central regions of the detector. . . . 72
6.18 Total number of bundles and inefficiency for RMD positrons with the best bundling configuration. . . . 73

6.19 Principle of the staggered readout. When there is a pileup event in the same bundle in (b) it is distinguishable in the right side of the SiPM. 73
6.20 Distribution of the number of the photoelectrons observed at single side. 74
6.21 Simulated energy deposit of the positrons from RMD ($E_\gamma > 48\,\mathrm{MeV}$). 75
6.22 Schematic view of the transmission of the scintillation photons. 75
6.23 Calculated number of scintillation photons at the single side. The probability to detect no photons is also included in the first bin. 76
6.24 Light yields and the probabilities to detect a signal with the SiPMs. 76
6.25 Hit patterns of the muon in the standard readout. The probabilities to detect a signal are shown in the red boxes. The fraction of each conditional branch is also shown. 76
6.26 Hit patterns of the muon in the staggered readout. Details of the hit position patterns are shown in the next figure. 77
6.27 Four hit position patterns when there are muon hits within ΔT. Case A, C : Positron cannot be detected at both ends. Case B : Positron can be detected only at one end. Case D : Positron can be detected at both ends. 77
6.28 Expected detection efficiency for the RMD positrons. 78
6.29 Expected sensitivity of the MEG II experiment. 78

A.1 PCB with 36 SiPMs. 82
A.2 Schematic diagram of avalanche multiplication [23]. 83
A.3 I-V curve of the SiPM. Left : Negative bias voltage. Right : Positive bias voltage. Due to the current limitation, we did not use the software below $-1\,\mathrm{V}$, but we read the value on the display of the picoammeter. 83
A.4 Example of fitting I-V curve. 84
A.5 Dark rate vs. threshold of the discriminator with different bias voltages (at 24 °C). 84
A.6 Dark rate vs. bias voltage with different temperatures. The threshold of the discriminator was always set to the signal amplitude of the half photoelectrons. . 85
A.7 Dark rate vs. temperature with different bias voltages. 85
A.8 Spectrum of the dark noise. 86
A.9 Measured spectrum at 24 °C. The bias voltage is 53.9 V. The left peak corrrenponds to a pedestal. 87
A.10 Gain vs bias voltage with different tempertures. 87

Chapter 1

Introduction

The MEG experiment has been searching for the charged lepton flavor violating (CLFV) process, $\mu^+ \to e^+\gamma$. This chapter introduces the physics motivations of the $\mu^+ \to e^+\gamma$ search. We first review the flavor conservation in the Standard Model and decay modes of the muon in its framework. Next, the CLFV process in the new physics models are discussed. The last section describes a historical overview of the CLFV search in the muon channels.

1.1 Standard Model

1.1.1 Flavor conservation

In the modern particle physics, the Standard Model has been the most successful theory to describe the elementary particles and their interactions. Figure 1.1 summarizes the elementary particles in the Standard Model . The constituents of the matter are called fermions (particles with half integer spin), which is divided into six quarks and six leptons. The interaction of the particles are caused by four gauge bosons (particle with integer spin). In addition to these particles, the Higgs boson, which was discovered several years ago [1][2], is responsible for the masses of the particles.

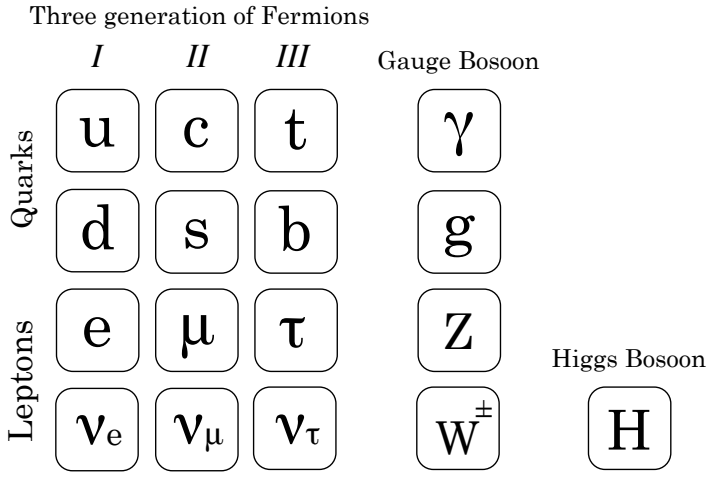

Figure 1.1: Elementary particles in the Standard Model

As shown above, the quarks and leptons are classified into the three flavor generations. In the quark sector, it is known that the flavor mixing occurred as :

$$\begin{pmatrix} d' \\ s' \\ b' \end{pmatrix} = \begin{pmatrix} V_{ud} & V_{us} & V_{ub} \\ V_{cd} & V_{cs} & V_{cb} \\ V_{td} & V_{ts} & V_{tb} \end{pmatrix} \begin{pmatrix} d \\ s \\ b \end{pmatrix}, \tag{1.1}$$

where (d', s', b') represents the flavor eigenstates vector and (d, s, b) represents the mass eigenstates of each quark. The mixing angle is described by the unitary matrix V, which is called Cabibbo-Kobayashi-Maskawa (CKM) matrix. The probability of the transition can be written as the square of the matrix element. In the Standard Model, it is considered that the flavor violation in the lepton sector is forbidden. This is because the neutrinos are massless and their mixing matrix is thereby diagonal. Thus, the $\mu^+ \to e^+\gamma$ is not allowed.

1.1.2 Muon decay modes

In the Standard Model, the decay of the muon is induced only by electroweak interactions. Decay modes of the μ^+ are listed in the Table 1.1. The decay modes of the μ^- can be expressed by conjugating their electric charges.

Decay mode	Branching ratio
$\mu^+ \to e^+\overline{\nu}_\mu\nu_e$	$\sim 100\%$
$\mu^+ \to e^+\overline{\nu}_\mu\nu_e\gamma$	$(1.4 \pm 0.4)\%$

Table 1.1: Major decay modes of μ^+ in the Standard Model [3].

The most dominant decay mode ($\mu^+ \to e^+\overline{\nu}_\mu\nu_e$) is called Michel decay. Another process ($\mu^+ \to e^+\overline{\nu}_\mu\nu_e\gamma$) is called Radiative Muon Decay (RMD), which can be regarded as an inner bremsstrahlung process of the Michel decay. Their contributions to the high energy positrons and photons are important in $\mu^+ \to e^+\gamma$ search. Figure 1.2 shows the energy spectra of the positrons from Michel decay and the photons from RMD.

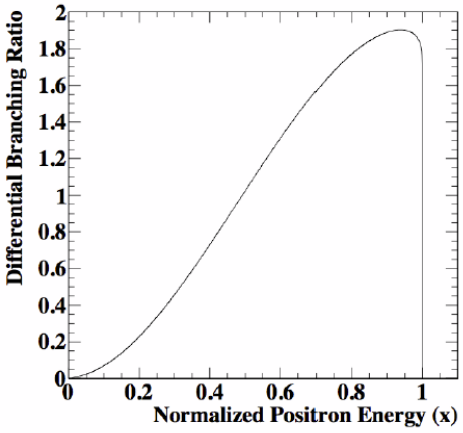

(a) Positrons from Michel decay

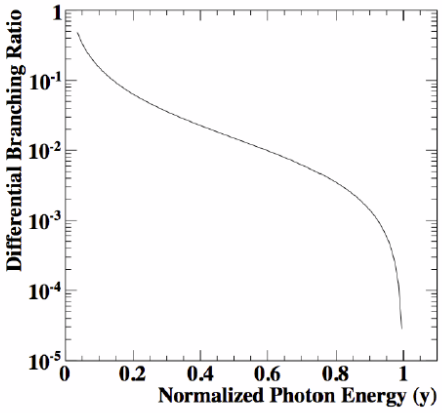

(b) Photons from RMD

Figure 1.2: Relative energy to the half of the muon mass (52.8 MeV).

1.1.3 Neutrino oscillation and $\mu \to e\gamma$ decay

Although the flavor violation in the lepton sector is forbidden in the Standard Model, several neutrino experiments observed the violation through the neutrino oscillations. Hence, the Standard Model which assumes the massless neutrinos is regarded as incomplete. If we take the neutrino masses into account, the neutrinos flavors are mixed through the non-diagonal mixing matrix as :

$$\begin{pmatrix} \nu_e \\ \nu_\mu \\ \nu_\tau \end{pmatrix} = \begin{pmatrix} U_{e1} & U_{e2} & U_{e3} \\ U_{\mu 1} & U_{\mu 2} & U_{\mu 3} \\ U_{\tau 1} & U_{\tau 2} & U_{\tau 3} \end{pmatrix} \begin{pmatrix} \nu_1 \\ \nu_2 \\ \nu_3 \end{pmatrix}, \tag{1.2}$$

where the vector $(\nu_e, \nu_\mu, \nu_\tau)$ and (ν_1, ν_2, ν_3) are representing the flavor eigenstates and the mass eigenstates, respectively. The mixing matrix U is called Pontecorvo-Maki-Nakagawa-Sakata (PMNS) matrix. Consequently, $\mu \to e\gamma$ can occurre through the $\nu_\mu \to \nu_e$ transition as shown in Figure 1.3.

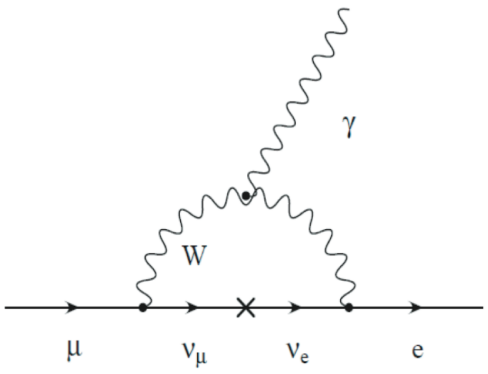

Figure 1.3: Feynman diagram of the $\mu \to e\gamma$ decay through the neutrino oscillation.

The branching ratio of the $\mu^+ \to e^+\gamma$ can be written by using the corresponding elements of the PMNS matrix as :

$$\mathscr{B}(\mu^+ \to e^+\gamma) = \frac{3\alpha}{32\pi} \left| \sum_{i=2,3} U_{\mu i}{}^* U_{ei} \frac{\Delta m_{i1}^2}{M_W^2} \right|^2, \tag{1.3}$$

where M_W is the mass of the W-boson and Δm^2 is the square neutrino mass difference. Experimentally, the neutrinos are known to have very tiny masses [4]. The branching ratio of the $\mu^+ \to e^+\gamma$ will be thereby very small ($\mathscr{B}(\mu^+ \to e^+\gamma) \sim 10^{-54}$) and it cannot be experimentally observed.

1.2 Beyond the Standard Model

Although the Standard Model has been strongly supported both experimentally and theoretically, several phenomena in the particle physics are not described in this framework. For

example, the presence of gravitational interactions, dark matter and matter-antimatter asymmetry cannot be explained with the Standard Model. It is believed that more fundamental theory of the particle physics exists and the Standard Model is just an low-energy approximation. Various scenarios of the new physics models beyond the Standard Model are considered. The grand unification theory (GUT) is a theory in which all the interactions are unified at the energy scale of $\mathcal{O}(10^{16})$ GeV. Supersymmetric model (SUSY) assumes the supersymmetric partners of each elementary particle. In these new physics models, the CLFV process are considered to be induced at a sizable rate, which is even reachable with the experiment. Therefore, searching for the charged lepton flavor violating process is equivalent to searching for an evidence of the new physics.

For example, the SUSY-SeeSaw is a model which predicts both supersymmetric particles and the tiny masses of the neutrinos by the See-Saw mechanism. Since no supersymmetric particles in the quark and lepton sector have been discovered at the same mass scale, it is considered that the SUSY is violated at the higher energy scale. In order to explain the violation, the SUSY-SeeSaw model assumes the presence of a non-diagonal mass matrixes of the supersymmetric particles, and thus, the CLFV rate is enhanced. Figure 1.4 shows the branching ratios of the CLFV processes for the several cases. Recently, relatively large neutrino mixing angle of $\theta_{13} \sim 8.4^\circ$ was measured [3]. As a consequence, the branching ratio of the $\mu \to e\gamma$ decay is more enhanced in the model. The current best upper limit of the branching ratio of the $\tau \to \mu\gamma$ decay is $\mathcal{O}(10^{-8})$. On the other hand, the branching ratio of the $\mu \to e\gamma$ decay already reaches $\mathcal{O}(10^{-13})$ as described below.

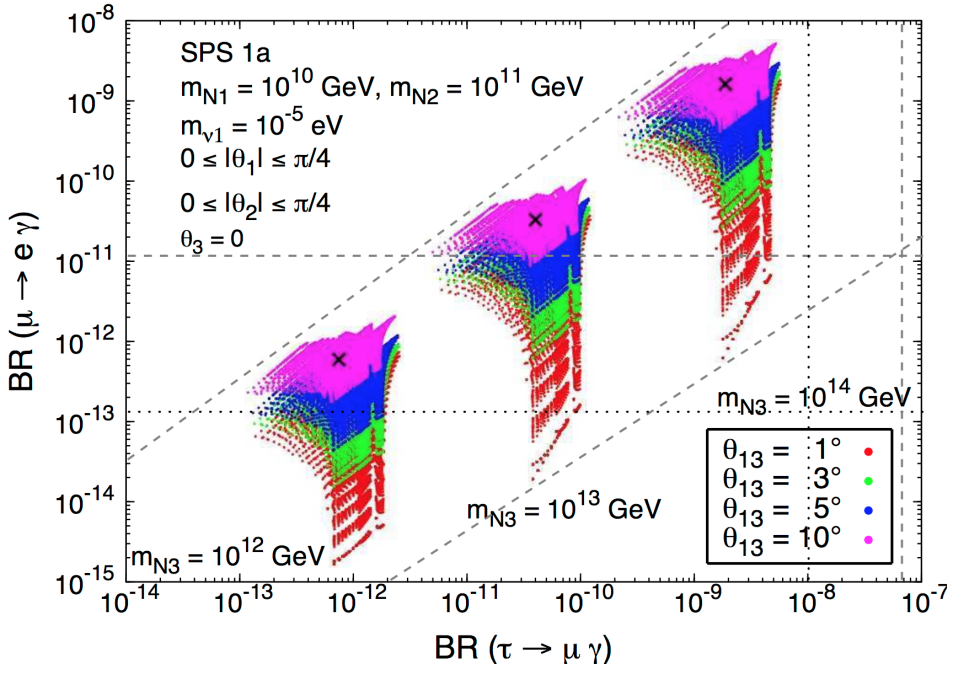

Figure 1.4: Branching ratio of $\mu \to e\gamma$ and $\tau \to \mu\gamma$ processes [5]. m_{N3} is the mass of the right-handed Majonara neutrino.

1.3 History of $\mu \to e\gamma$ search

The CLFV process has been searched for in various experiments for many decades. Particularly, the muon channels have been widely used since the way to produce a lot of muons has been established. There are also other CLFV processes induced in the new physics models such as $\mu \to eee$ or $\mu - e$ coherent conversion. Figure 1.5 shows the history of the upper limit of the branching ratio in the muon CLFV processes. The current best upper limit on the branching ratio of $\mu^+ \to e^+\gamma$ decay is $\mathscr{B} < 4.2 \times 10^{-13}$ (90% C.L.) [6]. This was set by the final result of the MEG experiment, which was performed in the period of 2008-2011 at the Paul Scherrer Institut (PSI) in Switzerland. PSI has the world's most intense μ^+ beam, which can provide 10^8 μ^+/s. In the MEG experiment, 7.5×10^{14} muons were stopped in the target in total. Currently, an upgrade experiment, called MEG II experiment, is being prepared at PSI aiming at one order higher branching ratio sensitivity of $\mathcal{O}(10^{-14})$ [8]. The details of the MEG II experiment are described in the next chapter.

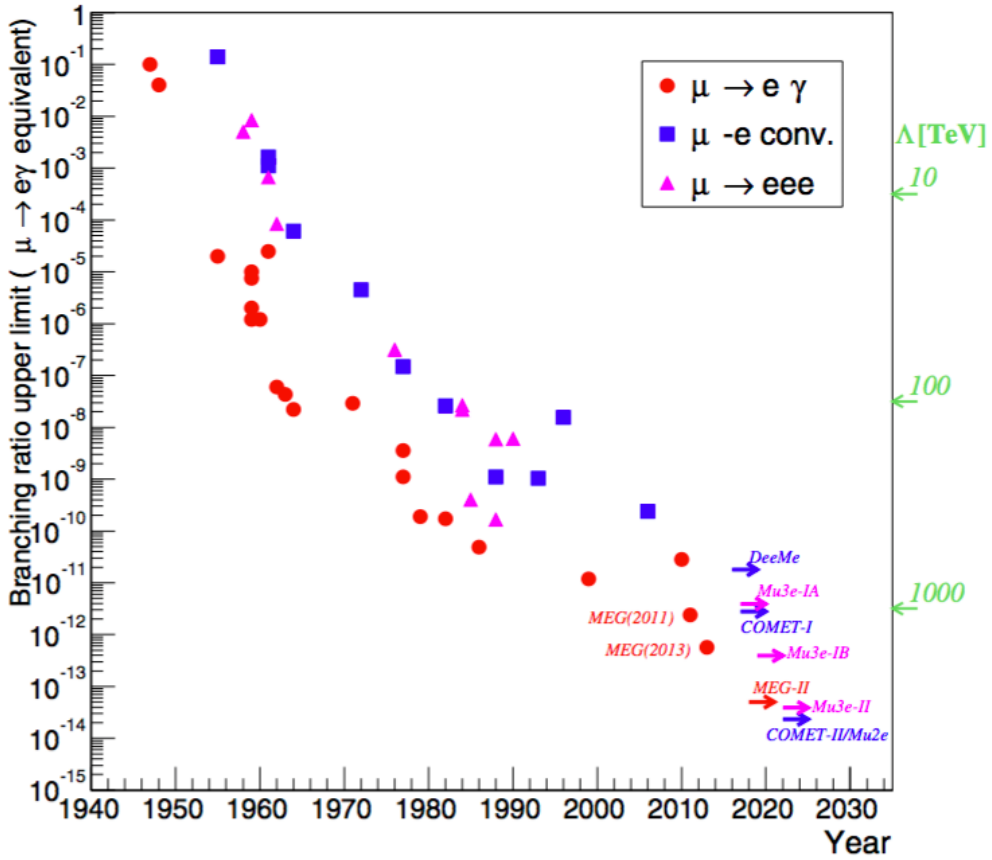

Figure 1.5: History of the upper limits at 90% C.L. on the muon CLFV channels [9]. The arrows represent target branching ratio sensitivities of the future experiments. Λ shows the energy scale of the new physics models.

Chapter 2

MEG II experiment

Currently, the preparation for the upgrade experiment (MEG II experiment) is in progress. It aims to achieve one order higher sensitivity by using the world's most intense muon beam at the PSI and detectors with significantly improved performance. This chapter first explains signatures of the signal and background events. Section 2.3 summarizes requirements for the $\mu^+ \to e^+\gamma$ search. Next, section 2.4 details the experimental apparatus of MEG II including the beam line and the detectors. The features of the upgrades from the previous experiment are also described. In the last section, the expected performance of the MEG II detectors and the sensitivity are described.

2.1 Signal and background

2.1.1 Signal

The signature of $\mu^+ \to e^+\gamma$ is a simple 2-body decay at the rest frame (Figure 2.1). A positron and a photon are emitted back-to-back ($\Theta_{e\gamma} = 180°$) and coincident in time ($t_{e\gamma} = 0$). The energies of the emitted photon and positron are both equal to half of the muon mass ($E_\gamma = E_e = m_\mu/2 = 52.8\,\mathrm{MeV}$).

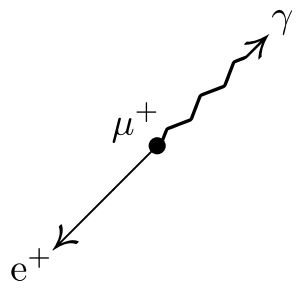

Figure 2.1: Signal event.

The expected number of signal events N_{sig} depends on the muon stopping rate on the target (R_μ) , the total acquisition time (T) and the efficiency to detect the signal (ϵ_{sig}) as shown in the following equation.

$$N_{sig} \propto R_\mu \times T \times \epsilon_{sig}$$

2.1.2 Background

There are two types of background events for the $\mu^+ \to e^+\gamma$ signal, "prompt background" and "accidental background". The prompt background is the Radiative Muon Decay (RMD ; $\mu^+ \to e^+\overline{\nu}_\mu\nu_e\gamma$) where both photon and positron carry away large energy (Figure 2.2). In the MEG II experiment, the fraction of the "The prompt background" will be smaller than that of MEG due to the improved energy resolutions of the photon and positron detectors.

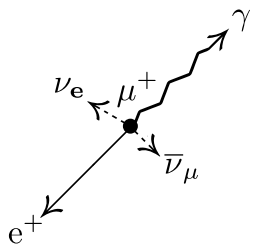

Figure 2.2: Prompt background.

Another background is the accidental coincidence of an energetic positron from Michel decay ($\mu^+ \to e^+\overline{\nu}_\mu\nu_e$) and an overlapping photon (Figure 2.3). The source of the photon is either RMD or Annihilation In Flight (AIF) of a positron.

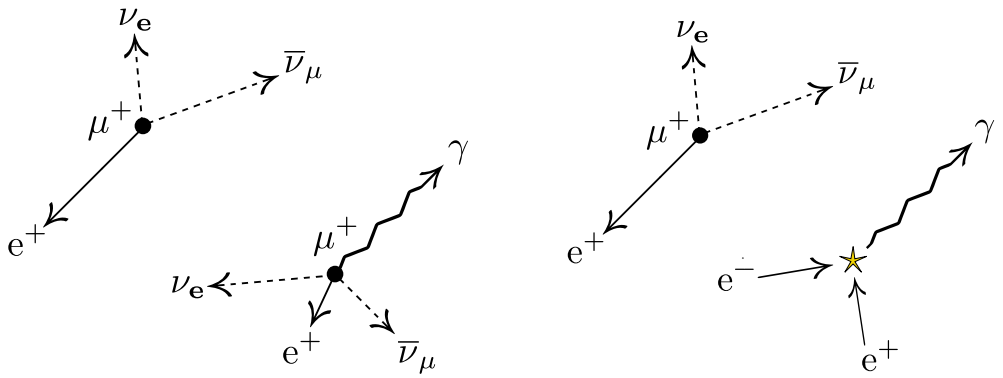

(a) Michel decay + RMD (b) Michel decay + AIF

Figure 2.3: Accidental background.

The accidental background rate is proportional to the square of the R_μ, it is thereby the most dominant background source in the MEG II experiment. The number of this background events (N_{acc}) is written as

$$N_{acc} \propto R_\mu^2 \times \Delta E_\gamma^2 \times \Delta P_e \times \Delta\Theta_{e\gamma}^2 \times \Delta t_{e\gamma} \times T$$

where $(\Delta E_\gamma, \Delta P_e, \Delta\Theta_{e\gamma}, \Delta t_{e\gamma})$ are the experimental resolutions for the photon energy, the positron momentum, the opening angle and the relative timing, respectively. Therefore, in order to distinguish the signal and the background, the good resolution of the timing, energy, and emission angle are important for both the positron and the photon detector.

Figure 2.4 describes the fraction of the gamma-ray sources in the accidental background. The two sources in the analysis region ($E_\gamma > 48$ MeV) were almost the same in the previous

experiment. On the other hand, the fraction of AIF becomes much smaller in MEG II. This is mainly due to the reduced material in the tracking volume of the new positron spectrometer (Figure 2.9). In addition, further identification of the AIF is possible in the analysis. Therefore, accidental pileup of RMD and Michel decay is the most dominant background event in the MEG II experiment.

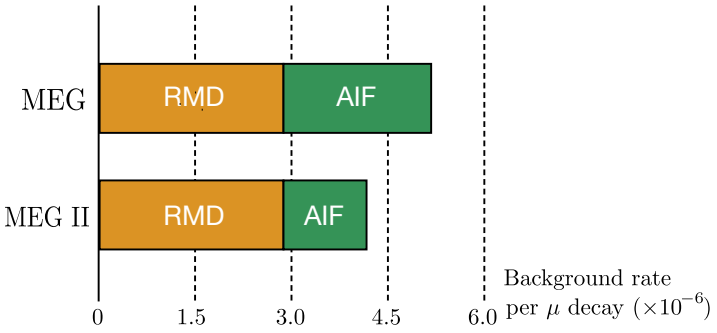

Figure 2.4: Source of the background photons ($E_\gamma > 48$ MeV).

2.2 Requirements for the $\mu^+ \to e^+\gamma$ search

In order to reach the target branching ratio sensitivity $\mathscr{B} < 4.3 \times 10^{-14}$ with three years physics data taking, it is important to have a high muon decay rate. Meanwhile, because the accidental background rate would be significantly increased due to the high muon decay rate, a pulsed muon beam is not suitable for the $\mu^+ \to e^+\gamma$ search. Moreover, negative charged muons are not suitable because they will be captured by the nuclei and will form muonic atoms. For this reason, the MEG II experiment requires a high intensity continuous positive charged muon beam. The world's most intense muon beam, which can provide $\sim 10^8 \mu^+/s$, is available at the πE5 beam line at PSI.

In the high muon decay rate environment, the suppression of the background rate is crucial. For this reason, the previous experiment was not operated with the full beam intensity ($\sim 3.0 \times 10^7 \mu^+/s$). Therefore, much better resolutions of the photon and positron detectors are required in the MEG II experiment. As shown in Figure 1.2, the energy spectrum of the background photon from RMD falls quickly near the signal energy region. Therefore, it is especially important to have a good energy resolution for the photon detector.

In order to suppress the AIF background rate, the muon stopping target and the positron spectrometer are required to have a small amount of materials. As shown in section 2.3.3, MEG II will use a thinner target by maintaining the muon stopping efficiency. Reducing the materials of the tracking volume of the spectrometer also helps to suppress the multiple scattering or the energy loss of the positrons. Moreover, the positron spectrometer has to be operational in the high decay rate positrons.

2.3 Experimental apparatus

This section details the MEG II apparatus in PSI. The high intensity muon beam at the πE5 line is produced by a proton accelerator complex. The muons are transported to the MEG II detector system (Figure 2.9) and stopped by a thin stopping target. The photons and the positrons from the $\mu^+ \to e^+\gamma$ decays are detected by a liquid xenon calorimeter and a positron spectrometer, respectively. For further improvement of the sensitivity, the MEG II experiment introduces a new detector (Radiative Decay Counter) for an active background identification

2.3.1 Proton accelerator complex and πE5 beam line

The high intensity muon beam is produced by a proton accelerator complex in following ways.

1. A Cockcroft-Walton accelerator first injects 870 keV protons into a 72 MeV cyclotron (Injector 2).
2. The protons are then injected into the 590 MeV ring cyclotron (Figure 2.5). The 590 MeV proton beam with the current of 2.2 mA is produced.
3. The protons are delivered to the pion and muon production targets (Target M and Target E). The produced particles are transported to each sub-beam lines.

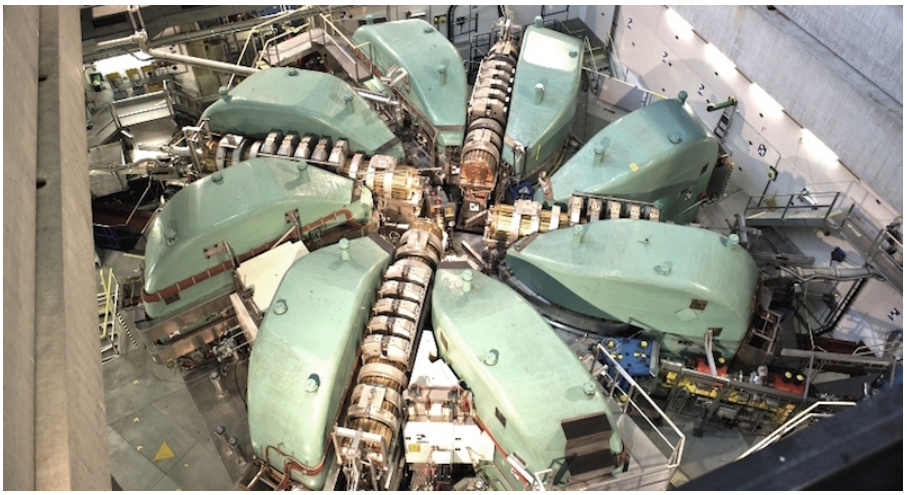

Figure 2.5: Aerial view of the 590 MeV ring cyclotron [10].

A schematic view of the cyclotron facility and the beam lines are described in Figure 2.6. The MEG II experiment uses the πE5 beam line which collects "surface" muons produced at the target E (4 cm thick graphite). The surface muons are produced from the decays of the pions stopped at the target surface Such a muon has a momentum of 29.8 MeV/c and a small momentum spread.

2.3.2 Beam transport system

The 28 MeV/c muons provided by the πE5 channel are delivered to the stopping target through the beam transport system. As shown in Figure 2.7, it consists of several components.

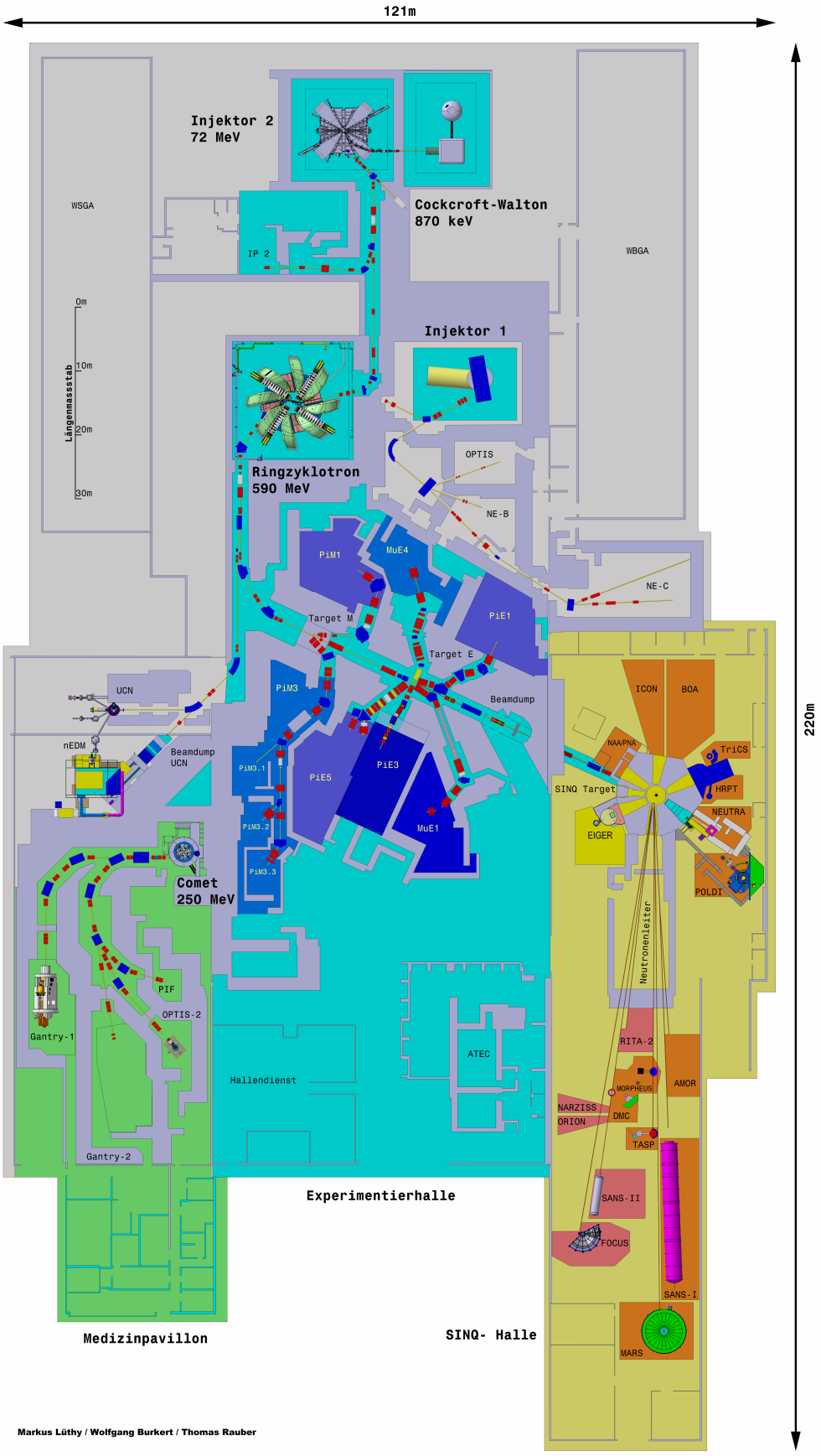

Figure 2.6: Schematic view of the cyclotron facility and the beam lines at PSI [11].

The first part is composed of two sets of quadrupole triplet magnets (Triplet I,II) and a separator sandwiched between Triplet I and II. The separator applies perpendicular electric and magnetic fields and eliminates the positron contamination. After being refocused by the Triplet II, the muons are brought to the beam transport solenoid (BTS) through a collimator. The BTS transports the muon beam to the stopping target in the COBRA spectrometer magnet. It also has a degrader made of a 300 μm thick MYLAR foil in order to reduce the muon momentum.

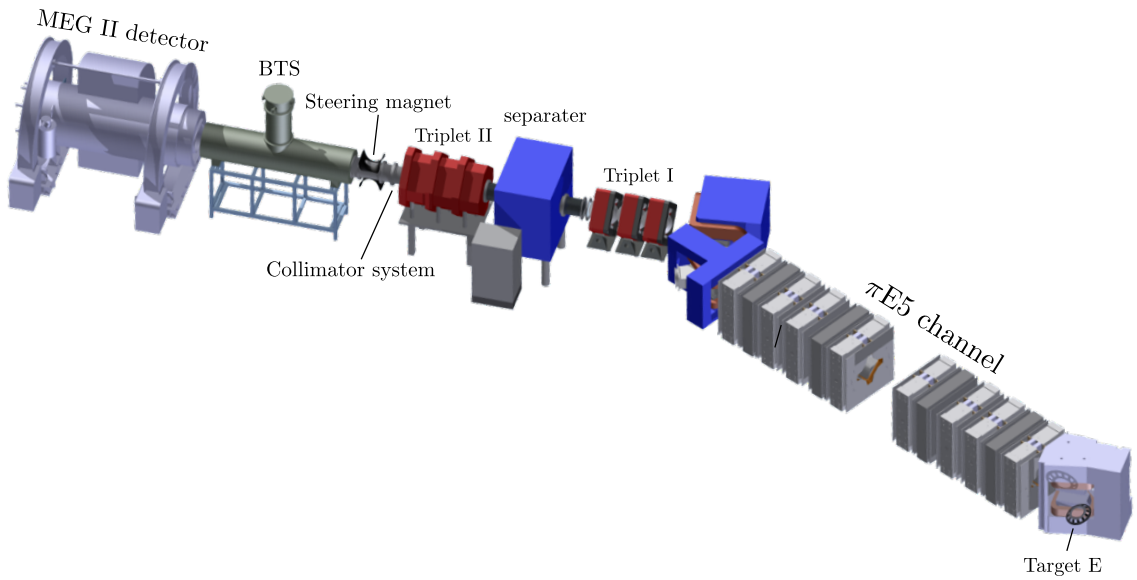

Figure 2.7: Schematic view of the beam line from the πE5 channel to the MEG II detector.

2.3.3 Target

The muon stopping target is placed inside the positron spectrometer. In the previous experiment, the target made of an ellipsoidal polyethylene-polystyrene foil (Figure 2.8). The target has the major axis of 200.5 mm and the minor axis of 79.8 mm. The thickness was 205 μm and the Rohacell frame was equipped for the mechanical support. The target had a slanted angle of 20.5° with respect to the beam axis in order to reduce the background due to the positron annihilation and to minimize multiple scattering. Moreover, the target had several holes to allow a calibration of the vertex reconstruction or an alignment of the target position.

The MEG II experiment uses a thinner target with smaller slanted angle of 15°. Since the deformation of the target was found in the previous experiment, several scenarios concerning the sizes and the materials are being considered, such as 140 μm thick polyethylene or 90 μm thick beryllium. In addition to this, a target made of a 130 μm thick scintillation film is being developed in order to monitor the muon beam profile.

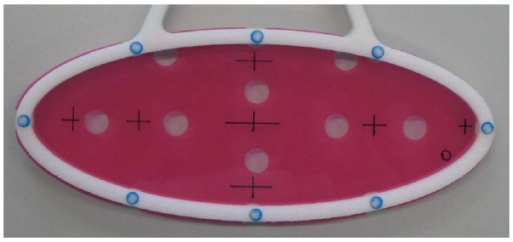

Figure 2.8: Target in the MEG experiment.

2.3.4 MEG II detector overview

The MEG detector principally consists of a liquid-xenon photon detector and a positron spectrometer. The positron spectrometer system, including a COBRA magnet, drift chamber and timing counter detects positrons. Photons are detected with a liquid-xenon photon detector. In MEG II, these detectors are upgraded. In addition, the Radiative Decay Counter is newly introduced on the beam axis.

A schematic view of the MEG II detector is shown in Figure 2.9 with the definition of the coordinate system. The positive z-axis is defined as the muon beam direction. x and y-axis are defined in accordance with a right-handed coordinate system, where the positive y-axis points upward. The distance from the z-axis is defined as r.

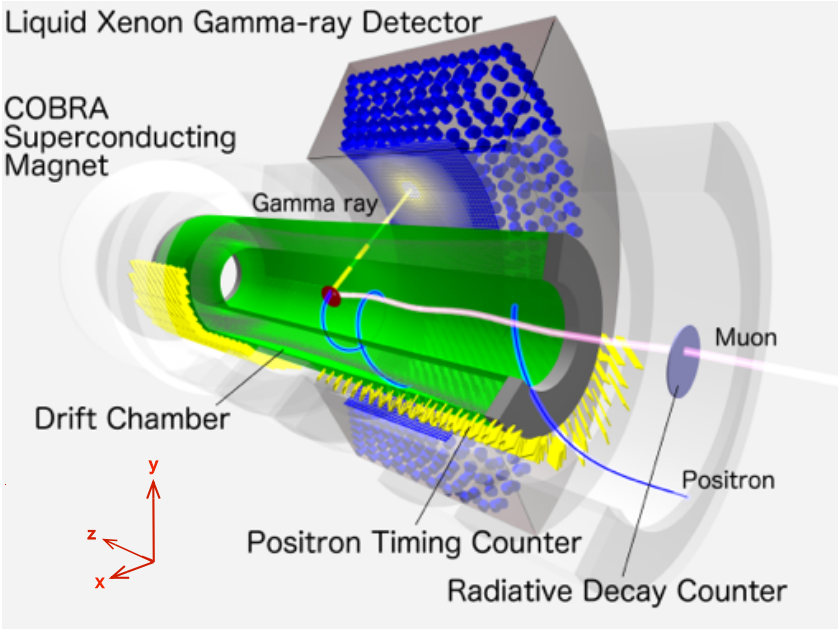

Figure 2.9: Schematic view of the MEG II detector.

2.3.5 Positron Spectrometer

The positrons are detected by the positron spectrometer which consists of several components. The two detectors are placed in a gradient magnetic filed produced by a superconducting solenoid. A cylindrical drift chamber and a pixelated timing counter detects the track and the timing of the positrons, respectively. The detail of each component is described in the following section.

A. COBRA magnet

The COBRA (COnstant Bending RAdius) magnet is a superconducting magnet with a gradient magnetic field specially developed for the MEG experiment (Figure 2.10). The total length is 2.8 m along the beam axis. In order to produce the gradient magnetic field, it consists of five coils with the three different radii. Additionally, it has two compensation coils to reduce the stray magnetic field which affects stable operations of the PMTs of the liquid-xenon photon detector. The wall of the magnet made of a thin layer (0.197 X_0) in order to transmit photons emitted from the target in the warm bore of the COBRA magnet.

The produced gradient magnetic filed ranges from 1.27 T at the center to 0.49 T at the both ends (Figure 2.11). Due to the gradient magnetic field, the positrons emitted from the target are quickly swept away regardless of their emission polar angles. Only high momentum positrons can enter the drift chamber and the timing counter. Therefore, the stable operation of the positron detectors is possible with the high beam intensity..

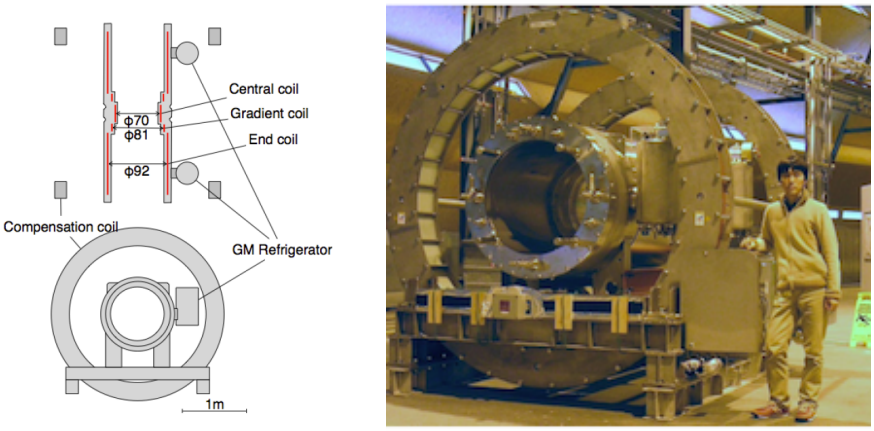

Figure 2.10: Schematic view and photograph of the COBRA.

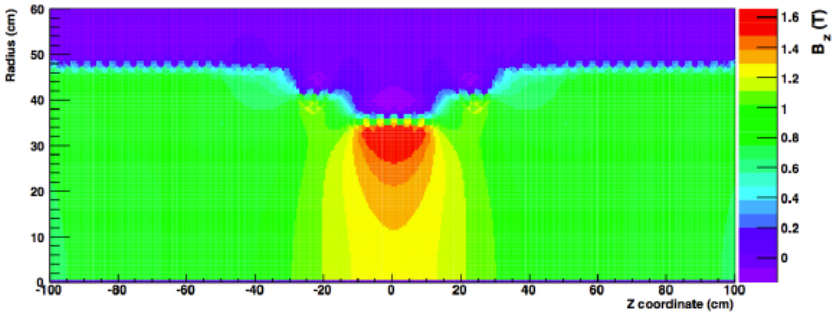

Figure 2.11: Distribution of the magnetic field.

B. Drift chamber

The tracks of the positrons are measured by the drift chamber. In the previous experiment, sixteen drift chamber modules were used. In MEG II, they will be totally replaced with a single-volume cylindrical drift chamber. The length of the new drift chamber is 193 cm along the beam axis. It consist of multiple-planes of anode and cathode wires (Figure 2.12). In total, more than 10,000 wires are used. By alternating wires with stereo angles of 6-8°, the detector is composed of ten layers of drift cells. Thanks to the small drift cells (6-9 mm), the detector can be finely segmented and reduce occupancies in the high hit rate environment. Moreover, the

detector is required to have a high transparency in order to suppress the Coulomb multiple scattering of the positrons. For this reason, the chamber gas with a very low mass mixture (helium : isobutane = 85:15) will be used. Currently, the wiring is in progress in a clean room by using a semi-automatic wiring machine (Figure 2.13).

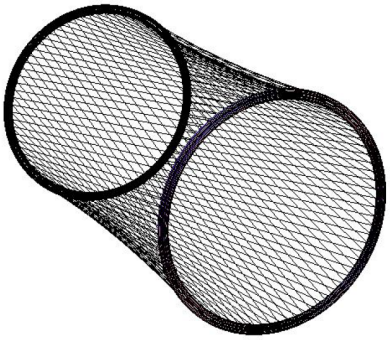

Figure 2.12: Schematic view of one of the cathode plane.

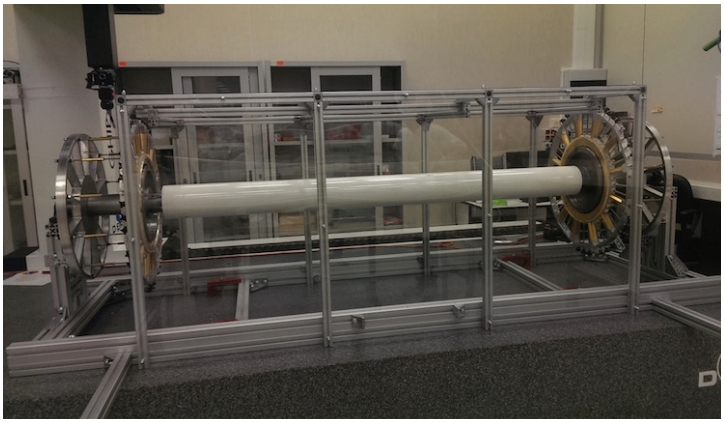

Figure 2.13: Drift chamber under construction.

C. Timing counter

Since the drift chamber is not able to measure the timing of the positrons precisely, the timing counter is placed outside of the drift chamber. In the previous experiment, 128 plastic scintillator bars with a double-side PMT readout

In the MEG II experiment, they will be replace with 512 scintillator tiles as shown in Figure 2.14. The size of the plastic scintillator tile is $100 \times (40 \text{ or } 50) \times 5\,\text{mm}^3$ typically. The scintillation light is collected at both ends with multiple-SiPMs, which are connected in series (Figure 2.15). In the laboratory test, a good timing resolutions of 60-70 ps was obtained in each counter. Moreover, the timing counter can obtain a much better timing resolution by using the multiple tile hits. In the simulation study, a single positron hits 9.2 tiles on average and an overall timing resolution of ~ 30 ps can be obtained.

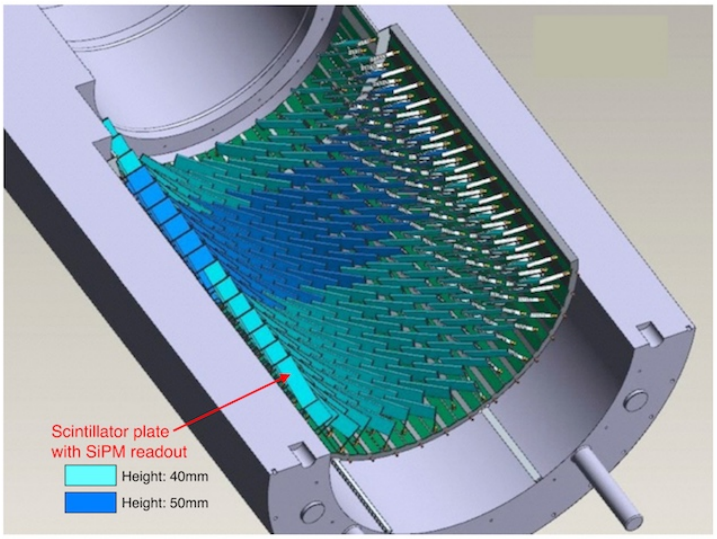

Figure 2.14: Schematic view of the pixelated timing counter. Only half part is shown.

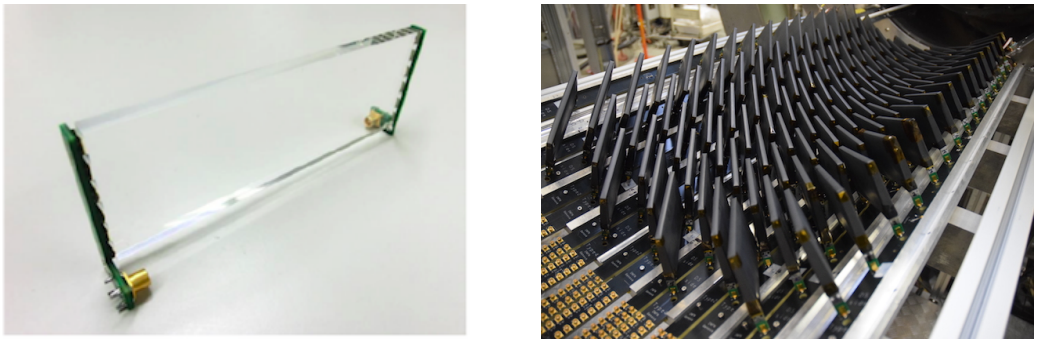

Figure 2.15: Timing counter. Left : Single counter. Right : Assembled 128 counters before the installation.

2.3.6 Photon detector

In the MEG II experiment, the liquid-xenon detector precisely measures the timing, energy and position of the 52.8 MeV signal photons Thanks to the high light yield and the fast decay time of the liquid-xenon, a good energy and timing resolution can be obtained. Moreover, the liquid-xenon is superior in terms of the high stopping power and the uniformity. The scintillation light of the liquid-xenon has a peak around 175 nm in the region of the vacuum ultra violet (VUV). Therefore, special 2-inches VUV-sensitive PMTs were developed in collaboration with Hamamatsu Photonics.

In the previous experiment, about 900 ℓ liquid-xenon was surrounded by the 846 PMTs. However, there was an issue that the energy resolution was deteriorated for the events where the photon conversion happens near the PMTs on the photon entrance face due to the position-dependent light collection efficiency

In the MEG II experiment, the 216 PMTs at the entrance face will be replaced with 4092 VUV-sensitive SiPMs, each of which has an active area of $12 \times 12\,\mathrm{mm}^2$ (Figure 2.16). The size of the single SiPM is $12 \times 12\,\mathrm{mm}^2$. Thanks to the high granularity in the entrance face, the position and the energy resolution will be improved by factor of two. The detection efficiency will be also improved by $\sim$ 10% thanks to the reduced materials of the entrance face. In addition, the photon entrance face is extended by $\sim$ 20% to reduce the energy leakage for the photons entering near the lateral faces.

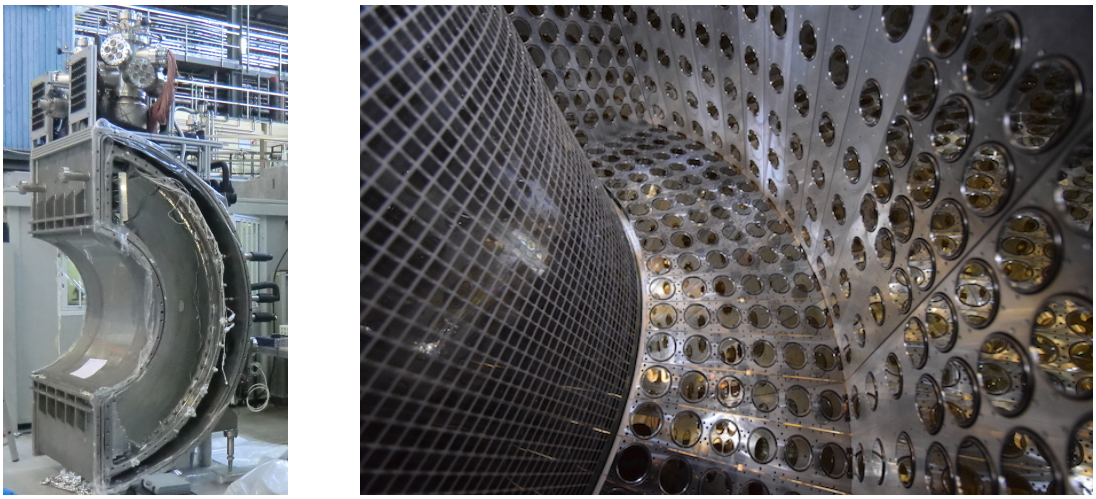

Figure 2.16: Liquid-xenon photon detector. Left : Cryostat. Right : Inner view after installing the PMTs and SiPMs.

2.3.7 Radiative Decay Counter

In addition to the upgrades of the positron spectrometer and photon detector, the Radiative Decay Counter will be newly installed for the active background identification. On the beam axis, two detectors will be installed at both upstream and downstream of the stopping target. The detail of the detector is described in the following chapter.

2.3.8 DAQ boards

The waveforms of each detector are stored in order to measure the pulse timing or charge precisely even with possible pileups at the high rate environment. For the waveform digitizer, the MEG collaboration adopted DRS4 (Domino Ring Sampler) chip, which was developed at PSI (Figure 2.17).

The principle of the waveform sampling is shown in Figure 2.18. The single DRS chip contains eight sampling channels, a channel for a clock signal and a channel for a trigger signal. In each channel, the waveform data is stored in a ring of 1024 capacitors. During the operation, the 1024 capacitors are continuously storing the waveform data at a fixed sampling frequency. The maximum sampling frequency is ∼5 GHz. When the trigger signal stops the sampling, the stored data is readout by a shift register and digitized by a commercial 12 -bits FADC.

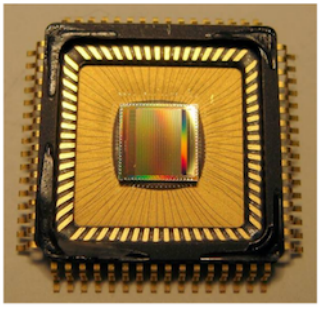

Figure 2.17: DRS chip.

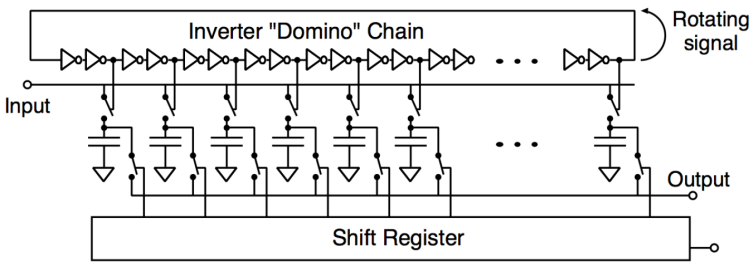

Figure 2.18: Schematic view of the waveform sampling.

The DAQ of the MEG II experiment will be also performed with the DRS chips. In order to construct a compact DAQ system for the increased number of the channels, the new DAQ board named “WaveDREAM” is adopted (Figure 2.19). As shown in Figure 2.20, the WaveDREAM combines both the waveform digitizing technology of the DRS chip and the trigger system [12]. It also contains a bias voltage supply for the SiPM, pre-amplifier and waveform shaper in each channel.

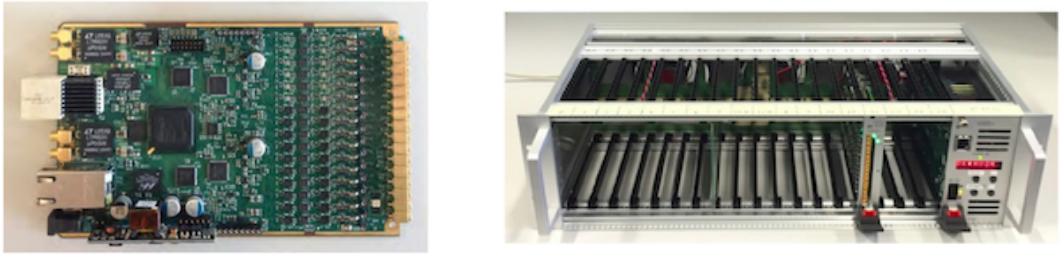

Figure 2.19: Pictures of the WaveDREAM. Left : Single board for 16 channels. Right : Crate for the boards.

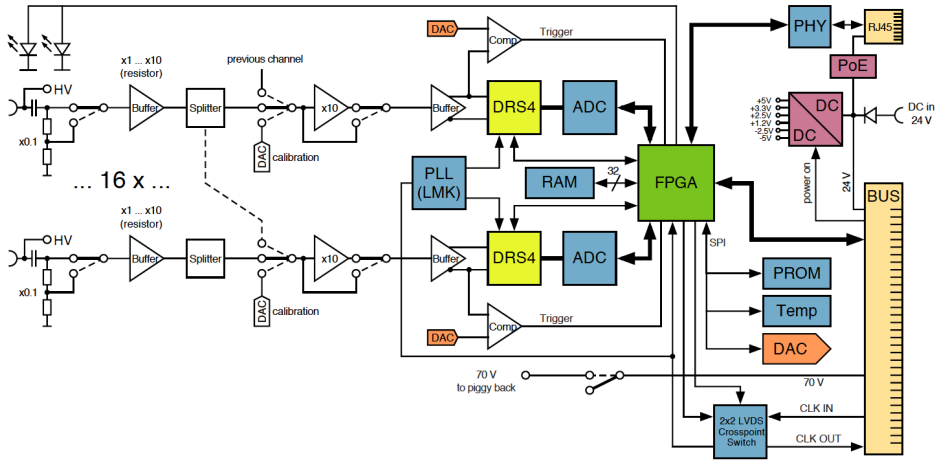

Figure 2.20: Simplified scheme of the WaveDREAM board.

2.4 Expected performance and sensitivity

The expected detector performance is summarized in the Table 5.8. Note that two energy resolutions of the photon detector are shown depending on the conversion points of the photons. The w is defined as the distance of the conversion point and the entrance face of the photon detector.

Currently, each detector is being prepared toward the engineering run in 2017. As shown in Figure 5.23, the MEG II experiment is expected to reach the sensitivity goal of $\sim 5 \times 10^{-14}$ after three years data taking.

Resolution (RMS)	MEG	MEG II
e^+ energy (keV)	306	130
e^+ vertex z position (mm)	2.4	1.6
γ energy (%) ($w < 2$ cm)	2.4	1.1
γ energy (%) ($w > 2$ cm)	1.7	1.0
γ z position (mm)	5	2.6
γ-e^+ timing (ps)	122	84
Efficiency (%)		
γ	63	69
e^+	40	88

Table 2.1: Resolutions and efficiencies of the upgraded detector.

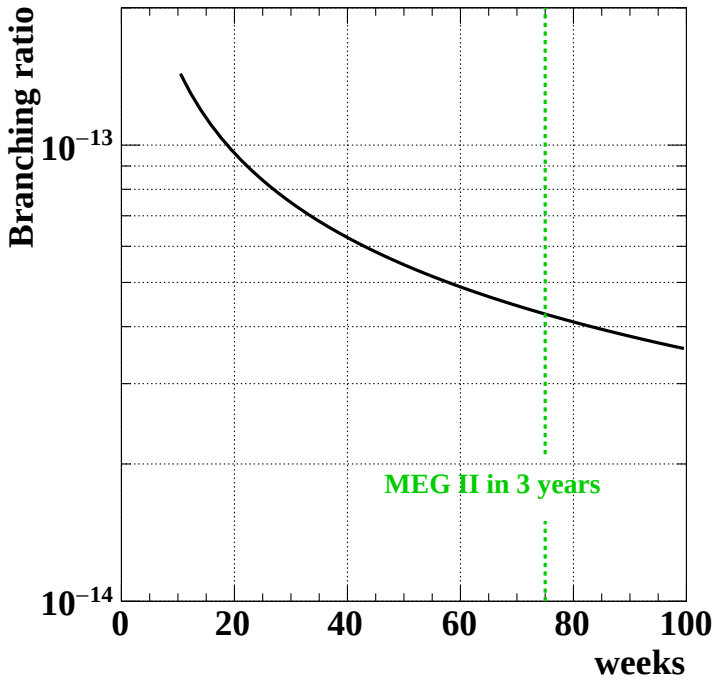

Figure 2.21: 90% C.L. upper limit sensitivity as a function of DAQ time.

Chapter 3

Radiative Decay Counter

The Radiative Decay Counter (RDC) is the new detector in the MEG II experiment which is able to improve the sensitivity by identifying significant part of the background photons from RMD. In this chapter, the detail of the RDC is described.

3.1 Principle of background identification

The concept of the RDC is illustrated in Figure 3.1. As previously mentioned, a positron emitted from the target follows a trajectory along the gradient magnetic field, which is produced by the COBRA magnet. When a high energy photon is emitted from RMD, a low momentum positron of typically 2-5 MeV is also emitted. This positron does not enter the positron spectrometer but it is swept away along the beam axis. The bending radius of these positrons are smaller than 6 cm when the energy of the gamma-ray is greater than 48 MeV. Therefore, the background photons from RMD can be identified by detecting the time-coincident low momentum positrons on the beam axis. The detectors can be installed at both upstream and downstream of the muon stopping target. Figure 3.2 shows the expected hit timing difference of the RDC and the photon detector. The timing peak in the red line is corresponding to the RMD events. The spread of the 6 ns (FWHM) mainly comes from the fluctuation of the time-of-flight of positrons. According to the simulation result, 41% of total background photons can be identified by installing two RDC detectors and thus the sensitivity is improved by 22%.

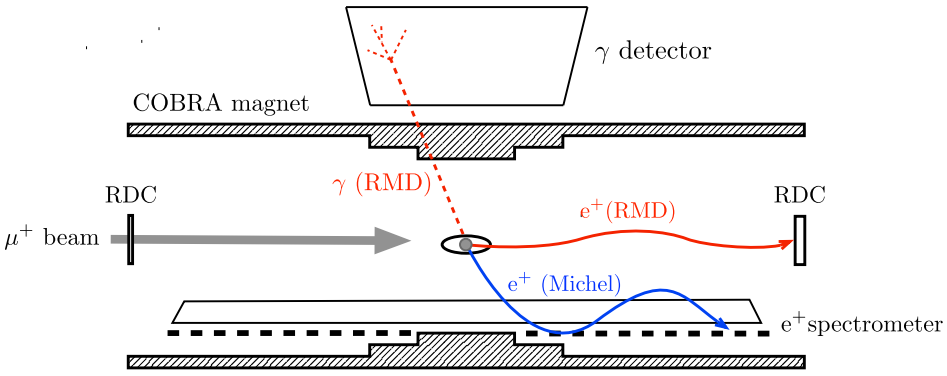

Figure 3.1: Schematic view of MEG II detectors

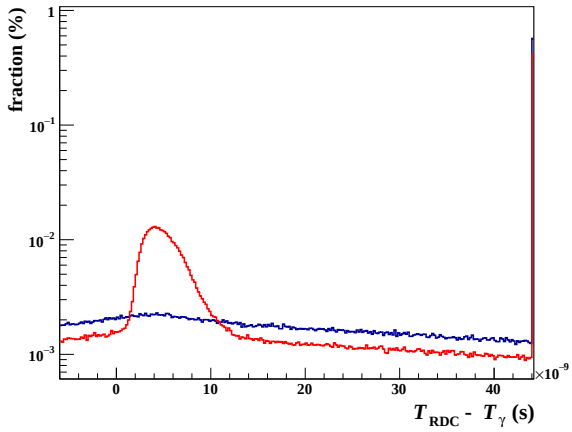

Figure 3.2: Expected hit time difference of the downstream RDC and the detected signal photon assuming timing resolution of 100 ps. (red) Accidental background. (blue) Positron from Michel decay. The last bin shows the events which have no hit in the RDC.

3.2 Concepts of the RDC detector

Because a lot of positrons from Michel decays hit each detector (∼10 MHz), it has to be operational in such a high hit rate environment. Moreover, there is a high hit rate of the beam muons in the upstream detector (∼100 MHz). The detectors thereby consist of a fast plastic scintillators which should be finely segmented in the high rate region. As a result, the large number of readout channels are required. Meanwhile, in order to be installed inside the superconducting solenoid, the size of the detector has to be as compact as possible (∼20 cm). For this reason, the scintillation light is collected by using a SiPM because it is small and insensitive to the magnetic field. Since pileup positrons from Michel decays are distinguishable by measuring their energies (Figure 3.3), the downstream detector also has a calorimeter based on LYSO crystals with SiPM readout. In addition to this, the upstream detector is required to have a minimum influence on the muon beam transportation. Therefore, it consists of a thin layer of scintillating fibers.

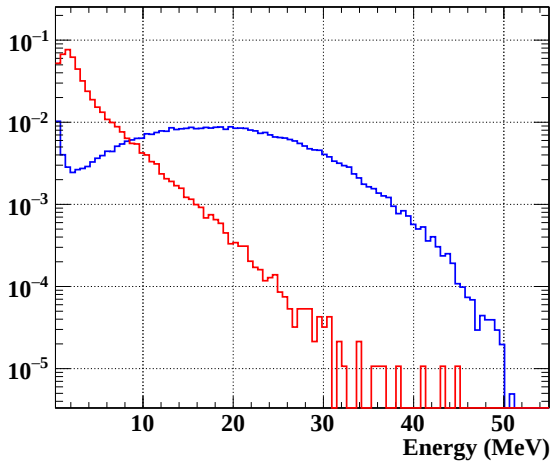

Figure 3.3: Expected energy deposit in the downstream detector. (red) RMD with $E_{\gamma} > 48$ MeV. (blue) Michel decay.

3.3 Downstream detector design

A schematic view of the downstream detector is shown in Figure 3.4. It consists of the timing counter and the calorimeter.

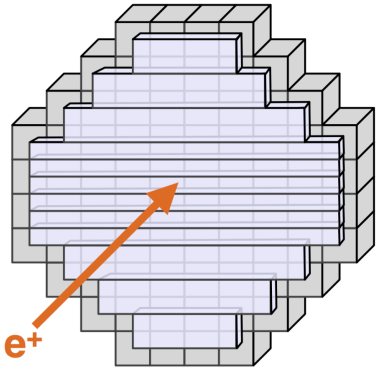

Figure 3.4: Schematic view of the downstream detector. The timing counter is placed in front.

The principle of the background identification was first demonstrated with a small prototype of the downstream detector in 2013 [13]. The prototype detector consists of two plastic scintillators and four GSO crystals (Figure 3.5). The size of the detector was ∼1/20 of the final design. It was operated with a high intensity muon beam expected in MEG II and a clear timing peak of RMD was successfully observed by triggering with the liquid-xenon detector. Because of the successful demonstration at the beam test with the prototype, the downstream detector was approved by the MEG II collaboration.

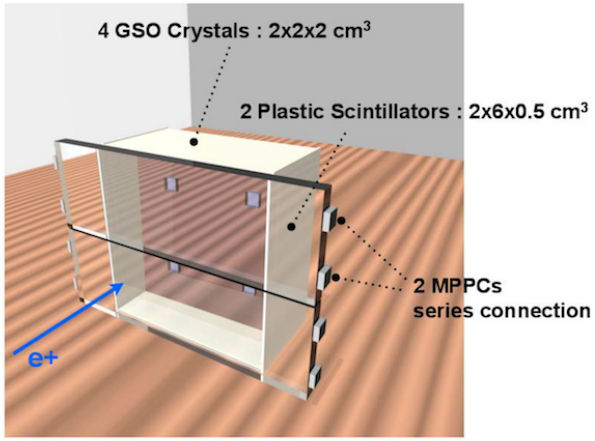

Figure 3.5: Schematic view of the downstream detector prototype.

The early work [14] reported on the development and the construction. Figure 3.6 shows the downstream detector after the construction. In order to be installed in a strong magnetic field, all of the support parts are made of non-magnetic materials such as aluminum or brass. The detail design of the timing counter and the calorimeter are described in this section. The commissioning of the downstream detector by using the high intensity muon beam is reported in chapter 5.

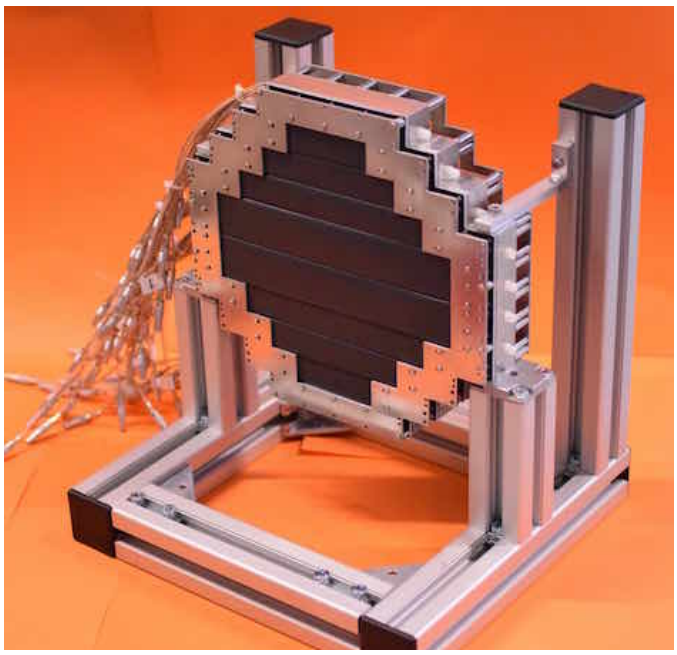

Figure 3.6: Constructed downstream detector. The timing counter is visible in front.

3.3.1 Timing Counter

The timing counter consists of 12 plastic scintillator bars with multiple-SiPM readout (Figure 3.7). Each scintillator bar has a 5 mm of thickness and several different lengths (7-19 cm). There are two types of widths (1, 2 cm) and the smaller width is used for central 6 scintillators where the hit rate is relatively high. The scintillation light is collected at the two ends by using a $3{\times}3\,\mathrm{mm}^2$ SiPM. In order to obtain a good timing resolution, it is important to collect as many scintillation photons as possible. For this reason, more than one SiPMs are used at each end. Two and three SiPMs are used at the end of 1 cm and 2 cm width scintillator bars, respectively.

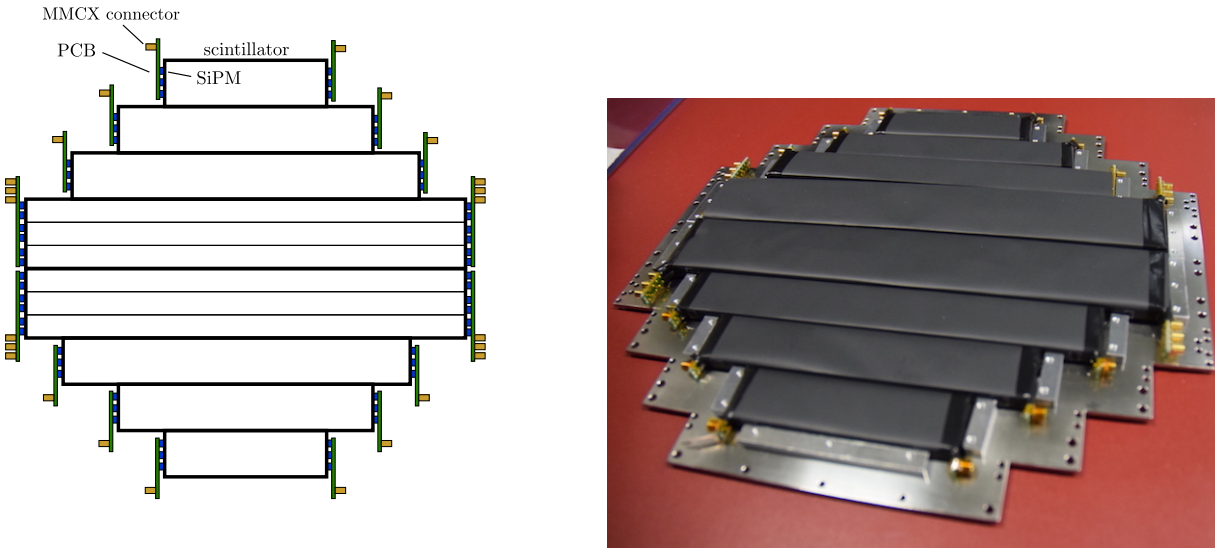

Figure 3.7: Timing counter.

In order to obtain a good timing resolution, a high light yield of the plastic scintillator is

required. For this reason, BC-418 from Saint-Gobain is selected for the plastic scintillator. This scintillator also has a very short rise and decay time (Table 3.1). For collecting the scintillation light, S13360-3050PE from Hamamatsu Photonics is selected for the SiPM because of its high photon detection efficiency and high gain (Table 3.2). The basic properties of the SiPMs are described in appendix.

Rise time	0.5 ns
Decay time	1.4 ns
Wavelength of Max. emission	391 nm

Table 3.1: Properties of BC-418 [15].

Effective area	3×3 mm^2
Pixel pitch	50 μm
Number of pixels	3600
Peak sensitivity wavelength	450 nm
Dark count	500 kHz
Gain	1.7×10^6

Table 3.2: Properties of S13360-3050PE [16].

At each end of the plastic scintillators, the SiPMs are connected in series to reduce the number of readout channels. The series connection is superior to the parallel connection in terms of the shape of the waveform. When they are connected in series, a rising time of the waveform becomes shorter thanks to smaller total capacitance of the sensor. As a result, better timing resolution can be obtained. In order to operate the series connected SiPMs properly, SiPMs in close electrical properties were grouped by measuring current-voltage response curves of all the SiPMs. Figure 3.8 shows the SiPMs mounted on the Printed Circuit Board (PCB). Six SiPMs in the central 3 scintillators are mounted on the single long PCB because of the limitation of the space. The SiPMs were mounted by using conductive epoxy (CW2400 from Circuit-Works) to avoid the possible damage due to heat during soldering. The SiPM and the scintillator were glued with optical cement (Figure 3.9). Each counter was wrapped with a reflector and light shielding.

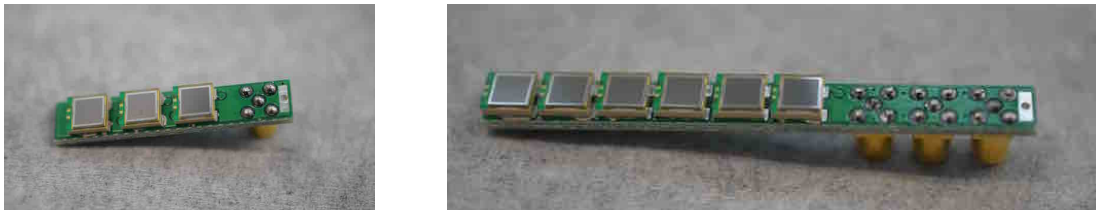

Figure 3.8: Left : PCB for a scintillator with a width of 2 cm. Right : PCB for three scintillators with a width of 1 cm.

As shown in Figure 3.10, the performance of each counter was checked by using a beta-ray source (^{90}Sr). The signal of the SiPMs were saved with a waveform digitizer (DRS4) by triggering with a small counter based on a plastic scintillator and a SiPM. The waveform data was analyzed with a software developed for MEG. The timing of the pulses are obtained with a constant fraction method, which calculates the timing where the waveform reaches the 15% of the full pulse amplitude. The timing resolution is defined as sigma of the distribution of $T = (T_{\rm L} - T_{\rm R})/2 - T_{\rm tr}$, where $T_{\rm L}$ and $T_{\rm R}$ are timing of the left and the right channel of the counter. $T_{\rm tr}$ is the timing of a trigger counter which has a 30 ps timing resolution in sigma. Figure 3.11 shows the measured distribution of the T. For each counter, the timing resolution of $\sim$90 ps was obtained, which is good enough for tagging the RMD event.

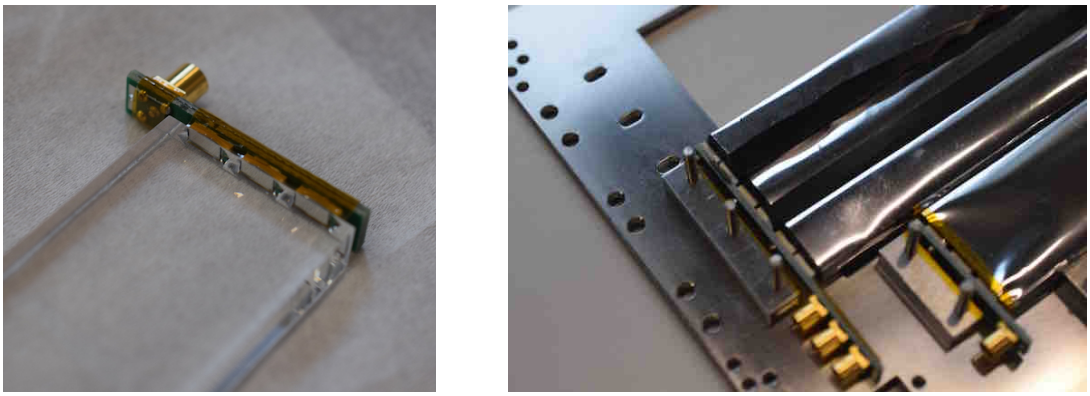

Figure 3.9: Left : Plastic scintillator glued with 3 SiPMs. Right : Short and long PCBs after being wrapped with the reflector.

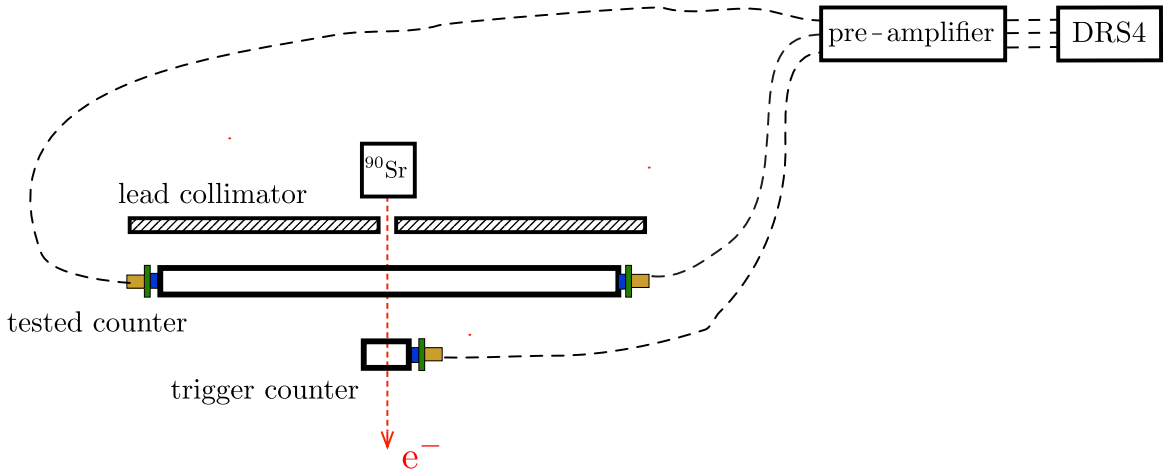

Figure 3.10: Schematic view of the setup.

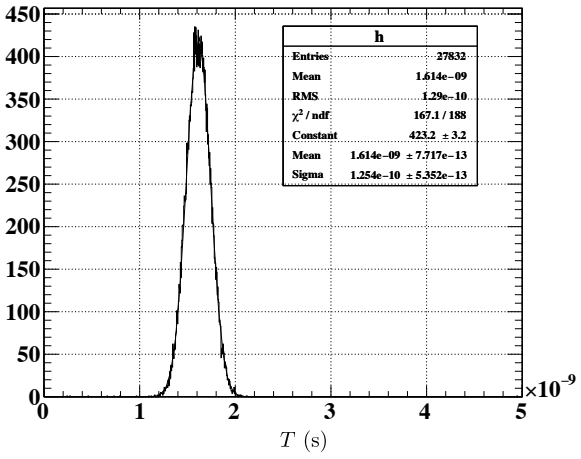

Figure 3.11: Measured distribution of T.

3.3.2 Calorimeter

The calorimeter part is placed just behind the timing counter. It consists of 76 LYSO (Lutetium Yttrium Orthosilicate) crystals (Figure 3.12). The LYSO crystal is a 20 mm cube. They were produced by Shanghai Institute of Ceramics. Each crystal was wrapped with a 65 μm thick reflector (ESR from 3M), which was produced by laser cutting.

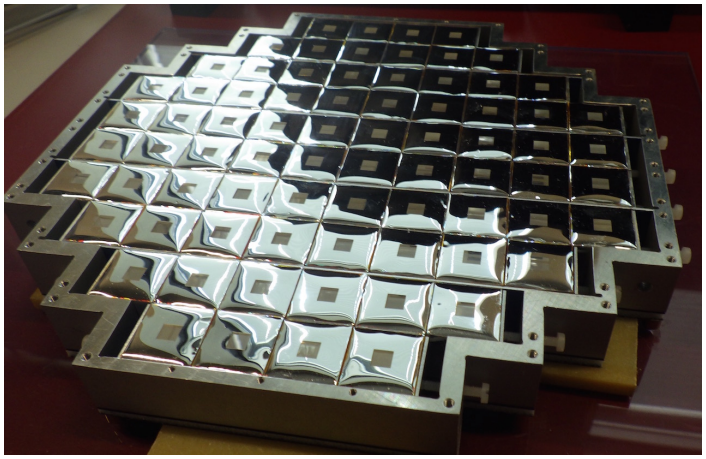

Figure 3.12: LYSO crystals contained in a holder.

The properties of the LYSO crystal are summarized in Table 3.3. It is suitable for high hit rate operation because of its short decay time. The LYSO crystal has an intrinsic radioactivity due to the contained radio isotope ^{176}Lu (2.59 % natural abundance, Figure 3.13). It has a long life time of 3.6×10^{10} years and makes an energy peak around 600 keV. Because the rate of the intrinsic radioactivities is low ($\sim$2 kHz), the accidental pileup with the positron signal would be negligible. On the other hand, the intrinsic radioactivity can be used for the energy scale calibration of each channel.

Density	7.4 g/cm^3
Radiation length	1.14 cm
Decay constant	42 ns
Emission peak	420 nm
Light yield	3×10^4 photons/MeV

Table 3.3: Properties of the LYSO crystal. [17].

Before the construction, the performances of all the crystals were measured by using a gamma-ray source (^{60}Co). The detail is described in chapter 4.1. Moreover, the LYSO crystal has a feature called afterglow, which induces an increase of the sensor current of the SiPM. Because there are large individual differences among crystals, the effect of the afterglow was investigated for all crystals. The detail is described in chapter 4.2.

Each crystal is readout with a single 3×3 mm^2 SiPM (S12572-025P from Hamamatsu Photonics). Since the saturation of the pixels would be a problem due to the high light yield of the crystals, the small pixel size of 25 μm was selected. Figure 3.14 shows one of a PCB in the calorimeter. The PCB has several flexible branches where the SiPMs are mounted. The SiPM is pressed on backside of the crystal with a spring and they are not glued for ease of maintenance.

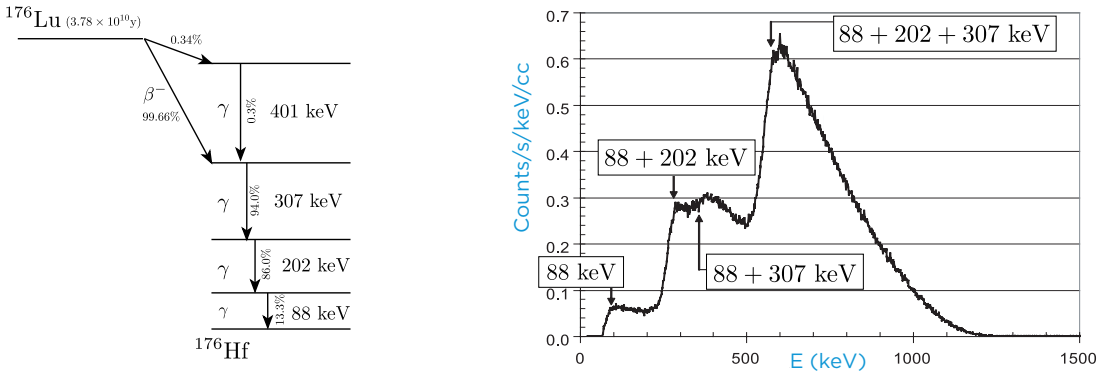

Figure 3.13: Decay scheme of ^{176}Lu and energy spectrum of the LYSO intrinsic radioactivity [18].

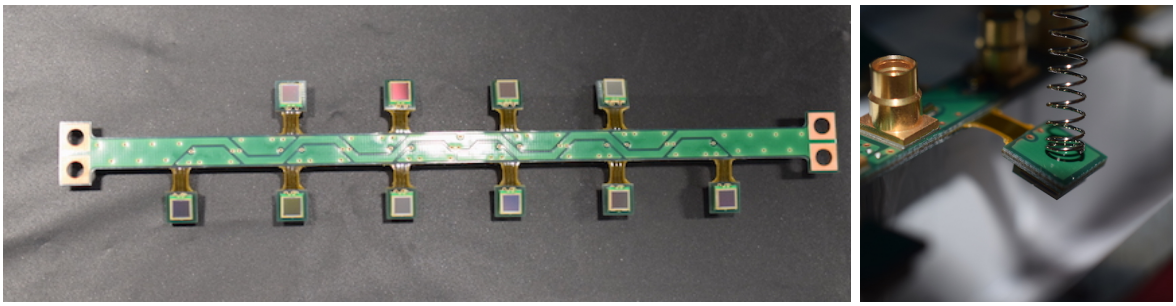

Figure 3.14: PCB in the calorimeter.

Therefore, the optical coupling of the crystals and the SiPMs need to be optimized. The detail is described in chapter 4.3.

In order to absorb the stress of the springs (∼2.5 kg in total), several support plates are inserted (Figure 3.15). The material thickness has to be as small as possible between the crystals and the timing counter. Therefore, the support plate consists of a thick Rohacell plate (3.3 mm) and two thin carbon fiber plates (CFRP : 0.2 mm × 2). In addition, a thin aluminum plate (0.1 mm) is inserted for the light shield of the crystals. On the other side of the crystals, a carbon fiber plate and two Derlin plates are inserted.

The springs are fixed on a chassis (Figure 3.16). After cabling, all the cables are fixed on the chassis not to touch the springs. For light shielding, an aluminum holder is equipped to cover the whole calorimeter (Figure 3.17).

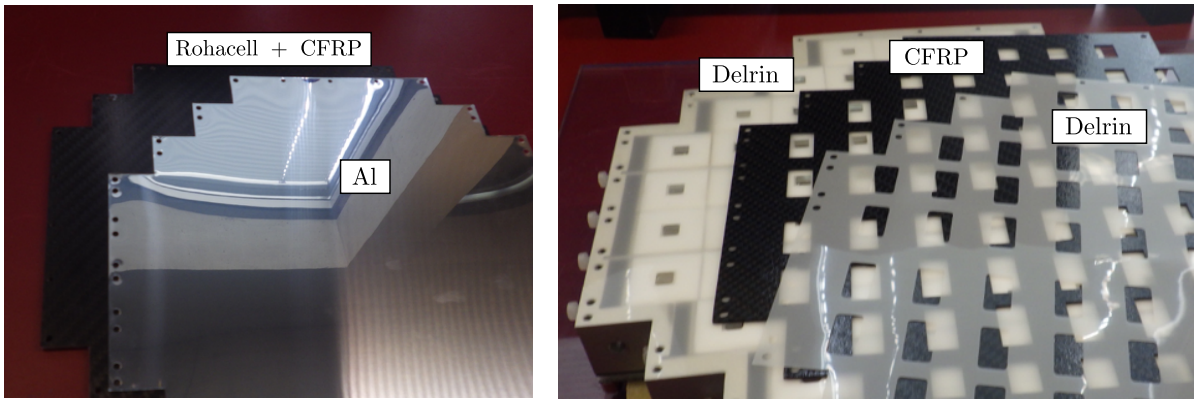

Figure 3.15: Support structure in the calorimeter. Left : Between the crystals and the timing counter. Right : Between the crystals and the PCBs.

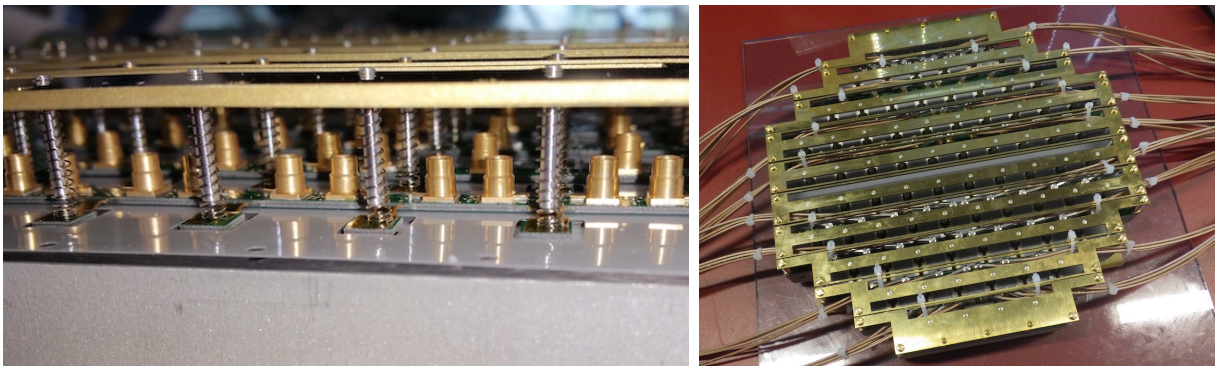

Figure 3.16: Chassis to fix the springs.

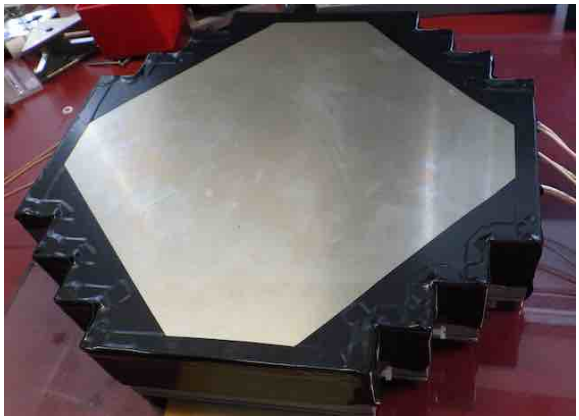

Figure 3.17: Aluminum cover for the light shielding. In order to prevent light leakage, black tapes are attached at the corner.

3.4 Upstream detector design

Presently, the installation of the upstream RDC detector has not been approved yet because it requires additional R&D concerning the operation in the high intensity muon beam ($\sim 10^8$ μ^+/s). In the provisional design, the upstream detector consists of a thin layer of scintillation fibers (Figure 3.18). We will use a double-clad square shaped scintillating fiber with a thickness of 250 μm. In order to cover the full beam pipe, about 780 fibers will be used.

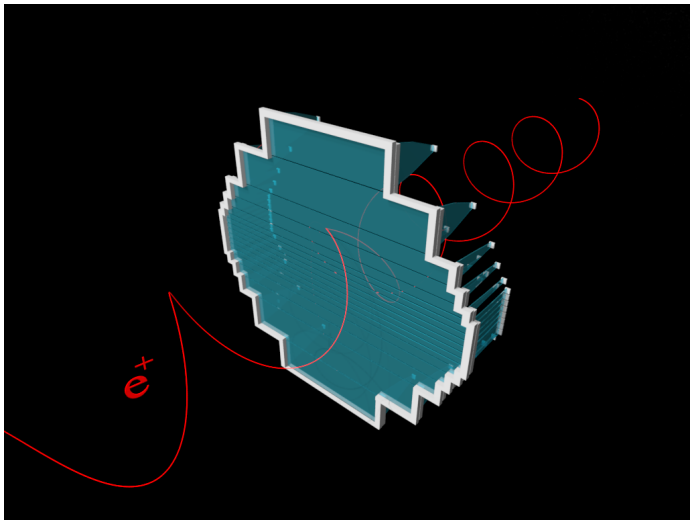

Figure 3.18: CG image of the upstream detector.

When the upstream detector is not installed, a 300 μm thick Mylar foil degrades the momentum at a beam waist in order to stop the 28 MeV/c of muons at the target. In principle, the upstream detector can be installed just by thinning the degrader. However, because it is not installed at the waist position, the upstream detector could affect the beam property.

In addition, the detection efficiency loss due to pileup beam muons is a potential issue. According to the simulation study, the hit rate of the muons is $\sim$ 500 kHz at the central fiber. To minimize the effect of the pileup, the detector has to be finely segmented in the high hit rate region. On the other hand, the upstream detector has to be installed inside a limited space as shown in Figure 3.19. Therefore, the fibers are grouped into a few tens of bundles and they are bent at right angles. Each bundle end is readout with a single SiPM. A series of the studies on above issues are reportred in chapter 6.

Figure 3.20 illustrates the provisional mechanical design of the detector with a flange of the beam pipe. Each SiPM is contained in a house in order to fix the alignment and reduce the damage due to the irradiation. Because the detector will be installed in the helium atmosphere, the signals are transmitted with feed-through connectors. In provisional design, the total number of the bundles is 18, which is limited by the available space for the readout SiPMs.

The upstream detector is desired to have a timing resolution of $\sim$500 ps in sigma by the double side readout. Figure 3.21 shows the bundle of fibers which was produced for a test. In order to make the detector as plane as possible, the fibers are glued together with optical cement by using a plane mold.

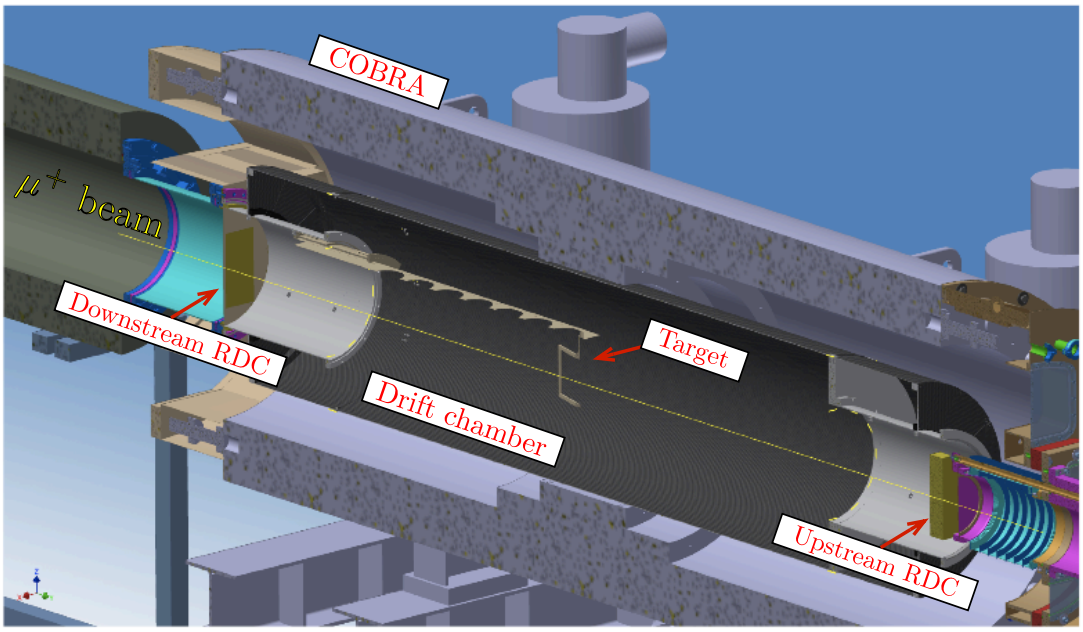

(a) Whole view of the detector

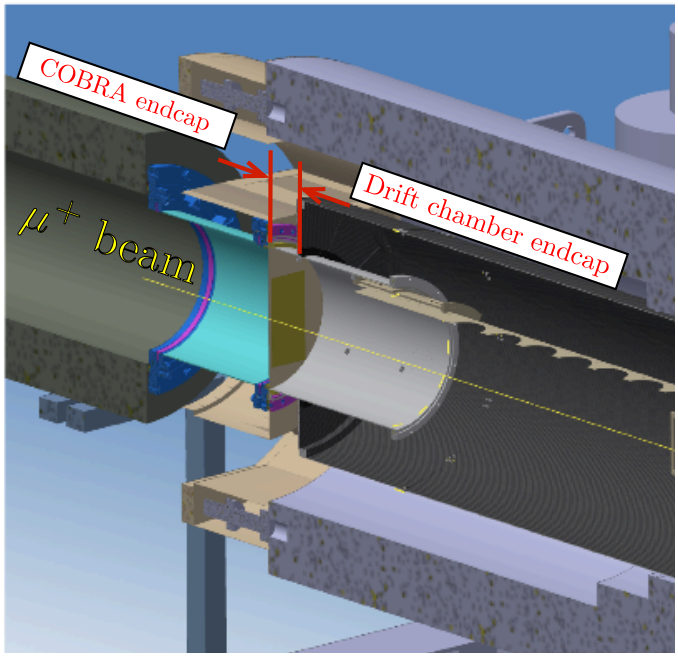

(b) Upstream side

Figure 3.19: Schematic view of the MEG II detector. The upstream detector is installed between the drift chamber end cap and the COBRA end cap where a small space is available ($r \sim 20$ cm, $z \sim 2$ cm).

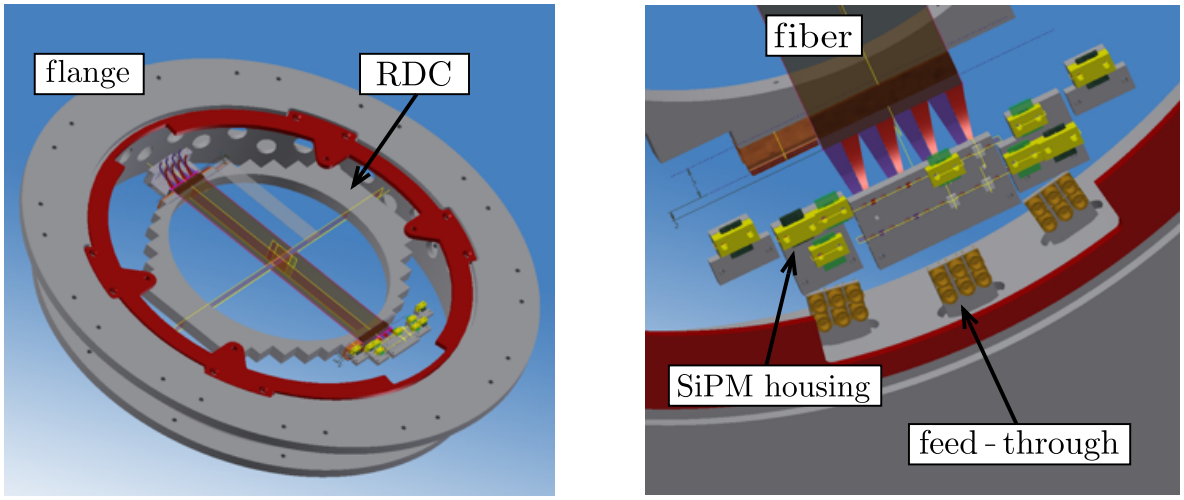

Figure 3.20: Provisional mechanical design.

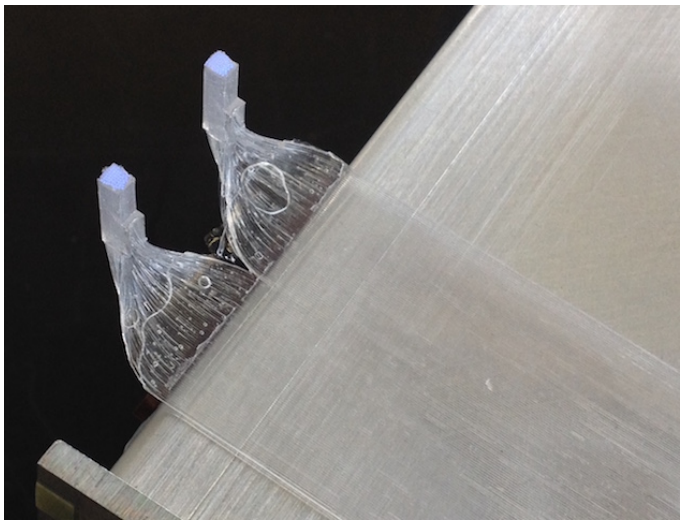

Figure 3.21: Prototype of the bundled fibers (64 fibers ×2).

Chapter 4

Development of LYSO calorimeter

Before constructing the downstream RDC, several studies on the calorimeter were required. In order to evaluate the performance of the calorimeter, we first studied on the properties of all the LYSO crystals. The light yield and energy resolution was measured one by one. During the measurement, we observed an afterglow of the crystals which is one of the features of inorganic scintillators. Since afterglow could affect the performance of the calorimeter, we studied it by using a room light and β-ray source. The details of the studies are described in section 4.2. Because the crystal and the SiPM are not glued in the calorimeter, it is necessary to optimize the optical coupling. We investigated the best way of the coupling by comparing the light yield of the crystal. The detail is summarized in section 4.3.

4.1 Mass test of the LYSO crystals

We measured the light yield and the energy resolution with all the LYSO crystals by using the setup shown in Figure 4.1. The crystals were wrapped with a reflector and tested one by one. The SiPM was fixed on the crystal by using spring pins. A gamma-ray source (^{60}Co) was set just beside the crystal. The signal of the SiPM was transmitted to a waveform digitizer (DRS4 evaluation board). Figure 4.2 shows the observed light yield spectrum. Two photo-peaks of the gamma-ray (1.17, 1.33 MeV) are overlapping with the spectrum of the intrinsic radioactivity.

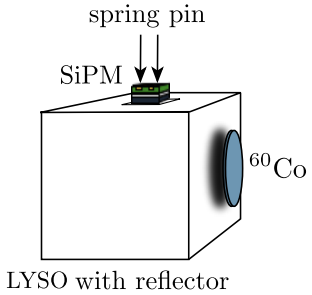

Figure 4.1: Schematic view of the setup.

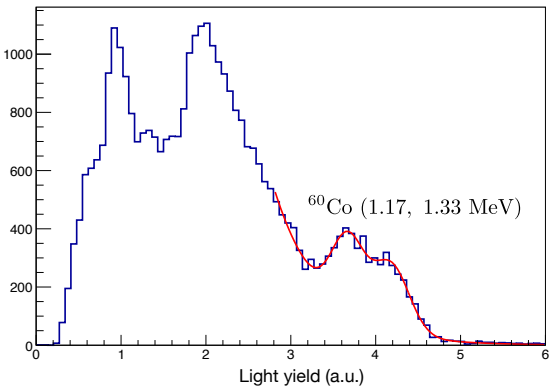

Figure 4.2: Energy spectrum.

The light yield and energy resolution were obtained by fitting the photo-peaks with gaussians in which beta-decay spectrum was convoluted. The energy resolution R was defined as $R = \sigma/E_\gamma$, where E_γ and σ are the mean and sigma of each gaussian. Figure 4.3 shows the result for the 76 crystals. Thanks to the high light yield of the crystal, good energy resolutions were obtained in most of the crystals (∼6% at 1 MeV).

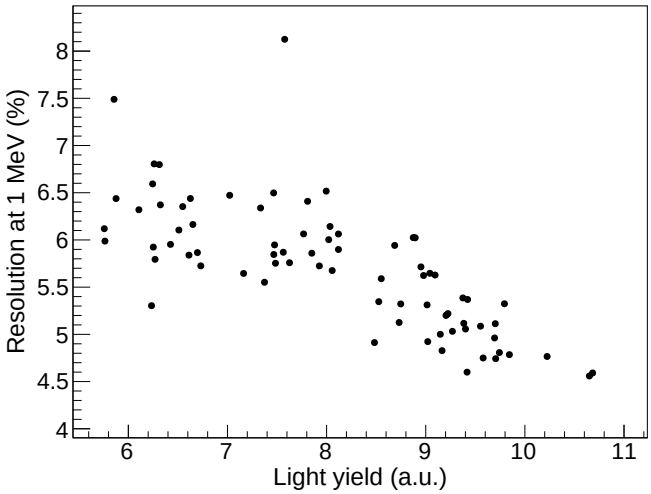

Figure 4.3: Distribution of the light yield and energy resolution.

4.2 Afterglow

During the mass test of the crystals, a large variation of a sensor current of the SiPM was observed. The reason of the variation was found to be "afterglow" of the crystal which is also called "phosphorescence" [19]. The afterglow has been observed in several types of inorganic scintillators including the LYSO. Some excited electrons in the scintillator are trapped in lattice defects, such as oxygen vacancies. Afterwards, these trapped electrons induce late scintillation photons which usually have a long time constant (typically few hours). When the crystal is exposed to a room light, a lot of electrons are excited and trapped. Therefore, the sensor current of the SiPM was significantly increased due to the large number of random scintillation photons. However, the afterglow due to exposing to the room light would not be a problem if we keep the calorimeter in a dark place before the operation. On the other hand, the afterglow due to the high hit rate of positrons (∼600 kHz at the central crystal) may not be negligible. The influence on the energy resolution needs to be properly understood.

4.2.1 Study with room light

We studied on the afterglow with the all 76 crystals by using the room light. The sensor current of the SiPM was measured with a setup shown in Figure 4.4. Before the measurement, all the crystals were kept in a dark place over 48 hours. Afterward, the crystals were placed in several rows and they were uniformly exposed to the room light over 24 hours. After exposing

to the room light, the crystals were taken out and tested one by one. We applied the bias voltage to the SiPM by using a picoammeter (Keithley, 6485) and read the sensor current. Each measurement was carried out immediately after taking out the crystal (~ 30 s).

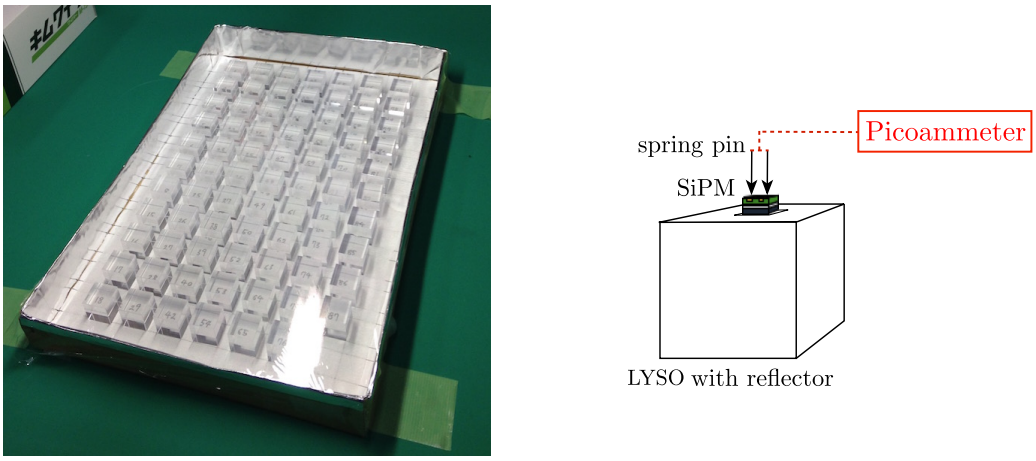

Figure 4.4: Setup of the afterglow measurement with the room light. Left : 76 crystals exposed to the room light. Right : Schematic view of the setup for the current measurement.

As a result, the large variation of the current was observed (Figure 4.5). When the crystals are kept in a dark place for long time (12 hours$\sim$), the sensor current of the SiPM would be typically a few micro-amperes. On the other hand, after exposing to the room light, the current was increased in most of the crystals. Especially several crystals induced the very large current which is over a hundred micro-amperes. It seems that the crystals in close serial numbers have similar tendency.

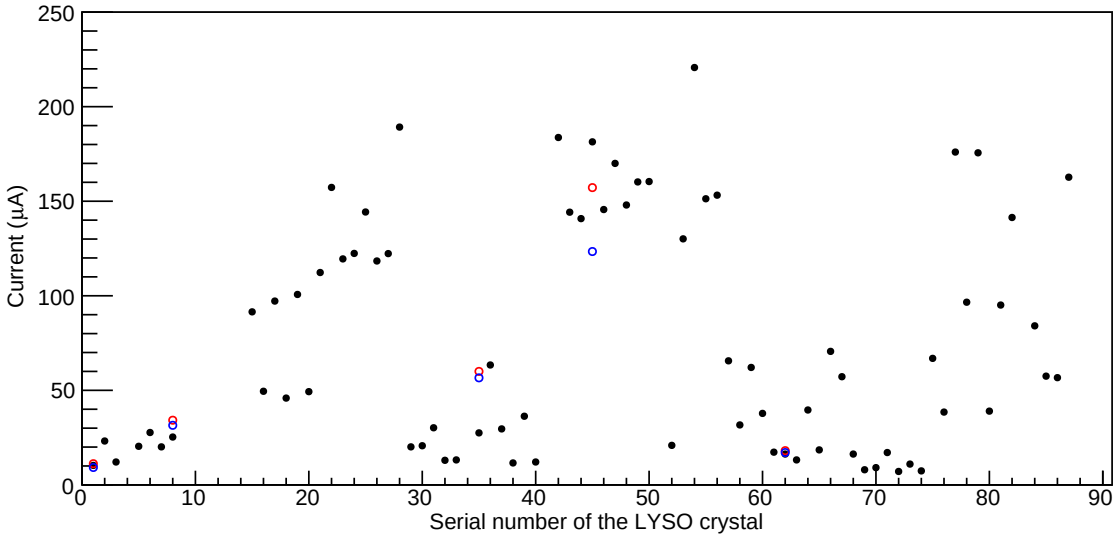

Figure 4.5: Measured sensor current of the SiPM. The 76 crystals were measured according to the order of their serial numbers. Note that several serial numbers are skipped because we replaced several crystals in which we found some defects. The red and blue plots are corresponding to the results of the next measurement (Figure 4.6).

In order to check the reproducibility, the measurement was repeated twice for the five crystals (serial number : 1, 8, 35, 45, 62) by using the same setup. In the first measurement, the

order of the measurement was 35→62→8→45→1, and it was inverted in the second measurement. The placement while exposing to the room light was also inverted in two measurements. The results show that the variation of the current values is independent of the order of the measurement (Figure 4.6). Hence, it can be seen that the current values are correlating to the production serial numbers of the crystals.

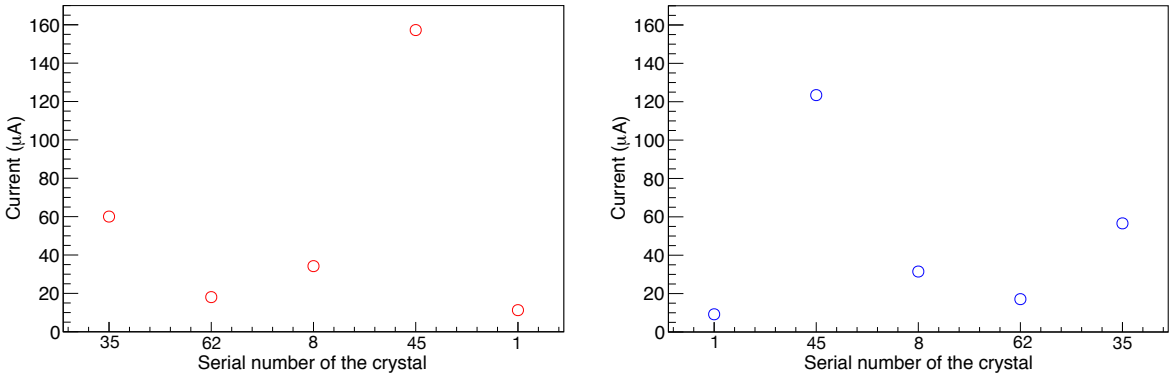

Figure 4.6: Measured sensor current of the SiPM and the serial number of the crystal. The red and blue plots show the result of the first and the second measurement, respectively. The order of the serial numbers corresponds to the order of the measurement.

We also measured how the increased sensor current changes after putting back the crystal to the dark place. This measurement was performed for the one crystal (serial number 54) in which we observed the largest current. The current was recorded every fixed period by using a power supply slot card of the SCS-2000, which is developed in PSI. As shown in Figure 4.7, we observed that the current was exponentially decreasing after stopping exposure to the room light.

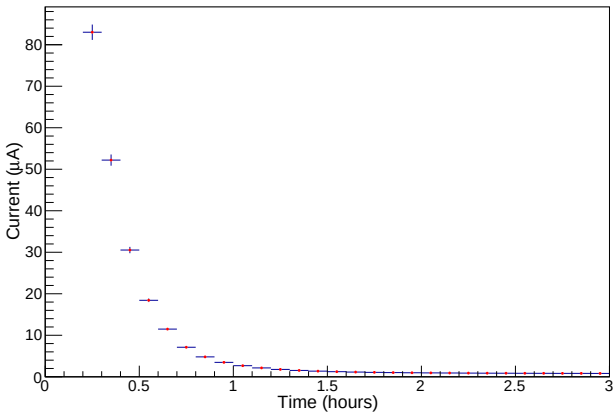

Figure 4.7: Observed sensor current of the SiPM after exposing to the room light. The values over 100 μA are not recorded due to the current limitation of the power supply.

4.2.2 Study with β-ray source

As previously mentioned, it is necessary to consider the afterglow due to the high hit rate of the positrons. In order to investigate the influence on the performance of the calorimeter, a series of measurements were performed by using a β-ray source (^{90}Sr). We firstly monitored the current during the β-ray irradiation with the one crystal (serial number 45). After keeping the setup in a dark place for long time, 3.7 MBq of ^{90}Sr was set beside the crystal and the current was monitored with the SCS2000 (Figure 4.8). During the measurement, the temperature was kept at 26 °C by using a thermal chamber. The temperature and the bias voltage of the SiPM were also monitored. The measurement was carried out for almost 20 days. As a result, we observed that the current was exponentially rising in the first few hours (Figure 4.9). Afterwards, it had kept increasing very slowly for 20 days.

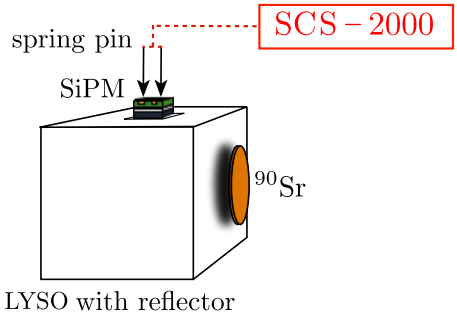

Figure 4.8: Schematic view of the setup.

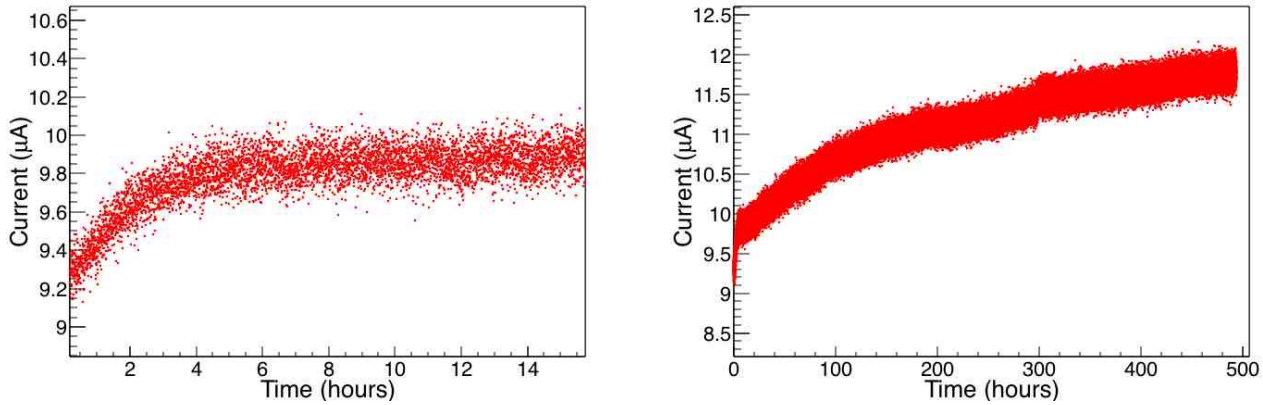

Figure 4.9: The observed current of the SiPM during the β-ray irradiation. Left : Region that the current exponentially increases. Left : Whole measurement.

On the other hand, we can expect that the number of the emitted scintillation photons will be exponentially increased with the afterglow by assuming as follows. By assuming that a certain number of electrons are excited and some of them are trapped in a time interval Δt, the time of the de-excitation follows a geometric distribution with $\Delta t \to 0$. Figure 4.10 shows the expected number of scintillation photons with this assumption. The similar behavior

was reproduced. However, the reason why the current had kept increasing for 20 days is not understood.

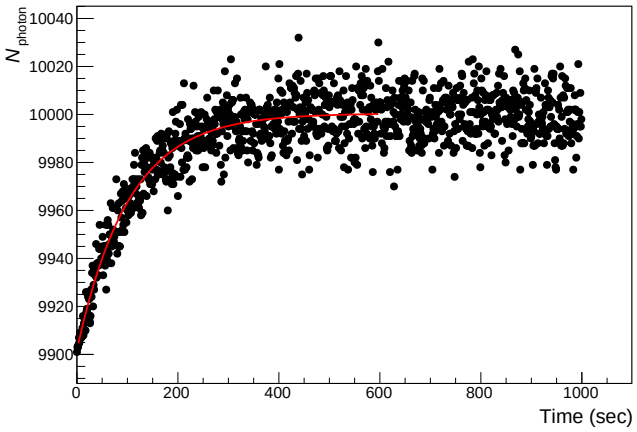

Figure 4.10: Expected number of emitted scintillation photons with afterglow (black). The red line shows the fitting with the below function.

Next, we checked the reproducibility of the current changes due to the afterglow by repeating the irradiation and shielding in turn (Figure 4.11). The same crystal (serial number 45) was used in the measurement. During the irradiation, the distance of the β-ray source and the crystal was always fixed. The β-rays were shielded by inserting a $\sim$5 mm thick lead plate between the source and the crystal. As a result, the similar behaviors were observed in each irradiation or shielding period.

For further quantitative evaluation of the result, we characterized the measured current I as a function of time t as :

$$I = \mathrm{C}_1 \pm \exp(-\frac{t - \mathrm{C}_2}{\tau}) \tag{4.1}$$

where τ and C_i are arbitrary constants. The constant τ characterizes the rise or ta time. By assuming both the rise and tail are asymptotic, the maximum variation of the current can be expressed as $\Delta I_{\mathrm{max}} = \exp(\mathrm{C}_2/\tau)$. Figure 4.12 exemplifies the fitting of the rising and tailing regions in Figure 4.12 and Table 4.1 summarizes the fitting parameters. As a result, similar τ and ΔI_{max} were obtained in either rising or tailing region.

	ΔI_{max} (μA)	τ (hours)
Irradiation	1.502 $\pm$ 0.007	1.771 $\pm$ 0.013
Shielding	-1.490 $\pm$ 0.001	1.733 $\pm$ 0.003

Table 4.1: Obtained parameters.

Finally, we checked if there were any individual differences among crystals as well as we had observed in the measurement with the room light. The current measurement during the irradiation was performed with the six crystals. Five of them had been previously measured with the room light for three times. In addition, another crystal (serial number 28) was measured. In this measurement, more powerful β-ray source (37 MBq of ^{90}Sr) was used.

(a) Irradiation (b) Sheilding

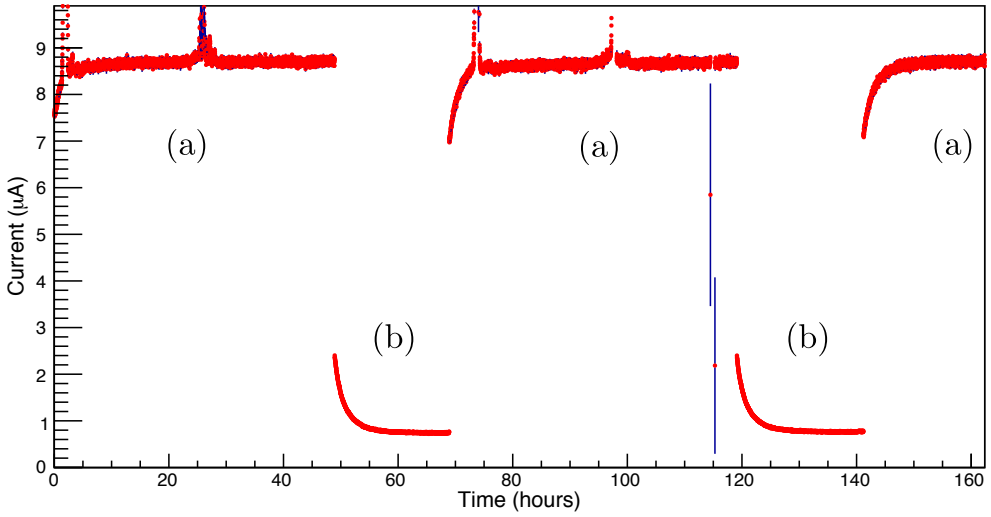

Figure 4.11: Setup for the reproducibility test and the measured sensor current of the SiPM. Current jumps during irradiation are due to a technical problem of the power supply.

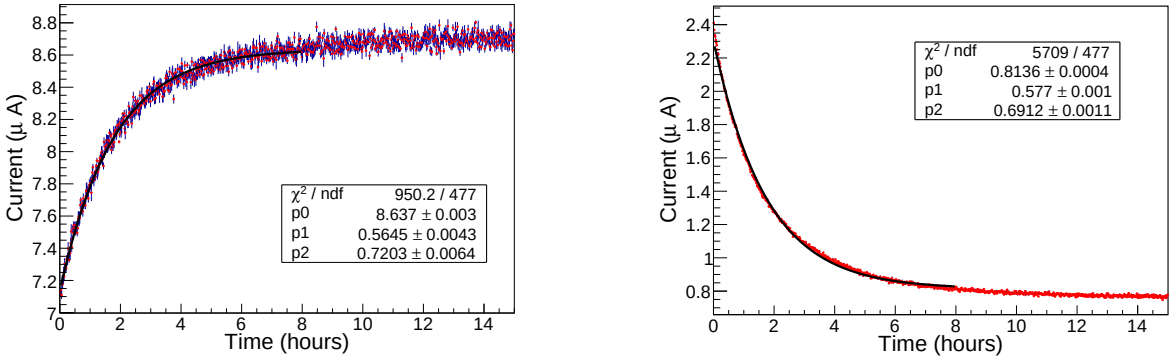

(a) Irradiation (b) Shielding

Figure 4.12: Examples of fitting.

The observed current and fitting parameters are summarized in Figure 4.13 and Table 4.2. The result shows that each crystal has unique τ and $\Delta I_{\max}$. As shown in Figure 4.14, no correlation was found between τ and $\Delta I_{\max}$. On the other hand, $\Delta I_{\max}$ showed a correlation with the measured current values after exposing to the room light.

As shown in Figure 4.12 and Figure 4.13, the same crystal (serial number 45) was measured with two sources with different intensities. In each measurement, the hit rate of the β-rays was also measured by using a discriminator and scaler. The threshold of the discriminator was adjusted as small as possible, but large enough not to trigger on the dark noise of the SiPM. As summarized in Table 4.3, $\Delta I_{\max}$ became larger with the higher hit rate.

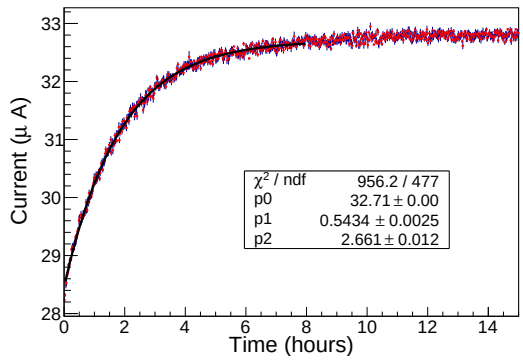

(a) Serial number 45

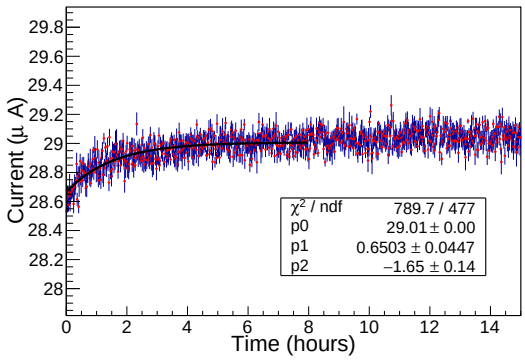

(b) Serial number 1

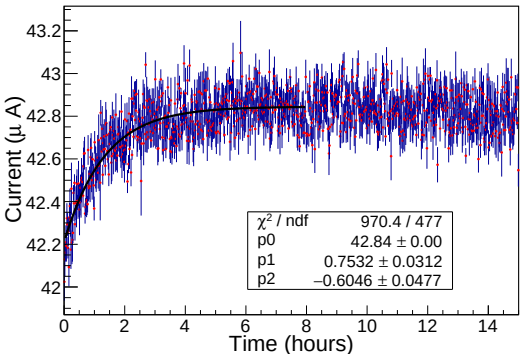

(c) Serial number 35

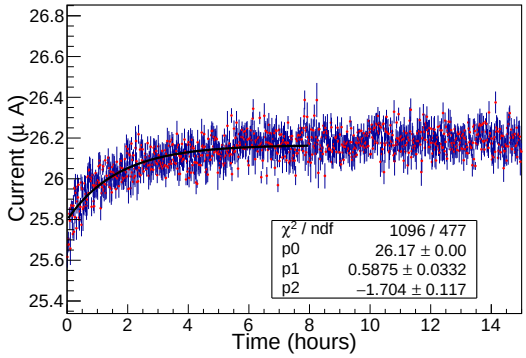

(d) Serial number 62

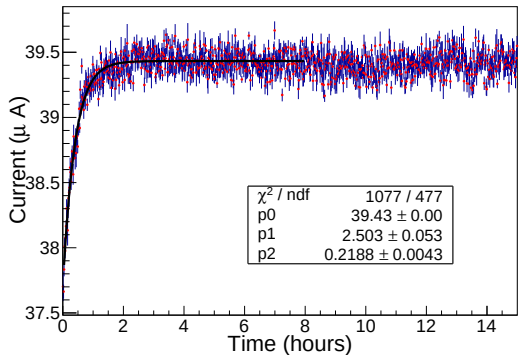

(e) Serial number 8

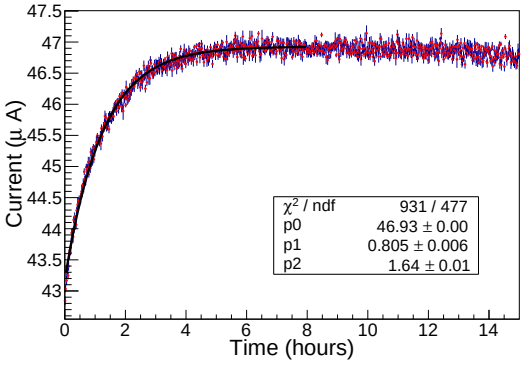

(f) Serial number 26

Figure 4.13: Sensor current of the SiPM during the irradiation with 37 MBq ^{90}Sr. The order of the figures is corresponding to the order of the measurement.

Serial number	$\Delta I_{\max}$ (μA)	τ (hours)
45	4.246 ± 0.028	1.840 ± 0.009
1	0.342 ± 0.002	1.538 ± 0.011
35	0.634 ± 0.004	1.328 ± 0.055
62	0.367 ± 0.002	1.702 ± 0.096
8	1.729 ± 0.012	0.400 ± 0.008
26	3.744 ± 0.025	1.242 ± 0.009

Table 4.2: Fitting parameters.

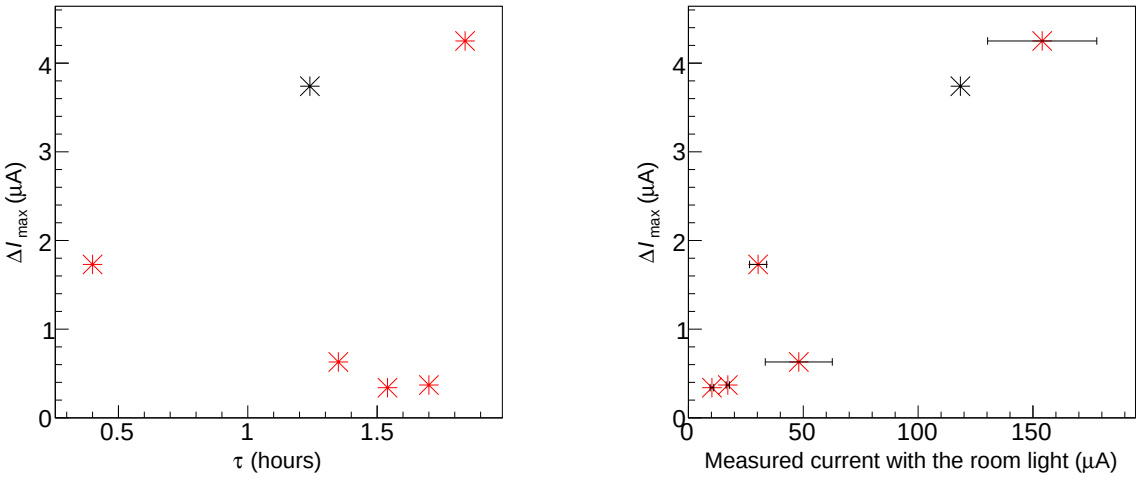

Figure 4.14: Left : $\Delta I_{\max}$ vs. τ. Right : $\Delta I_{\max}$ vs. measured sensor current after exposing to the room light. The black plot shows the additional measurement with serial number 28. The current with the room light was measured three times in the red plots. The error bar is the standard deviation of the three results.

Radioactivity of the ^{90}Sr (MBq)	Measured hit rate (kHz)	$\Delta I_{\max}$ (μA)	τ (hours)
3.7 (nominal)	161	1.502 ± 0.007	1.771 ± 0.013
37	372	4.246 ± 0.028	1.840 ± 0.009

Table 4.3: Comparison of the parameters for different source intensities.

4.2.3 Influence on the energy resolution

The influence on the energy resolution was estimated by calculating the number of photoelectrons contained in the waveform of the SiPM. Let us consider the case where the waveform contains photoelectrons induced by afterglow. The total number of photoelectrons in a single waveform can be expressed as :

$$N_{\text{all}} = N_{\text{sig}} + N_{\text{AG}}, \tag{4.2}$$

where $N_{\rm sig}$ and $N_{\rm AG}$ are the number of photoelectrons from the signal positron and the afterglow, respectively. Due to the photoelectrons from afterglow, the mean value of the photo-peak becomes larger. Here, the energy resolution is defined as the ratio of the variation of $N_{\rm all}$ ($\sigma_{\rm all}$) and the absolute energy of the signal. Hence, the energy resolution R can be written as :

$$R = \frac{\sigma_{\rm all}}{N_{\rm sig}}, \tag{4.3}$$

where $\sigma_{\rm all}$ is the variation of $N_{\rm all}$. By assuming that the number of photoelectrons follows a Poisson distribution, the energy resolution can be written as :

$$R = \frac{\sqrt{N_{\rm sig} + N_{\rm AG}}}{N_{\rm sig}}. \tag{4.4}$$

Therefore, the contribution of afterglow can be calculated with the energy $N_{\rm sig}$ and $N_{\rm AG}$. Let us consider the 6% energy resolution at 1 MeV, where $N_{\rm sig}$ can be approximately estimated as ∼280. On the other hand, $N_{\rm AG}$ can be calculated as :

$$N_{\rm AG} = \frac{\Delta I_{\rm max} \times W}{G \times e}, \tag{4.5}$$

where W is a width of the signal waveform and G is a gain of the SiPM. e is an elementary charge (1.6×10^{-19} C). The typical width of the waveform is ∼300 ns. The gain of the SiPM is approximately 6.0×10^5 according to the spec sheet [16]. Because $\Delta I_{\rm max}$ is calculated as the difference of the two current values, the effect of the dark current of the SiPM is not included. Figure 4.15 shows the expected energy resolution as a function of $\Delta I_{\rm max}$.

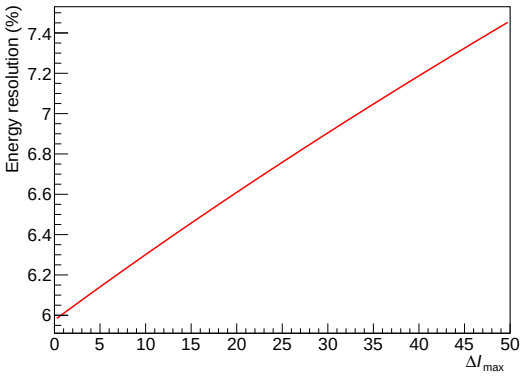

Figure 4.15: Expected energy resolution.

4.2.4 Discussion

As a conclusion of the study, we can conclude that the influence of afterglow is expected to be small. The reasons are as follows :

- The crystal (serial number 45) induced the largest sensor current of the SiPM in all the crystals after exposing to the room light. (Figure 4.6)
- The measured current in two results (with the room light and β-ray source) are correlated (figure 4.14).
- ΔI_{max} in the serial number 45 can be considered as less than 10 μA even if it is placed at the central area of the calorimeter where there is a high hit rate of $\sim$600kHz (Table 4.3).

Therefore, as shown in Figure 4.15, the influence on the energy resolution is expected to be less than 1% even if the crystal with a large afterglow is placed at the center of the calorimeter. Further reduction of the influence is possible by placing the crystal with a small afterglow at the center.

On the other hand, as shown in Figure 4.9, we observed that the current had kept increasing for 20 days. However, because of its very slow change, the total variation of the current is expected to be 50 μA at most even if we keep operating the calorimeter for 200 days. Therefore, we concluded that the influence on the energy resolution due to the slow component is expected to be also small (less than 1.5%).

4.3 Optimization of optical coupling

Because the crystal and the SiPM are not glued in the calorimeter, the optical coupling needs to be optimized. We compared three possibilities as shown in Figure 4.16 for the optical coupling. The pad made of soft elastic materials which has a thickness of 1 mm. It is commonly used for the optical coupling of a scintillator and a PMT. One the other hand, the film is much thinner (20 μm) since it is developed for the coupling between light fibers.

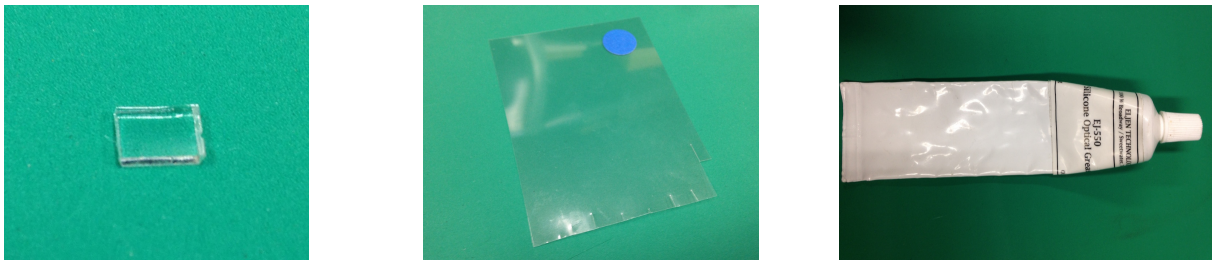

(a) Pad (Saint-Gobain, BC634A) (b) Film (Tomoegawa, FW205) (c) Grease (Eljen, EJ550)

Figure 4.16: Candidates for the optical coupling.

The best way of the optical coupling was investigated by comparing the light yields of the crystal. The same setup as shown in Figure 4.1 was used. In addition to those three configurations, the measurement without any optical coupling materials was also performed. Figure 4.17 shows the measured light yield at the 1.17 MeV peak of ^{60}Co with different over

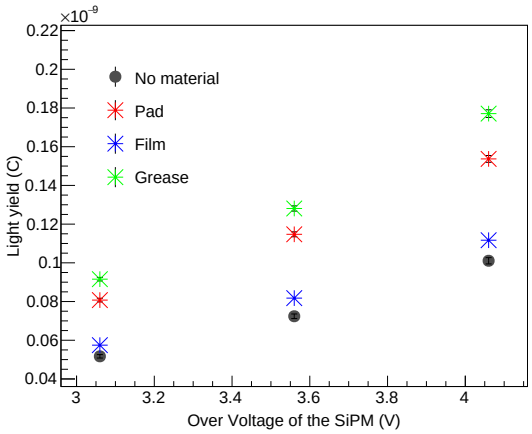

Figure 4.17: Light yield of the crystal and the over voltage of the SiPM.

voltages of the SiPM. The significant improvement of the light yield was observed by using the pad or grease.

As can be seen in the result, the grease is a little superior to the pad. In order to check the reproducibility, we repeated same measurement only with the grease and the pad (Figure 4.18). As a result, a larger light yield was always obtained by using the grease. Therefore, we concluded that using the grease would be the best way for the optical coupling.

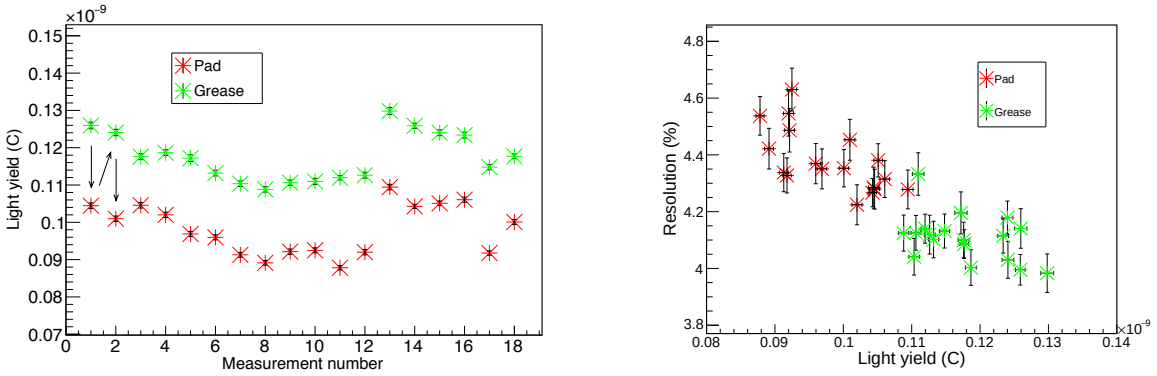

Figure 4.18: Comparison of the grease and the pad. Left : Comparison of the light yield. The arrows represent the order of the measurement. Right : The energy resolution and the light yield.

Chapter 5

Commissioning of the Downstream Detector

In July, 2016, the first commissioning of the downstream detector was carried out by using a high intensity muon beam at the $\pi E5$ beam line. This chapter describes the details of the commissioning from the setup to the data analysis. We successfully demonstrated the capability of the identification of the RMD events. At the same time, several issues were revealed. The details of the issues and the prospects are discussed in the last section.

5.1 Setup

The setup of the commissioning is shown in Figure 5.1. As the same condition as the MEG II experiment, the high intensity muon beam ($\sim 10^8\ \mu^+/s$) was transported to the stopping target. The downstream RDC detector was installed at end cap of the COBRA cryostat. The low momentum positrons were swept along the beam axis by a gradient magnetic field produced by the COBRA magnet. As a substitution for the liquid-xenon photon detector, a detector based on BGO crystals with PMT readout was used. The positron spectrometer was not used in this commissioning. The details of the apparatus and DAQ setup are described below.

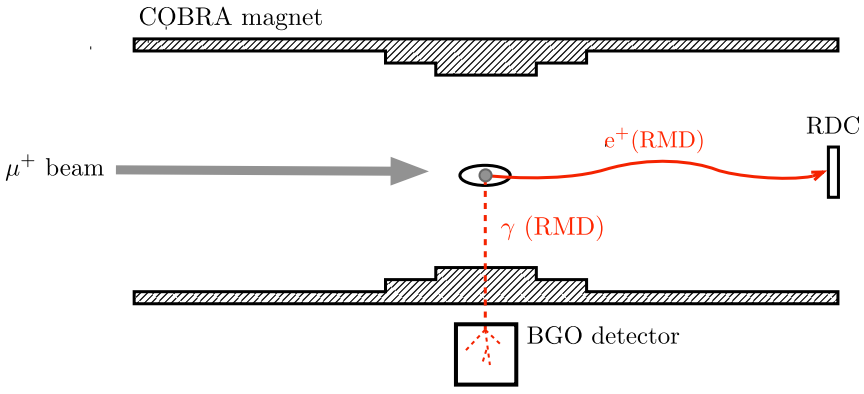

Figure 5.1: Schematic view of the setup.

5.1.1 RDC installation

During the MEG II data taking, the downstream RDC is required to be movable. This is because a calibration system for the photon detector is needed to be inserted on the beam axis from the downstream side. Therefore, the downstream detector is mounted on a moving arm. Figure 5.2 shows the stage with the moving arm, which was developed by the detector group in PSI. In order to be operational in the strong magnetic field, most of the components are made of aluminum. On the other hand, several parts in which there are heavy loads, such as the shaft of the arm, are made of titanium. The detector is moved by two plastic water pistons behind the stage. The position of the detector can be monitored with two end switches.

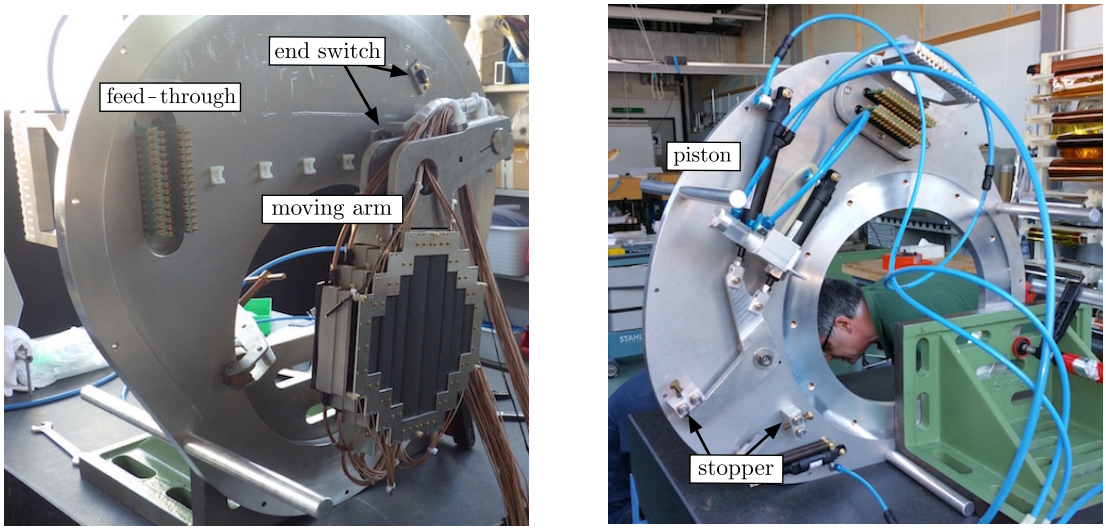

(a) front (b) back

Figure 5.2: Stage of the downstream RDC.

The mechanism of the moving arm was tested in the laboratory with the RDC detector mounted. As shown in Figure 5.3, the detector can take two positions. While the calibration system is inserted, the detector stays in the parking position. The moving system was successfully tested in the laboratory, however, during the commissioning, the detector was always set to the measuring position due to a geometrical conflicts between the front part of the detector and the end cap of the COBRA.

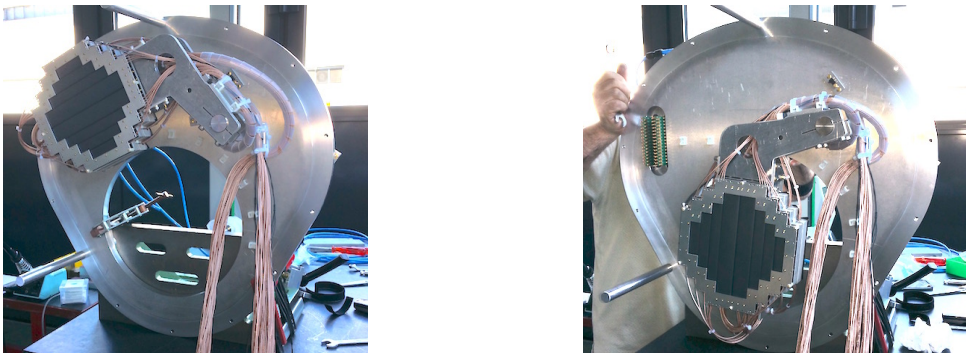

(a) parking position (b) measuring position

Figure 5.3: Positions of the detector.

Because the detector is installed in the helium atmosphere, all the cables are connected to outside electronics by using two feed-through PCBs. The feed-through PCB was originally developed for the MEG II photon detector. It is designed to have a high density signal transmission from vacuum and realize a low noise environment. The single PCB can contain 60 channels at most (Figure 5.4). The downstream detector has 100 signal channels (timing counter : 24 channels, calorimeter : 76 channels) in total. In addition, two thermometers (PT100 : 2 channels $\times$ 2) and two end switches (2 channels $\times$ 2) were connected to the same PCB. The one thermometer was equipped inside the calorimeter, near the SiPMs. The other one was placed outside the main frame of the LYSO crystals. The temperatures had been always monitored during the commissioning because the gain of the SiPMs are affected by the change of the temperature.

Figure 5.5 shows the detector after the cabling and the light shielding. All the cables were fixed on the stage, in order to avoid the interruption with the moving arm.

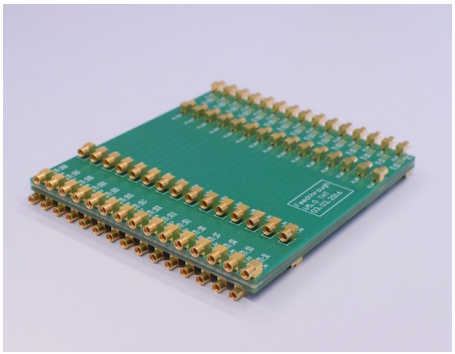

Figure 5.4: Feed-through PCB.

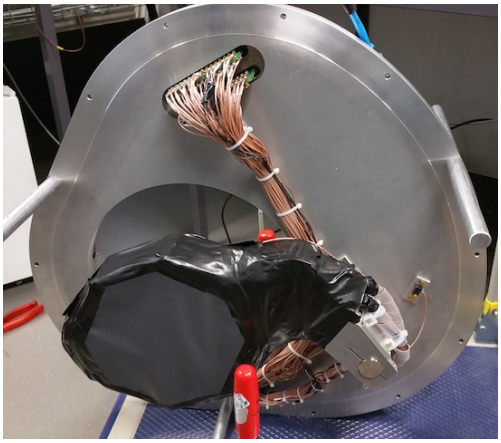

Figure 5.5: Detector after cabling and light shielding.

5.1.2 BGO photon detector

The photon detector consists of 16 BGO (Bismuth Germanium Oxide) crystals readout with PMTs (Figure 5.6). The BGO detector was originally developed as a tagging detector for the energy calibration of the liquid-xenon detector. It was designed to detect high energy photons (54.9, 82.9 MeV) from $\pi^0 \to \gamma\gamma$, which follows the charge exchange reaction ($\pi^- p \to \pi^0 n$). The BGO crystal is superior in terms of a short radiation length (1.12 cm) and a small Molière radius (2.23 cm). The crystals are readout with fine-mesh-type PMTs (H8409-70, from Hamamatsu Photonics), which are operational in the strong magnetic field. Therefore, we considered that the BGO detector would efficiently detect the high energy gamma-rays from RMD ($E_\gamma > 48$ MeV). For the original purpose of the BGO detector, it was placed at the opposite side of the liquid-xenon detector. The detector was aligned to face forward the center point of the target.

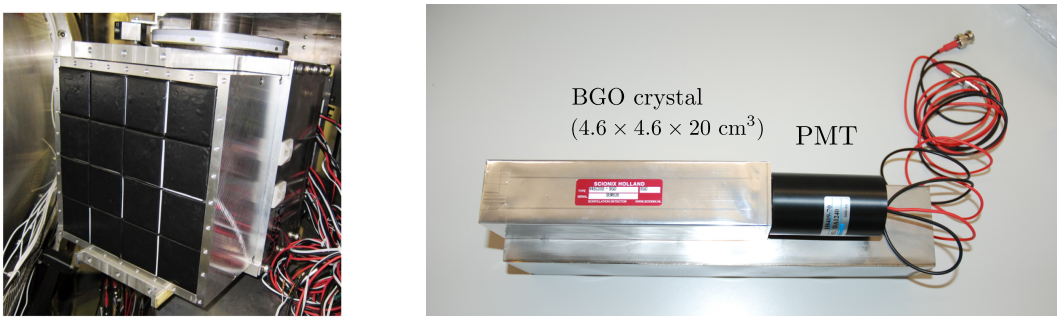

Figure 5.6: BGO detector. Left : 16 BGO crystals. A front cover of the crystals is not attached. Right : BGO crystal attached with the PMT.

5.1.3 DAQ

The signals from the RDC and BGO detector were transmitted to the WaveDREAM boards (Figure 5.7). The WaveDREAM board contains a power supply, waveform shaper, pre-amplifier and waveform digitizer. Because each board contains 16 channels, eight boards were prepared for the RDC and the BGO detector. The boards assignment for each detector and the configurations of the pre-amplifiers are summarized in Table 5.8. Each waveform was digitized with a sampling frequency of 2 GHz. Since each channel of the BGO detector requires a high bias voltage (∼2 kV), another power supply was prepared.

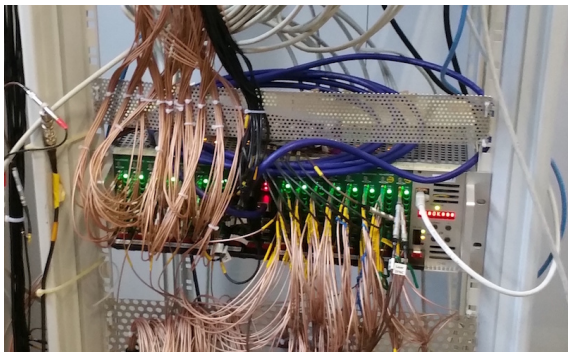

Figure 5.7: WavedDREAM boards after cabling. The left half part was used for the RDC and the BGO detector.

	N_{channel}	N_{board}	Gain
Timing counter	24	2	100
Calorimeter	76	5	1
BGO detector	16	1	1

Figure 5.8: Boards assignment for each detector and the gain of the pre-amplifiers.

5.1.4 Signal check

Before the data taking, we checked the signals of all the channels in each detector. For the RDC detector, the waveforms were checked with an oscilloscope by applying the bias voltages with a picoammeter (Keithley, 6485). The waveforms of the cosmic-rays and intrinsic radioactivities of the LYSO crystal were checked for the timing counter and the calorimeter, respectively.

No strange waveforms were observed in the calorimeter. On the other hand, we could not observe any waveforms in four channels in the timing counter (Figure 5.9). In these channels, the current of the SiPMs were nearly zero even if we applied the bias voltages. After the commissioning, the cause of the problematic channels was investigated. The detail is discussed in section 5.5.

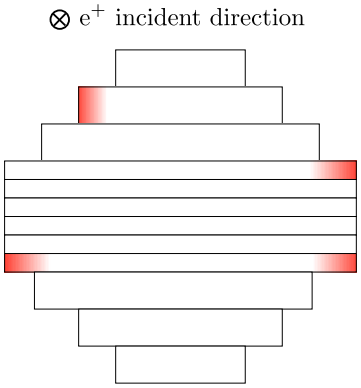

Figure 5.9: Problematic channels in the timing counter (red parts).

For the BGO detector, the signals of the cosmic-rays were checked. No problematic channels were found. In order to optimize the bias voltage of each PMT, the waveform data was acquired beforehand. The details of the calibration of the BGO detector are described in the next section.

5.2 Calibration

We firstly measured the timing offset of the RDC and the BGO detector in order to properly set the timing window for the RDC. The offset mainly comes from the difference of the cable lengths. Figure 5.10 shows the schematic view of the set up for the measurement. We prepared a trigger counter based on the plastic scintillator and SiPMs, whose cable length is same as the RDC detector. The trigger counter was put on the top of the BGO detector and same cosmic-ray events were acquired. The timing offset was measured to be 30.8 ns by calculating the constant fraction timing for each waveform.

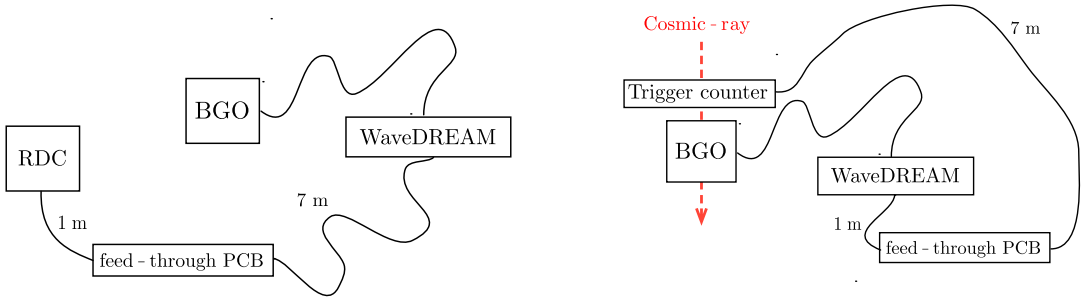

(a) Commissioning (b) Timing offset measurement

Figure 5.10: Schematic view of the setup.

5.2.1 Non-linearlity of the WaveDREAM

During the calibration, a non-linearity of the readout amplitude of the WaveDREAM was found. In order to know the correct energy scales with the calibration, the response functions

were measured. By using a function generator (Agilent, 81150A), we made an input pulse which is similar to the that of the LYSO crystals (Figure 5.11). We compared the input pulse height and the readout amplitude which was calculated as a difference of the peak amplitude and the baseline amplitude.

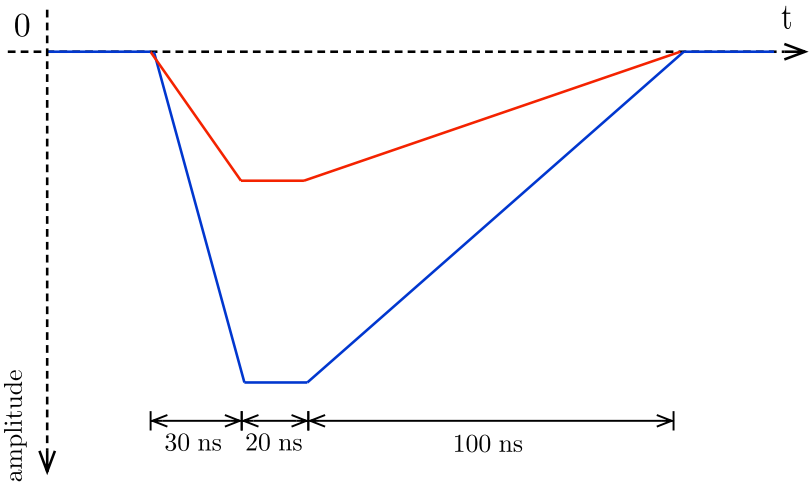

Figure 5.11: Schematic view of the input pulse. Several pulse heights were used.

Figure 5.12 shows the response functions which were measured by changing the input pulse height. All the channels in the calorimeter and the BGO detector were measured. Because the timing counter does not require the precise energy calibration, the common response function was used for all the timing counter channels. Before the waveform analysis, the amplitude data of each bin was corrected with these response functions. The example of the corrected waveform is shown in Figure 5.13. In the final design of the WaveDREAM board, the non-linearity will be fixed.

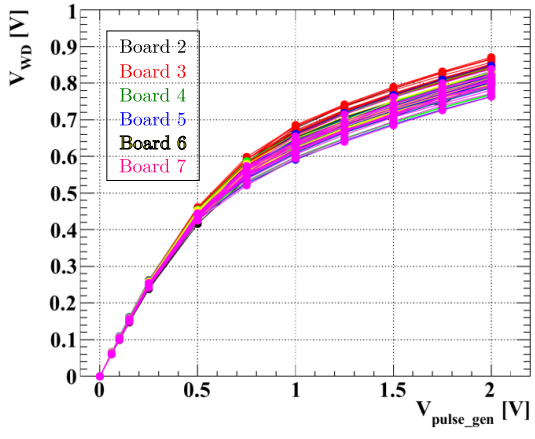

Figure 5.12: Input pulse height and the the measured pulse height of the output waveform.

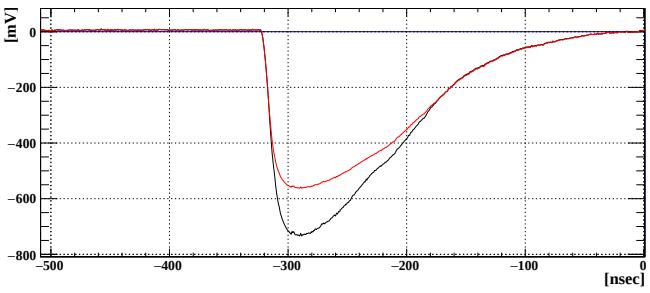

Figure 5.13: Example of waveform correction (calorimeter channel). Red and black shows the waveform before and after correction, respectively.

5.2.2 Energy scale calibration

In order to equalize the gain and to obtain the absolute energy scale of each channel, each detector was calibrated with the different calibration sources.

A. RDC

The timing counter was calibrated by using the positrons from Michel decay. During the commissioning, the calibration data was acquired by triggering on any hit of the timing counter. Figure 5.14 shows the simulated actual energy deposit and the measured spectrum fitted with a Landau's function. According to the simulation study with GEANT4, the mean energy deposit of the Minimum Ionizing Particle (MIP) is about 0.8 MeV.

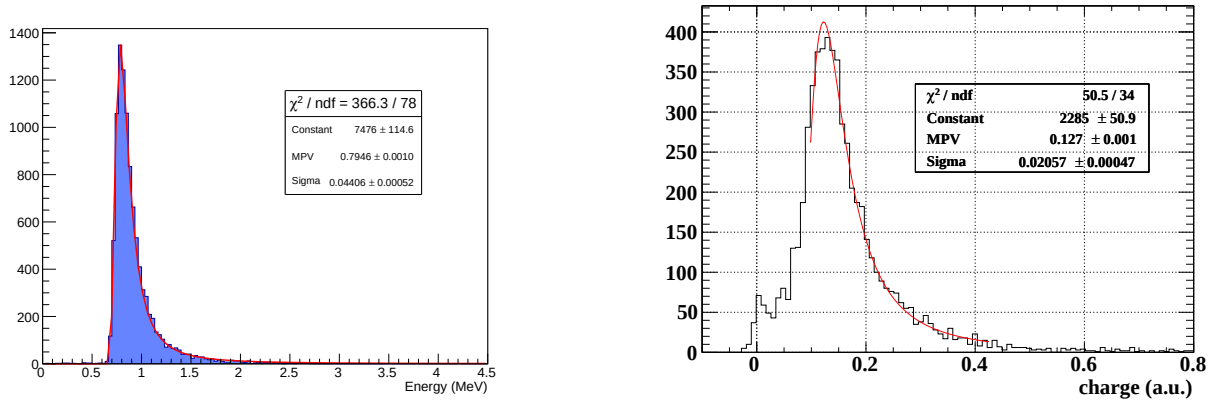

Figure 5.14: Simulated energy deposit (left) and measured spectrum (right).

As previously mentioned, the calorimeter is calibrated by using a peak of the intrinsic radio activity of the LYSO crystals. During the commissioning, the calibration data was acquired by triggering on any hit of the crystal with the beam turned off. As shown in figure 5.15, the spectrum has both photo-peaks of the gamma-ray and β-decay spectra. We fitted the photo-peak corresponding to ~ 600 keV. The fitting function consists of a photo-peaks and a β-decay spectra, which are smeared with the energy resolution.

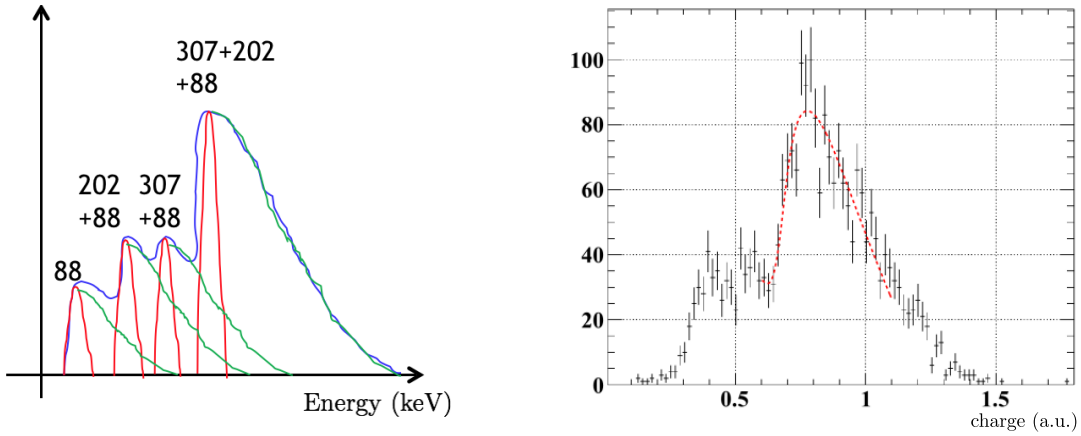

Figure 5.15: Left : Expected energy spectrum (blue). The red and the green parts show the photo-peaks of the gamma-rays and the β-decay spectrum, respectively. The Q-value of the β-decay spectrum is 1192 keV [20]. Right : Example of the measured spectrum in the single channel.

B. BGO detector

The BGO detector was calibrated with two calibration sources. In order to equalize the gain of each channel, the cosmic-ray data was acquired before the physics data taking. The muon beam was turned off during the calibration. The data was acquired by triggering on the coincidence hit of any top and bottom crystals. The second calibration source was gamma-rays of the ^{88}Y source (0.9, 1.8 MeV). This calibration was performed for the one channel in order to know the absolute energy scale (figure 5.16).

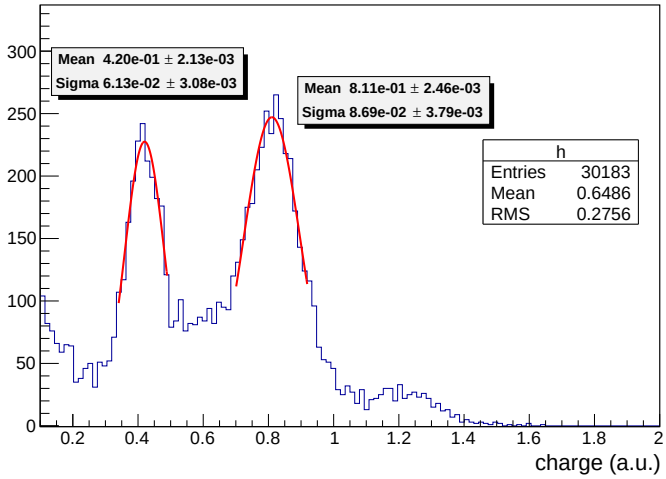

Figure 5.16: Measured spectrum with the ^{88}Y.

According to the simulation study, the energy deposit of the cosmic-ray is expected to be around 45.4 MeV. However, if we assume that the energy scale calibration with the ^{88}Y is correct, the measured energy deposit of the cosmic-rays is about 17% lower (figure 5.17). The detail of the discrepancy between the two calibration results is discussed in the last section.

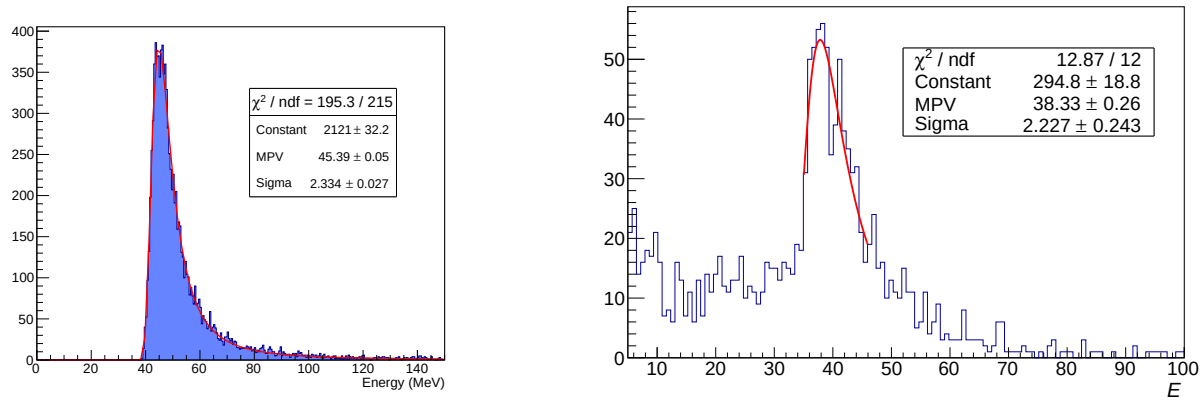

Figure 5.17: Simulated energy deposit (left) and measured spectrum (right). The energy scale of the measured spectrum is calibrated with the gamma-rays of ^{88}Y.

5.3 Data taking

The physics data had been acquired by triggering on any hit of the BGO crystals. The trigger rate was about 15 Hz. The threshold of each crystal was around 35 MeV if we assume that the calibration with the ^{88}Y is correct. About 680000 events were acquired in total. The data acquisition rate was about 5 Hz due to the limited transmission speed of the trigger board. Most of the triggered events have the energy deposit greater than 52.8 MeV, which are triggered by the cosmic-rays (figure 5.18).

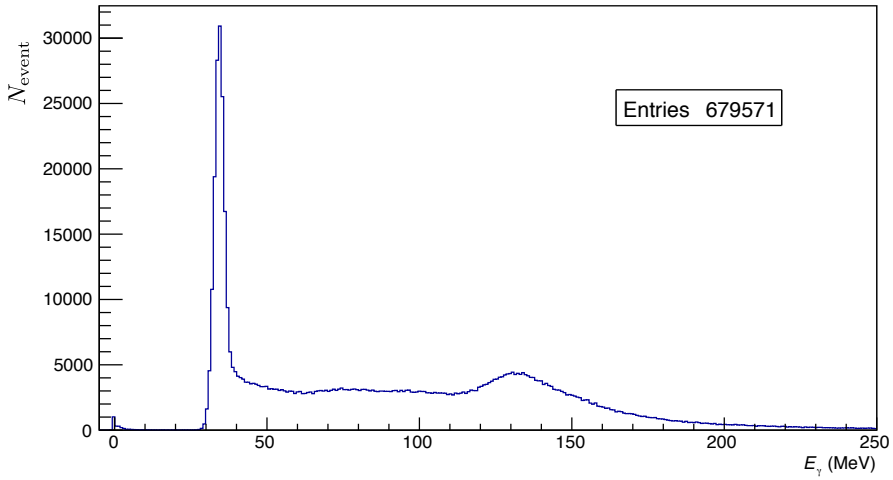

Figure 5.18: Total energy deposit in the BGO detector of all the triggered events. The energy scale is defined by the calibration data with the ^{88}Y.

5.4 Analysis

Each waveform data was analyzed by using a software developed for MEG II. The pulse height was calculated as the difference of the peak amplitude and the baseline which was calculated by averaging amplitudes in the region before the pulse. The timing of the pulse was calculated with the constant fraction method. The timing where the waveform reached

15% of the full pulse height was measured. The light yield was calculated by integrating the waveforms.

5.4.1 Event selection

Because most of the events were triggered by the cosmic-rays, we first applied the event selections in following two steps. First, the event was selected with the hit positions in the BGO detector. As shown in figure 5.19, the cosmic-ray track makes several hits from the top to the bottom crystals. Moreover, if the gamma-ray from RMD hits the crystal in the edge, the energy deposit could not be measured correctly. Therefore, we defined the fiducial volume of the BGO detector as the central four crystals (figure 5.20) and selected the event which had the largest energy deposit in this area.

Second, the events were selected with the total energy deposit in the BGO detector. As previously mentioned, the event whose energy deposit is greater than 52.8 MeV are considered to be triggered by the cosmic-rays. Figure 5.21 compares two spectra of the energy deposit of the BGO detector, which were acquired either with or without the muon beam. We set the energy threshold to 55 MeV to cut the cosmic-ray events.

Figure 5.22 shows the energy deposit distribution of the BGO detector after applying two cuts. Most of the cosmic-ray events were rejected (98%).

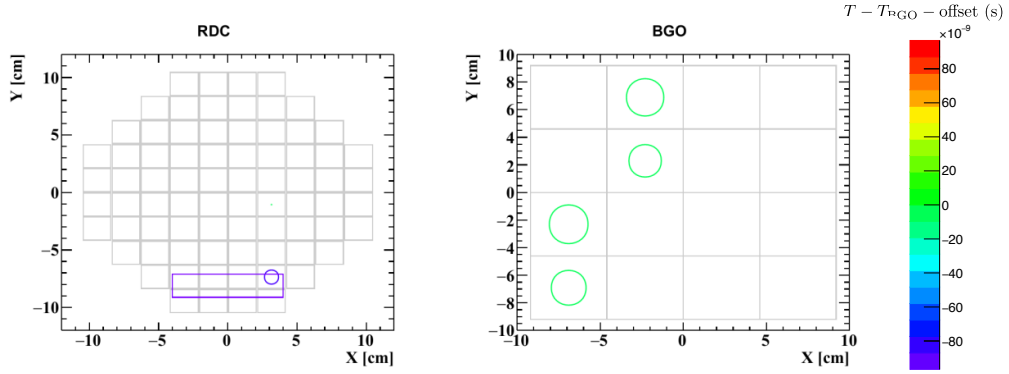

(a) Candidate of the cosmic-ray event

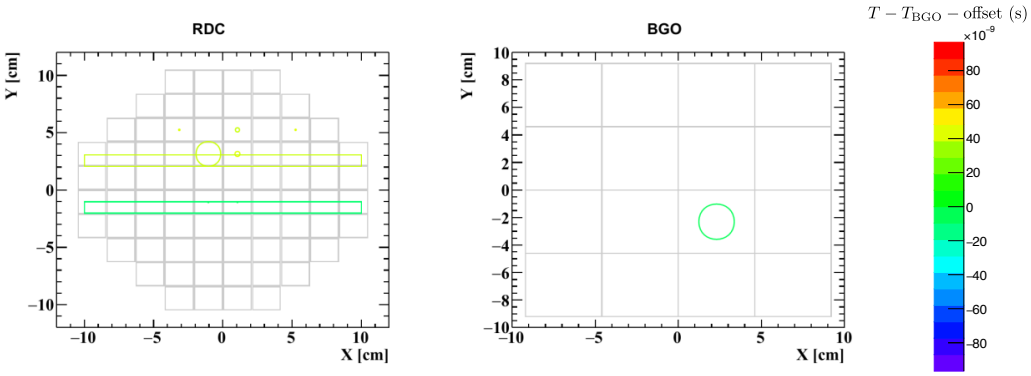

(b) Candidate of the RMD event

Figure 5.19: Event display of the RDC and the BGO detector. The marker color and the diameter represent the hit timing and the energy deposit respectively.

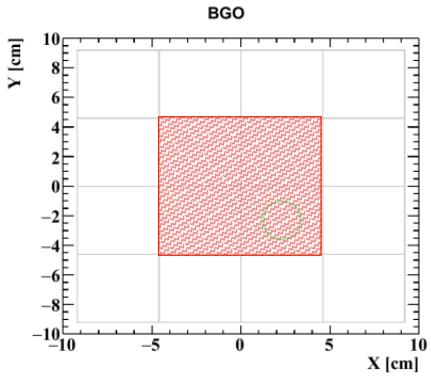

Figure 5.20: Fiducial volume of the BGO detector (red shaded part).

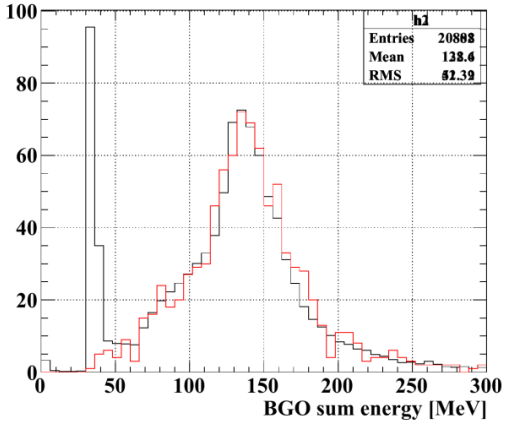

Figure 5.21: Total energy deposit in the BGO detector. The black and red spectra shows the beam on and off data, respectively.

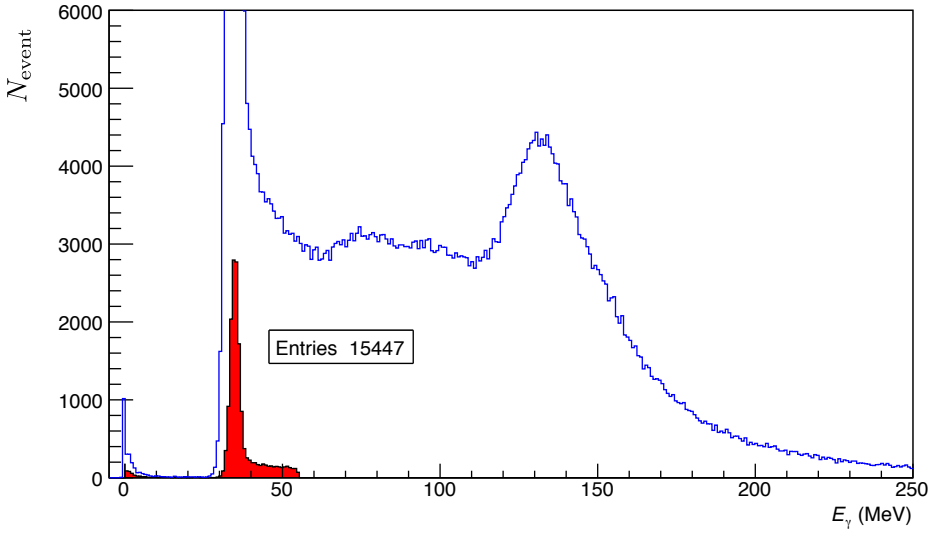

Figure 5.22: Total energy deposit in the BGO detector. The blue and red part shows before and after the event selections, respectively.

5.4.2 Timing coincidence of the RDC and BGO detector

After the event selection, the coincidence between the BGO detector and the RDC was checked. Figure 5.23 shows the timing differences of the two detectors. As a result, we successfully observed a clear timing peak, which is corresponding to the RMD events. At the same time, the accidental hits of the positrons from Michel decay were observed, which corresponded to the flat region of the Figure 5.23.

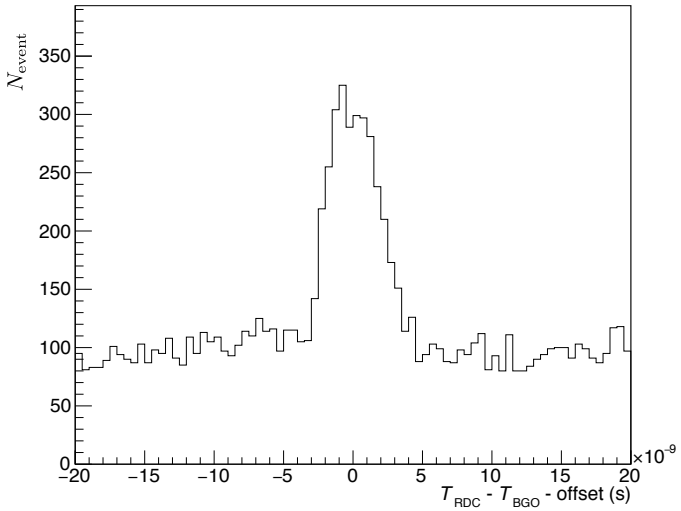

Figure 5.23: Timing difference of the BGO detector and the RDC.

5.4.3 Energy cut with the calorimeter

As previously mentioned, the accidental positrons from Michel decay are distinguishable because of their larger energy deposit than that of the positrons from RMD. Figure 5.24 shows the total energy deposit in the calorimeter after the event selection.

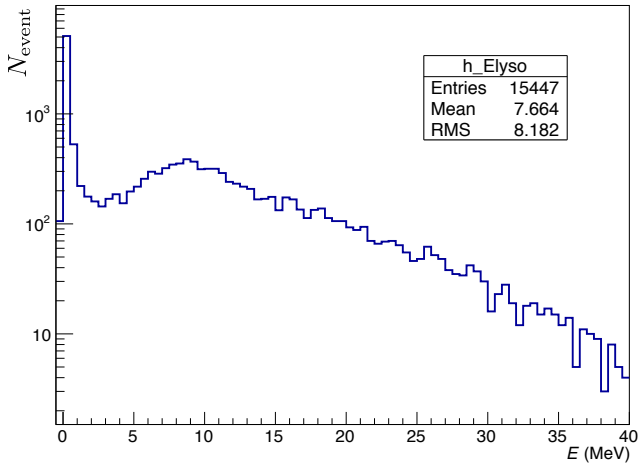

Figure 5.24: Total energy deposit in the calorimeter.

As a demonstration, we cut the events which have the energy deposits greater than 4 MeV. Figure 5.25 compares the timing difference of the BGO detector and the RDC before and after

the energy cut. As a result, the fraction of the flat regions were decreased to $\sim 1/10$. At the same time, the fraction of the timing peak of the RMD events was also decreased to $\sim 1/3$. This was probably due to the low energy threshold of the BGO detector ($E_\gamma >\sim 35$ MeV). The relatively high energy positrons from RMD were also cut.

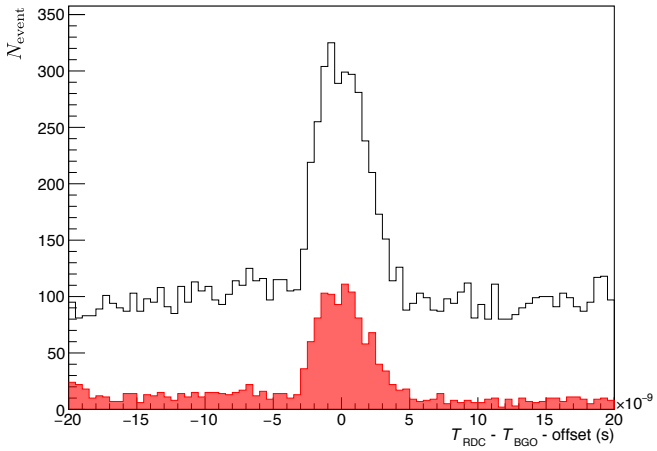

Figure 5.25: Timing difference of the BGO detector and the RDC after the energy cut with the calorimeter(> 4 MeV). The black and the red show the events before and after the cut, respectively.

5.5 Issues and prospects

As shown in the previous section, the first commissioning of the downstream RDC was completed. At the same time, it revealed following issues.

- A geometrical conflict between the front part of the RDC and the COBRA end cap was found.
- We found four problematic timing counter channels in the signal check. Because these channels did not work at all, $\sim 10\%$ of the timing counter acceptance was lost.
- We calibrated the energy scale of the BGO detector with two calibration sources (gamma-rays of the ^{88}Y and cosmic-rays), however, the MIP peak of the cosmic-rays are 17% smaller than expectation. Due to the discrepancy of the two results, the correct energy scales of the photons are uncertain accordingly.

The first issue can be solved by modifying some detector layouts because it requires only few millimeters of extra z space in front of the RDC. Other two issues were investigated after the commissioning. The details and prospects are described in the following sections.

5.5.1 Problematic channels in the timing counter

After the commissioning, we investigated the problematic channels in the timing counter by disassembling several counters. Because of the following reasons, the cause was considered as bad connections around the PCB.

- The three of the four problematic channels were placed near the MMCX connector in the long PCB, which had larger loads when connection or disconnection of the cables.
- When we push the PCB to the scintillator with applying the bias voltage, we again observed the signals.

The scheme of the assembly of the scintillator, SiPMs and PCB are illustrated in Figure 5.26. The cause was found to be a mechanical detachment between the PCB and the SiPMs where the conductive epoxy was used. The mechanical detachment was observed in some of the problematic channels after we removed the light shielding. Figure 5.27 shows the surfaces of the PCB and the SiPMs after we disassembled one of the counter by hand. The conductive epoxy sticks on the both PCB and SiPMs surfaces and it can be seen that the connection is not strong enough.

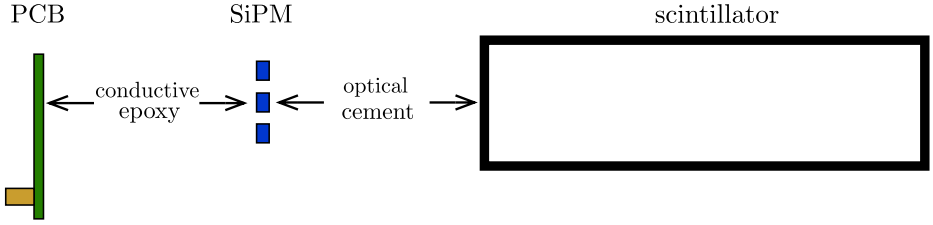

Figure 5.26: Schematic view of the connections in the timing counter.

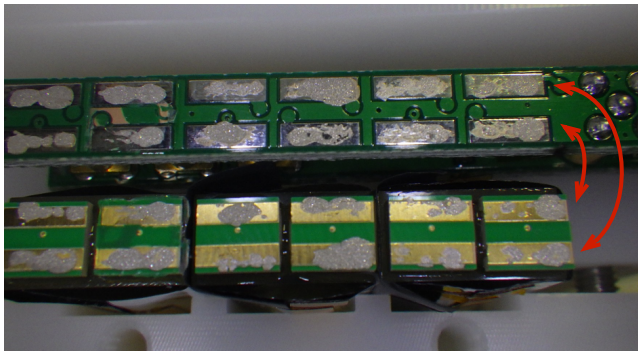

Figure 5.27: PCB (top) and SiPMs (bottom) after disassembling. The red arrows show the glued areas before disassembling.

As a solution to this problem, we are going to solder the SiPMs on the PCB instead of using the conductive epoxy. For the surface mount SiPMs, this process should be done by the reflow soldering. This was tested with a help of the electronics group in PSI. One PCB and three SiPMs were soldered in following steps.

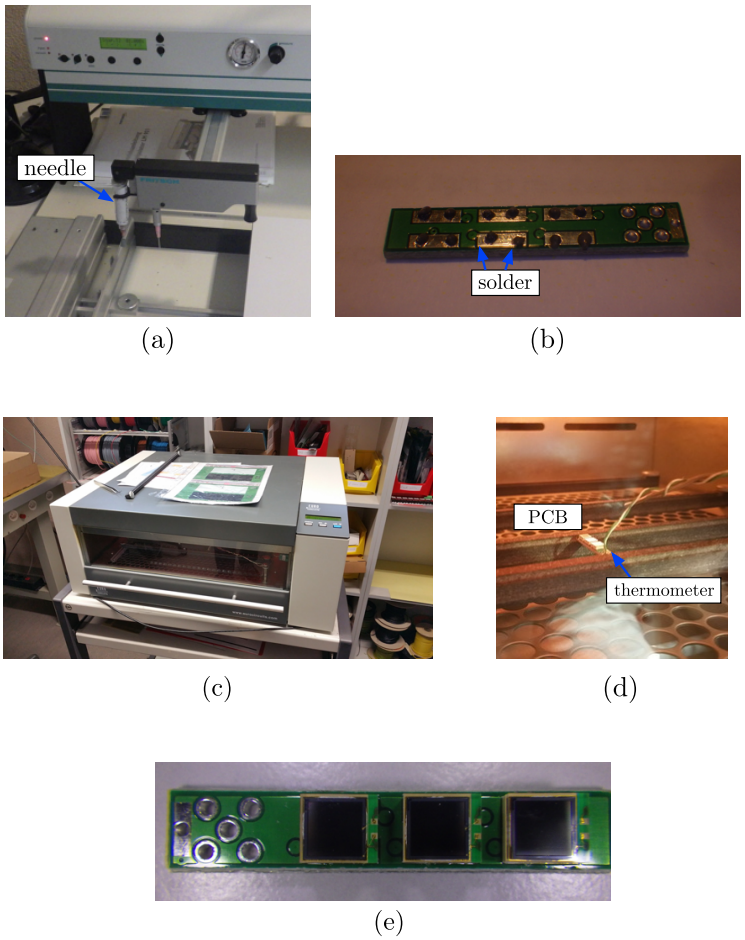

(a) (b) (c) (d) (e)

Figure 5.28: Reflow soldering processes.

1. A solder paste which has a diameter of ∼1 mm was put on the PCB by using a fine needle (Figure 5.28 (a), (b)).

2. The three SiPMs were aligned on the PCB by using a microscope.

3. The PCB and the SiPMs were heated with a reflow oven, which can gradually change the temperatures (Figure 5.28 (c)). The temperature was changed in accordance with the handling manual of the SiPMs

   peak temperature was set below the limitation of the SiPM (Peak temperature ∼ 240°C) [16]. It took about 10 minutes for the heating and the cooling. During this process, the temperatures were monitored with several thermometers (the one is attached to the PCB, Figure 5.28 (d)).

As long as we checked by eyes, neither a deformation nor a change of the color of the SiPMs due to heating were observed (Figure 5.28 (e)). Moreover, the alignment of the SiPMs were kept even after the reflow.

Next, we checked if there were no changes in the performance by heating the SiPMs. We made a test counter where the soldered PCB was glued in one side (Figure 5.29). By using the same setup as shown in Figure 3.10, we acquired the waveform data with the ^{90}Sr. Since we applied the same bias voltage on each channel, the gains of two channels were not exactly equal. However, as long as we compared the waveforms (Figure 5.30) and the light yields (Figure 5.31), no significant difference was observed in the soldered PCB. Moreover, we obtained ∼ 85 ps of the timing resolution which is good enough. Therefore, the reflow soldering can be solution for the detachment problem. We are going to reproduce all the timing counters in this way. Moreover, we will prepare some spare counters so that we can quickly replace with them even if problematic channels are found during the operation.

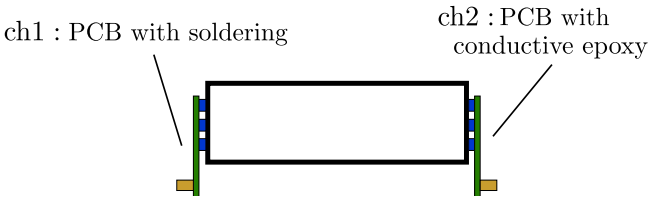

Figure 5.29: Schematic view of the tested counter. The length of the scintillator is 11 cm.

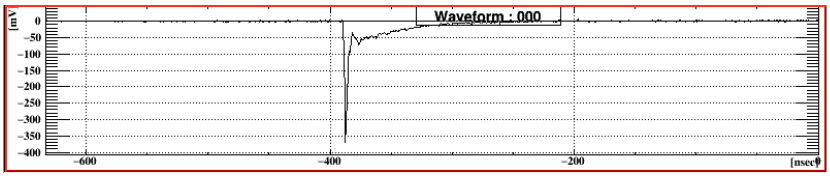

(a) ch1

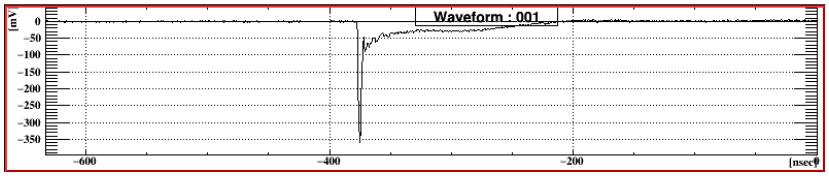

(b) ch2

Figure 5.30: Example of waveforms.

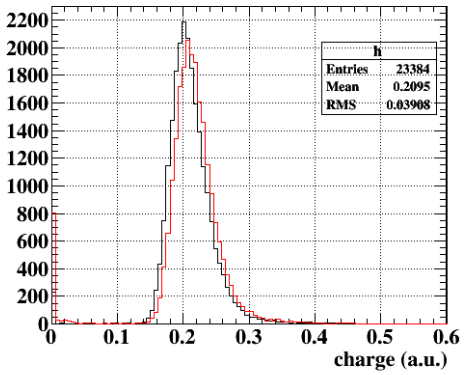

Figure 5.31: Comparison of the light yields. The red and black show the channel 1 and 2, respectively.

5.5.2 Uncertainty of energy scale of the BGO detector

For the quantitative evaluation of the capability of the background identification, the correct energy scale of the BGO detector has to be known. It is necessary to investigate the discrepancy between the two calibration results (gamma-ray of the ^{88}Y and cosmic-ray). For the possible reasons of this discrepancy, we considered following four possibilities.

I. Currently, the energy deposit of the cosmic-rays is calculated only for the case that the cosmic-rays are always penetrating perpendicularly at the center. On the other hand, the calibration data was acquired by triggering on the coincidence hit of any top and bottom crystals. Therefore, the actual energy deposit might have a smaller peak than 45.4 MeV by glancing the crystal.

II. We corrected the non-linearity of the readout amplitude of the WaveDREAM. However, the correction may not be perfect.

III. Because we placed the ^{88}Y in front of the crystal, the light yields of the gamma-rays could become larger if the response of the detector changes with different position and incident angle.

VI. There could be some non-linearity in the scintillation properties of the BGO crystal or the PMT.

In order to check the first two possibilities (I, II), we took the calibration data again after the commissioning by using a DRS evaluation board. As shown in figure 5.32, we used four crystals placed in a row. In the commissioning, two calibrations were performed with a channel A (Figure 5.16, 5.17).

This time, the ^{88}Y data was acquired in each of four channels. The source was set in front of the crystal as we did in the commissioning. While retaking the cosmic-ray data, two small trigger counters (1.5 cm cube) based on plastic scintillators and SiPMs were placed above the crystals to select the cosmic-rays with vertical incident angles. Moreover, for the analysis, we required coincidence hits in the bottom crystal (channel D).

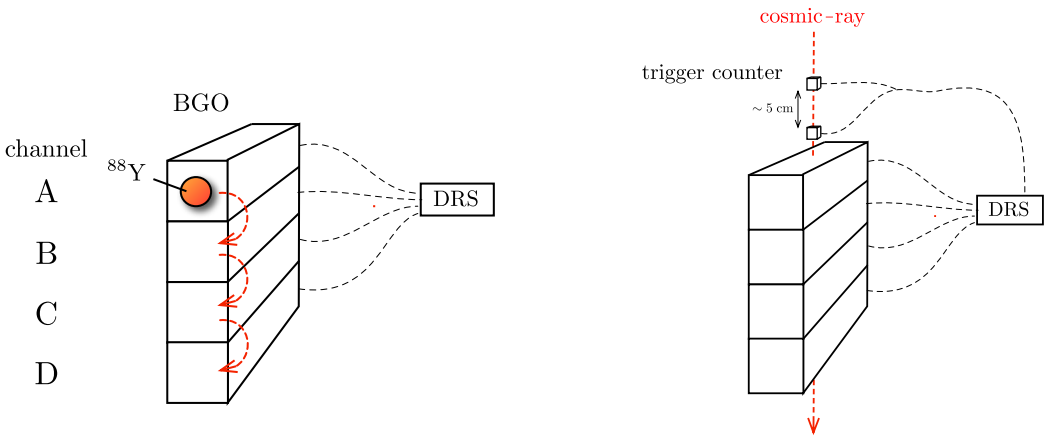

(a) Gamma-rays of the ^{88}Y (b) Cosmic-rays

Figure 5.32: Schematic views of the setup.

Figure 5.33 shows the example of the measured spectra. By using two photo-peaks of the gamma-rays (0.9, 1.8 MeV) in the ^{88}Y data, we calculated the MIP peak of the cosmic-rays. Table 5.1 summarizes the results of the calculations and the measured values by fitting. As a result, all the peaks of the cosmic-rays were measured to be smaller than their expectations. We concluded that the first two possibilities in the list were not the case.

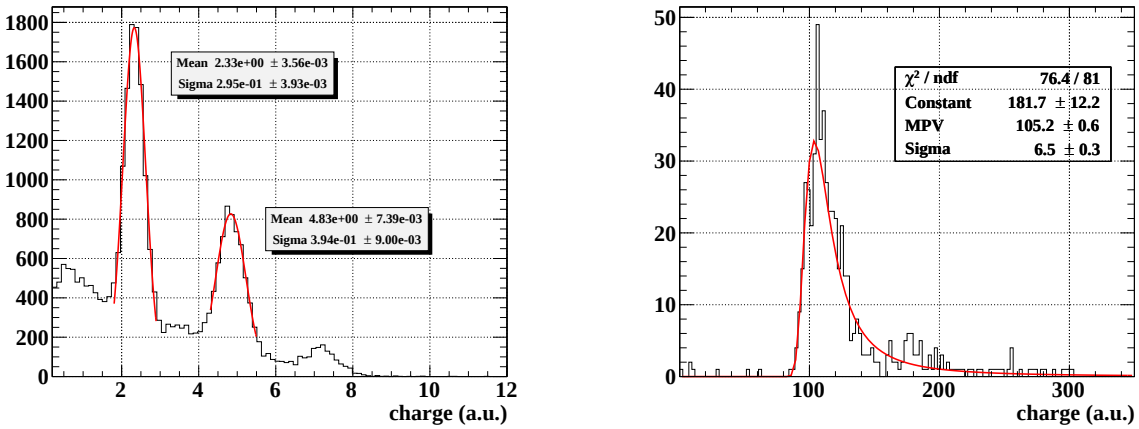

(a) Gamma-rays of the ^{88}Y (b) Cosmic-rays

Figure 5.33: Measured spectra (channel A).

Channel	Expected from ^{88}Y data	Measured value	Discrepancy (%)
A	126.1 ± 0.4	105.2 ± 0.6	16.6 ± 0.6
B	157.4 ± 0.4	122.5 ± 0.7	22.2 ± 0.5
C	155.9 ± 0.4	132.9 ± 0.8	14.8 ± 0.6
D	155.9 ± 0.4	122.4 ± 0.7	21.5 ± 0.5

Table 5.1: Light yields of the MiP peak of the cosmic-rays (45.4 MeV).

Next, we checked the position dependence of the gamma-rays by changing the positions of the source. As shown in Figure 5.34, we acquired the data by placing the source on the top of the channel A. The measured spectrum is shown in Figure 5.35. We compared the two photo-peaks to the peaks observed in Figure 5.33 (a). Table 5.2 shows the energy scales calculated by the photo-peaks in two configurations. Consequently, a large difference which may explain the discrepancies were not observed.

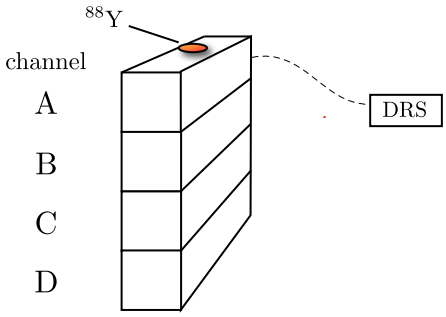

Figure 5.34: Schematic view of the setup

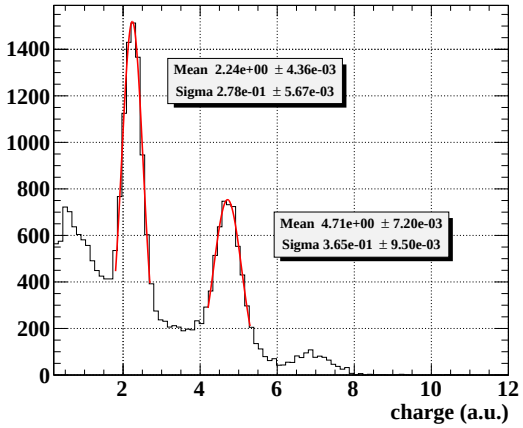

Figure 5.35: Measured spectrum.

^{88}Y position	Charge at 1 MeV (a.u.)
Front	2.78 ± 0.01
Top	2.74 ± 0.01

Table 5.2: Peak of the charge distributions in two configurations.

So far, we investigated all the possibilities on the list except VI. As long as we refer other experiments which uses the BGO detector, such a non-linearity is not reported. Although the fine-mesh-type PMT is known to have a good linearity, some non-linearity of the light yield and the readout amplitude are reported [21]. Because this could be a reason in our case, we will check it next.

Chapter 6

Development of the Upstream Detector

As previously mentioned, the influence of the upstream detector on the muon beam transportation has to be minimized. First of all, the influence on the beam spot was investigated by using a mockup RDC. According to the measured beam spot size with the mockup, the effect of the different beam size was evaluated in the simulation study. Moreover, the effect on the muon stopping rate was studied in the simulation. Section 6.2 describes the effect of the pileup beam muon. Because of the high hit rate of the beam muons (∼100 MHz), the detection efficiency loss due to pileup is not negligible. The configuration of the bundle widths can be also optimized to minimize the inefficiency due to pileup. Finally, according to the measured light yield or the inefficiency due to pileup, the total detection efficiency for RMD positrons was evaluated. Section 6.3 compares the efficiencies in several configurations.

6.1 Influence on the muon beam

6.1.1 Beam spot size on the target

The influence on the muon beam was studied with a help of the beam group of PSI. A mockup RDC with the same material thickness as expected for the scintillating fiber layer of the upstream RDC was used (Figure 6.1). The beam spot size at the target position was measured with two configurations as shown in Figure 6.2. When the upstream RDC is not installed, a degrader with a 300 μm Mylar foil is inserted at a beam waist inside the BTS to reduce the muon momentum. By thinning the degrader, the RDC with the same amount of the material thickness can be installed.

Figure 6.1: RDC mockup (230 μm thick Mylar foil).

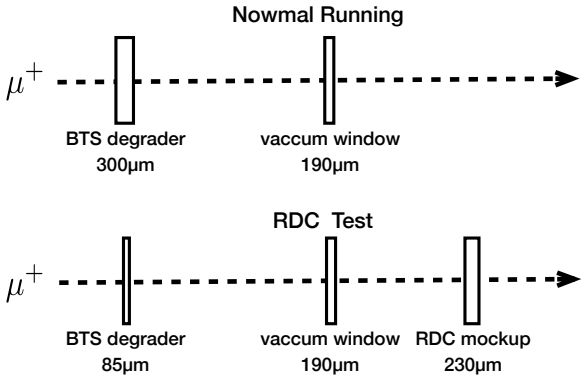

Figure 6.2: Schematic view of the setup.

The beam profile was measured in two dimensions at the target position by moving the position of a thick depletion-layer APD with a step size of 5 mm. Table 6.1 summarizes a result of gaussian fitting for each x and y distribution. The product of σ_x and σ_y increased by 16% with the mockup. Concerning the muon stopping rate, the comparison in a simulation study is described in section 6.1.3.

	σ_x (mm)	σ_y (mm)
without mockup	10.7 ± 0.2	10.4 ± 0.2
with mockup	11.5 ± 0.2	11.2 ± 0.2

Table 6.1: Beam spot size at the target position

6.1.2 Effect of the larger beam spot

As previously mentioned, a positron emitted from the target follows a spiral trajectory in the gradient magnetic field. The gradient magnetic field ranges from 1.27 T at the center to 0.49 T at the cryostat end ($|z| = 1.42$ m). If the beam spot becomes larger, the muon vertex will be spread more in z-direction due to the slanted angle of the target. As a consequence, the trajectory of the positron could be significantly affected with the larger beam spot. To study the influence on the positron tracking performance, a series of simulation studies were performed by using GEANT4. In order to simplify the study, the muon beam was not simulated, but the simulation started from a muon decay on the target. Table 6.2 summarizes the geometrical parameters concerning a size of the target in two configurations. In addition to the nominal size of the target, the bigger target was simulated. The bigger target is able to cover both ($6\sigma_x$, $6\sigma_y$) of the larger beam spot when it is placed with the slanted angle of 15°. The muon vertex distribution was input to the simulation according to the result of the mockup test (Figure 6.3).

	major-axis (mm)	minor-axis (mm)	thickness (μm)
nominal	260	70	120
larger	267	70	120

Table 6.2: Fiducial volume parameters of the target

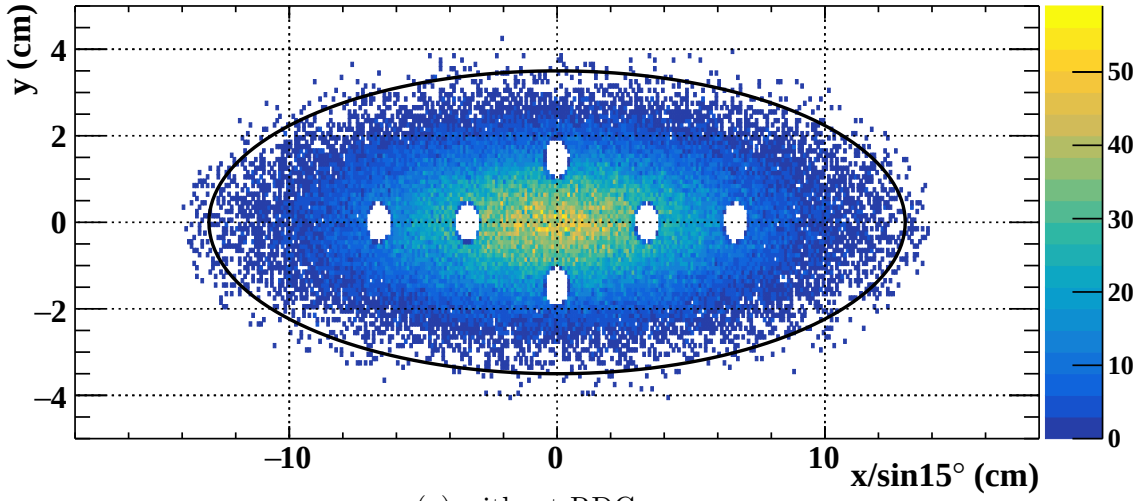

(a) without RDC

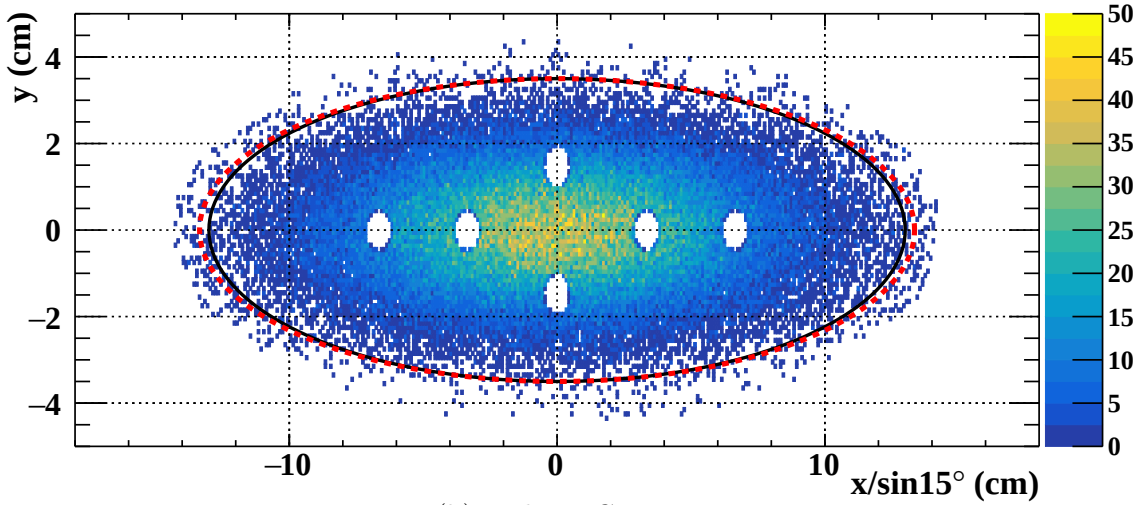

(b) with RDC

Figure 6.3: Distribution of the muon vertex on the target. Black solid line and red dashed line represent the fiducial area of the nominal and bigger target, respectively.

A. Detection efficiency for signal positrons

We firstly studied on the detection efficiencies of the drift chamber and the timing counter for the signal positrons.. In this study, $\mu^+ \to e^+\gamma$ events were simulated on the target. The emission angle of the photon was selected according to an acceptance of the MEG II liquid-xenon detector ($r = 64.97$ cm, $|z| < 23.9$ cm, $|\phi| < 1.05$ rad).

In the drift chamber, the signal positron track intersects multiple wire cells by making several turns. Once it crosses the outer shell of the drift chamber, the track will be interrupted. Figure 6.4 shows the distribution of the number of hit wire cells before crossing the outer shell in the drift chamber. The track with less than ∼50 hits are interrupted by the outer shell in the first turn. In the track reconstruction, a long track is important in order to obtain the good angular and momentum resolutions. Table 6.3, *I* shows the efficiencies of the drift chamber. For three different configurations, we first counted the number of events generated on the fiducial area of the target. The efficiency was then calculated as the probability not to be interrupted in the first turn. Figure 6.5 shows the distribution of the number of the hit tiles in the timing counter. The distribution does not seem different with the bigger beam spot. The efficiency of the timing counter was calculated as the probability to cross at least one counter tile (Table 6.3, *II*).

As summarized in Table 6.3, the product of two results represents the total efficiency. It was changed by −0.79% (standard target) and −0.83% (bigger target) with the bigger beam spot. As a result, it can be seen that the change of the efficiency for the signal positrons would be small with the upstream RDC.

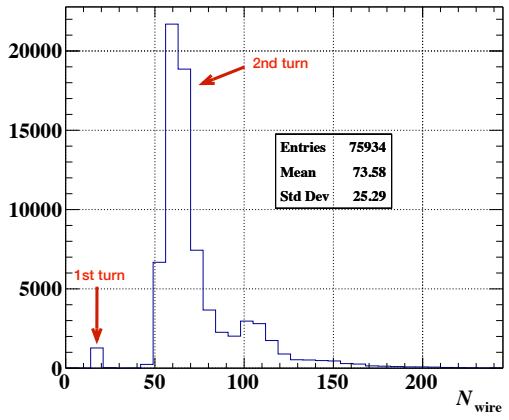

Figure 6.4: Number of hit wire cells before crossing the outer shell in the drift chamber.

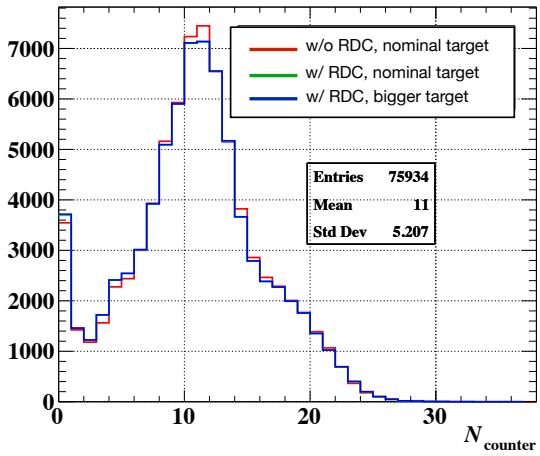

Figure 6.5: Number of hit tiles in the timing counter.

	I Drift Chamber	*II* Timing Counter	*I*×*II*
without RDC, nominal target	98.25 ± 0.05	95.33 ± 0.08	93.73 ± 0.09
with RDC, nominal target	97.65 ± 0.06	95.11 ± 0.08	92.99 ± 0.09
with RDC, bigger target	97.53 ± 0.06	95.09 ± 0.08	92.95 ± 0.09

Table 6.3: Efficiency for the signal positrons (%)

B. Hit rate in the drift chamber

Due to the high muon decay rate of $\sim 7 \times 10^7$ Hz, the positron spectrometer is operated in such a heavy irradiation environment. Particularly, there is a high positron hit rate ($\sim$1 MHz) in the inner most wire of the drift chamber, which is placed at $r = 18$ cm. The aging of the wire is thereby a potential issue. The previous study shows a yearly gain drop of $\sim$25% in the inner most wires [9]. If the beam spot becomes bigger, more positrons may hit the inner most wires. Therefore, the increase of the hit rate could be a problem.

To study on the hit rate in the inner most wire, Michel decay events were simulated on the target. The emission angle of the positron was isotropic. Figure 6.6 shows the distribution of hit wire ID in the drift chamber. Because it is uniformly distributed in the same layer, the average hit rate in each wire can be calculated by using the muon decay rate (7×10^7 Hz) and the number of wires (192 wires in a layer). The result is summarized in Table 6.4. The change with the bigger beam spot is +0.79% with either standard or bigger target. We concluded that the influence on the hit rate in the drift chamber would be negligibly small.

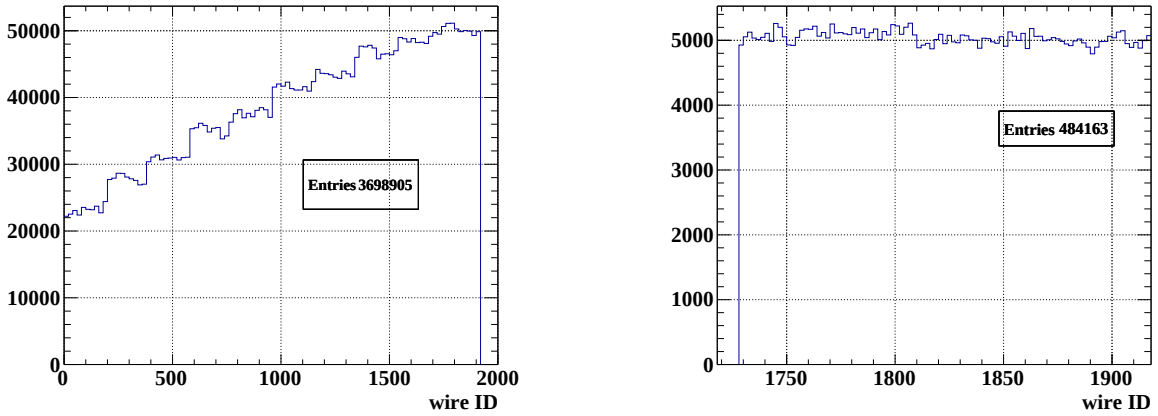

(a) Wires in the whole drift chamber

(b) Inner most wires

Figure 6.6: Distribution of the hit wire ID. The last 192 wires are corresponding to the inner most wires.

	hit rate (MHz)
without RDC, nominal target	1.765 ± 0.003
with RDC, nominal target	1.779 ± 0.003
with RDC, bigger target	1.779 ± 0.003

Table 6.4: Hit rate in the inner most wire

C. Reconstructed momentum resolution

The reconstructed momentum resolution with the drift chamber was estimated by simulating the signal events. Track fitting was performed by using an algorithm based on Kalman-filter developed for positron tracking in MEG. Figure 6.7 shows the difference of the reconstructed momentum and the true momentum in the simulation. The low momentum tail is corresponding to energy loss of positrons, which mostly comes from a bremsstrahlung of multiple scattering. The distribution was fitted with a double-gaussian where the reconstructed momentum resolution σ_{P} is expressed as sigma of the main peak. Table 6.5 summarizes the reconstructed

momentum resolution. In the upgrade proposal of the MEG II, the momentum resolution of ~ 130 keV was obtained [9]. We obtained the better resolution due to the improved track fitting algorithm, which can associate more hits to the track. Moreover, the contribution of the electronic is not considered in our simulation. As a result, the resolution changed by +1.30% with the bigger beam spot and the bigger target. We concluded that the reconstructed momentum resolution would not be significantly affected with the upstream RDC.

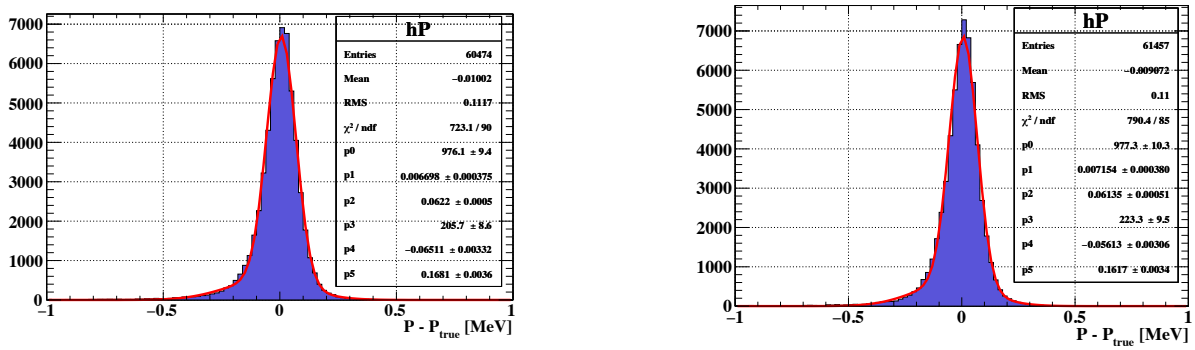

(a) without RDC, nominal target

(b) with RDC, bigger target

Figure 6.7: Difference of the reconstructed momentum and the true momentum in the simulation.

	σ_{P} (keV)
without RDC, nominal target	61.4 ± 0.4
with RDC, bigger target	62.2 ± 0.4

Table 6.5: Reconstructed momentum resolution

6.1.3 Muon stopping rate

Because it is difficult to measure the actual muon stopping test in the beam test, it was studied in the simulation. The muon beam of 28 MeV/c was generated in the simulation at the entrance of the beam transport solenoid. The muons were transported to the stopping target after passing the beam degrader and 190 μm thick vacuum window. A layer of the scintillation fibers was placed between the vacuum window and the target in the configuration with the upstream RDC. The stopping rate was calculated by counting the number of muon decay vertices inside a fiducial area of the nominal target. The muon beam intensity was assumed to be 10^8 μ/s.

Figure 6.8 shows the stopping rate in two configurations. The thickness of the degrader was changed with a step size of 10 μ m. The degrader thickness was optimized by maximizing the stopping rate in each configuration. Table 6.6 summarizes the stopping rate and the optimal degrader thickness. The change of the stopping rate is small (-0.54%) with the upstream RDC.

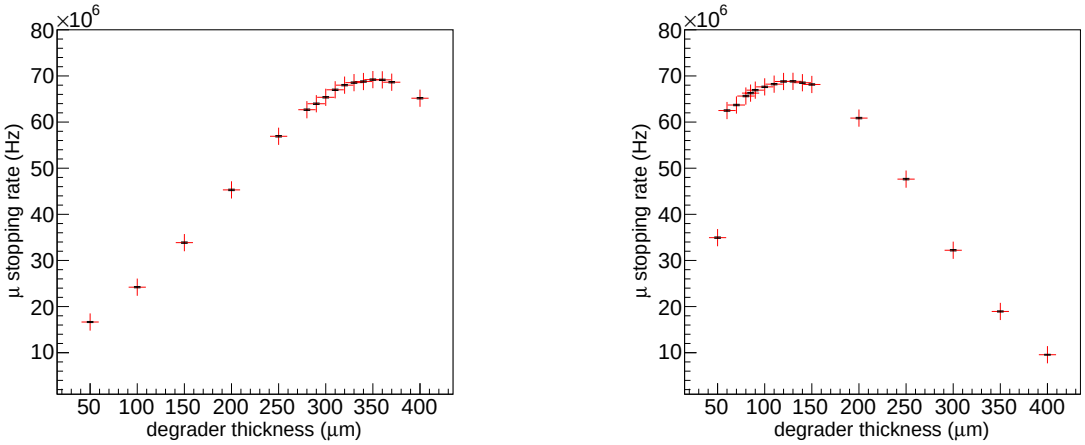

(a) without RDC (b) with RDC

Figure 6.8: Muon stopping rate with several degrader thicknesses.

	degrader thickness (μm)	Stopping rate (MHz)
without RDC	350	69.20 ± 0.16
with RDC	130	68.82 ± 0.14

Table 6.6: Optimal degrader thickness and muon stopping rate

6.2 Effect of pileup muon

Because of the high muon hit rate (∼500 kHz at the central fiber), the effect of the pileup is not negligible. In order to estimate the detector performance, the detection efficiency loss for the RMD positrons due to the pileup was studied. The inefficiency due to the pileup is estimated by calculating the following two factors. The first one is the capability to distinguish muon and positron pulses in the waveform analysis. The second one is the hit rate of muon and positron from RMD at each channel. The hit rate depends on the width of the fiber bundle and its position. In other words, the bundle widths can be optimized to minimize the inefficiency. Finally, section 6.2.4 presents several prospects to reduce the inefficiency due to the pile up.

6.2.1 Capability to distinguish two waveforms

As mentioned above, the inefficiency depends on the capability to distinguish muon and positron pulses in waveform analysis. Let us first define the minimum time difference to distinguish the muon and positron pulse as ΔT (Figure 6.9). To the first approximation, ΔT can be considered as a sum of muon and positron pulse widths. However, there are after-pulses of the SiPM associated with the main pulse. The muon waveform usually has a several after-pulses due to its large amplitude of the main pulse. Therefore, the pileup with these after-pulses needs to be also considered.

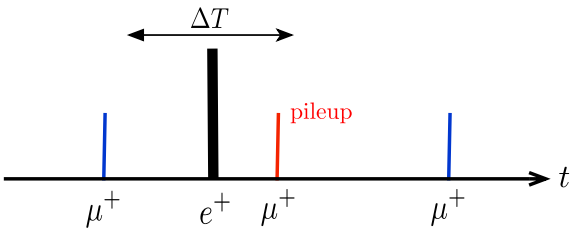

Figure 6.9: Definition of ΔT.

A. Data taking with a prototype

In order to measure actual ΔT, we acquired muon and positron waveform data individually at the πE5 beam line in PSI. The momentum of the beam particles were tuned to be 28 MeV/c.

The prototype detector consists of the scintillation fiber and SiPM (Figure 6.10). Square shape fiber with a size of 250 μm (Saint-Gobain, BCF-12) are placed with a pitch of 5 mm. The length of the fiber is about 20 cm. In order to reduce the light yields loss, the fiber is coated with a 100 nm aluminum. Because this is also a prototype of a two dimensional beam monitoring device, it has another perpendicular fiber layer. The scintillation light is collected at two fiber ends with 1.3×1.3 mm^2 SiPMs (Hamamatsu, S13360-1350CS). The fiber and SiPM are coupled with optical grease. The position of the fiber end is fixed on the PCB. Before data taking, the characteristics of all the SiPM were studied. The detail is described in appendix.

After cabling and light shielding, the detector was placed between the BTS and the steering magnet. The signal was transmitted to the WaveDREAM which was placed just in front of the detector. The waveform was acquired by triggering on a coincidence hit between the signals of two fiber ends.

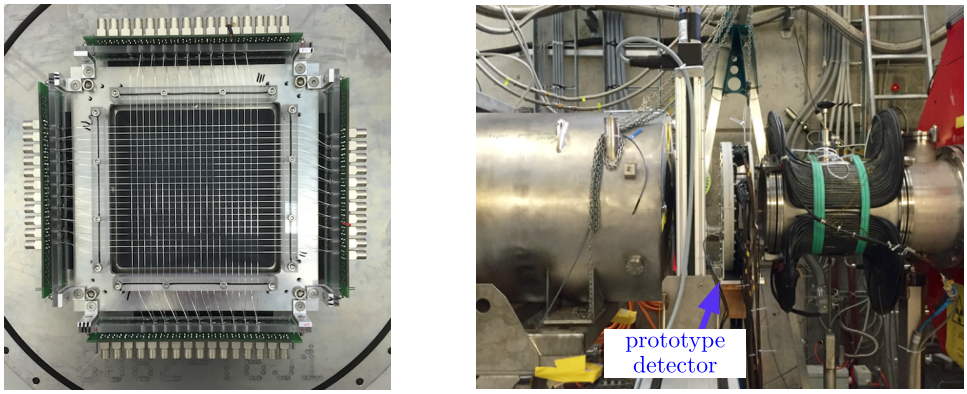

Figure 6.10: Prototype detector. Left : Fiber and PCB. Right : Detector at the measurement position after light shielding.

B. Waveform analysis

For each waveform, timing and amplitude of the pulse were calculated. ΔT was determined with following steps.

1. We first selected good sample waveforms. The waveform which has only one main pulse in the time window was selected. Examples of the selected waveforms are show in Figure 6.11 (a) and (b).

2. One positron and one muon waveform were randomly selected. The two waveforms were mixed by summing up amplitude data in a whole time window. The same positron waveform data was reused by shifting the timing by 20 ns so that we could obtain enough statistics.

   The example of the mixed waveform is shown in Figure 6.11 (c). By mixing waveforms, the noise level was increased by 54%.

3. The mixed waveforms were analyzed again. Timing and amplitude were calculated for each pulse.

4. According to the timing and amplitude information of the positron pulse before the mixing, the positron signal was searched for the corresponding timing (± 10 ns) and amplitude (± 10 mV) region.

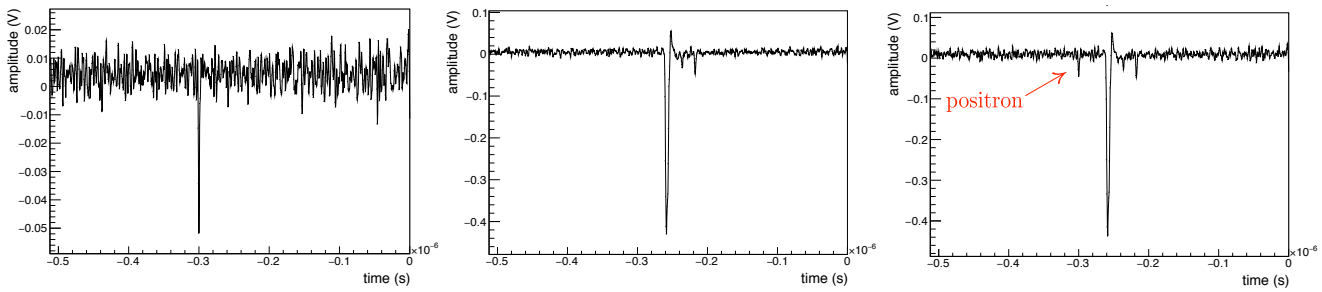

(a) Positron (b) Muon (c) Positron + Muon

Figure 6.11: Examples of waveform mixing.

Figure 6.12 shows the probabilities to find the positron signal in the mixed waveform. The decrease of the probability was observed for ∼120 ns around the region where the positron waveform overlaps muon waveform. Because of the noises, the probabilities are always below 100% even if there should be no pileup. The measured value is much larger than the sum of the positron and the muon waveform widths. This is because the after-pulses are generated only randomly after the main pulse, the positron signal could be detected even if it comes within 120 ns after the main pulse. However, in following sections, we consider the worst case where ΔT is 120 ns.

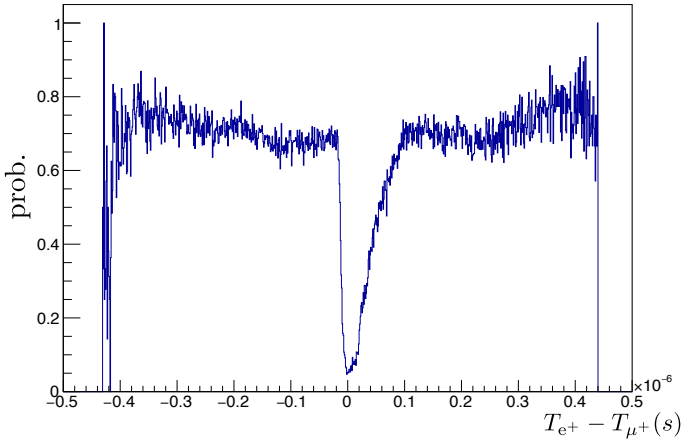

Figure 6.12: Probability to find a positron signal after mixing.

6.2.2 Effect of size and position of the fiber bundle

The hit rate of the beam muons and the positrons from RMD at each fiber bundle were obtained in a simulation study. Figure 6.13 shows the hit distributions in the upstream RDC. By using the hit rate and the value of ΔT, the probability of pileup can be calculated as :

$$\text{Probability} = \frac{\text{Number of pileup events}}{\text{Number of detected RMD events}}. \tag{6.1}$$

As previously mentioned, the probability depends on the width and position of the bundle. The probability will be larger if the bundle is placed near the beam axis (Figure 6.14). We assumed that the width of each bundle is square number of fibers (from 4 to 100) in order to efficiently fix at the end. The probabilities for all possible configurations were calculated as shown in Figure 6.15.

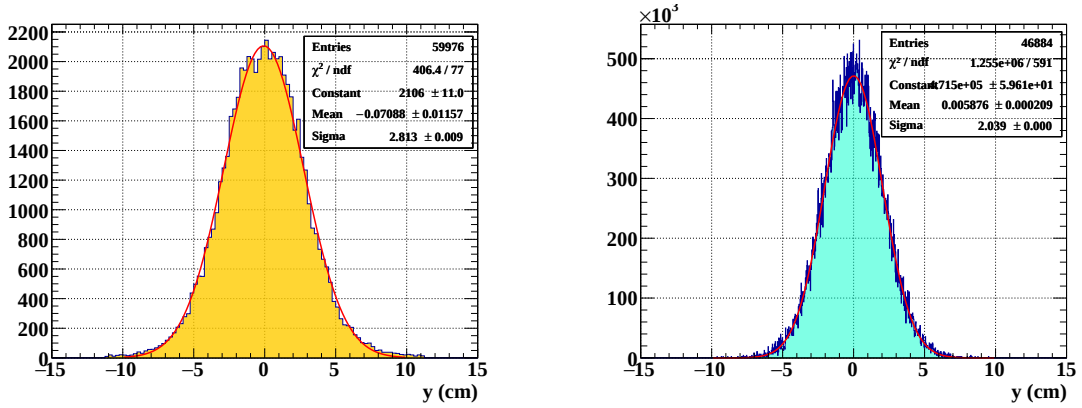

(a) Positron from RMD ($E_\gamma > 48$ MeV) (b) Beam muon

Figure 6.13: Hit distribution in the upstream RDC.

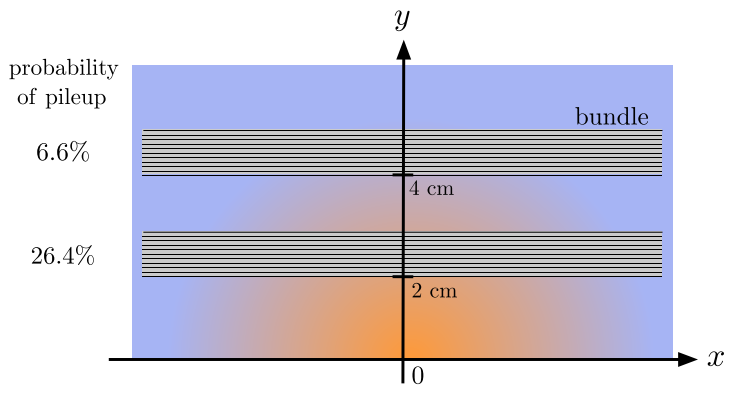

Figure 6.14: Example of the probability of the pileup in two different positions (9 fibers bundle, $y = 2$, 4 cm). The orange area represents the high muon hit rate region.

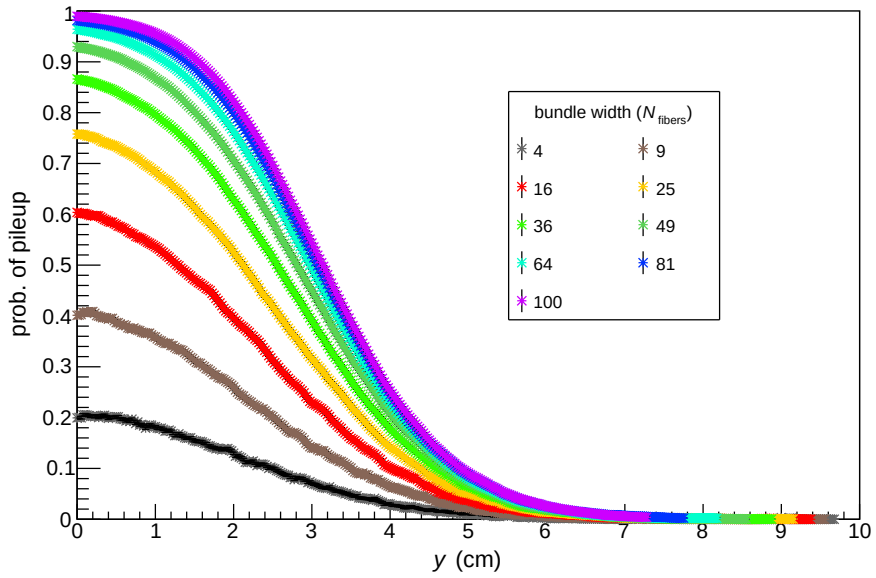

Figure 6.15: Probability of the pileup calculated with a step size of 250 μm

6.2.3 Total inefficiency for RMD positrons of all bundles

The inefficiency due to the pileup was calculated by integrating the probability of the pileup over the whole detector. We estimated the inefficiency by assuming following two conditions.

- Total y length of the upstream RDC is within 19.6 $\pm$ 0.25 cm.
- The maximum number of bundles is 18 due to the limitation of the space for the SiPMs.

There are over a thousand configurations of the bundle widths, which satisfy above conditions. We calculated the inefficiency for all these possible configurations as shown in Figure 6.16. Table 6.17 shows the best configuration of the bundle width, which minimizes the inefficiency. The inefficiency due to the pileup is 50.4% with the best configuration.

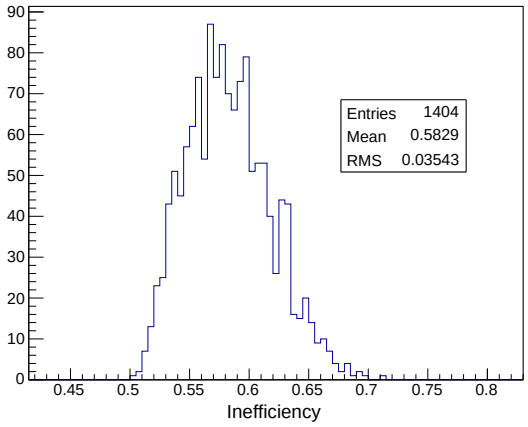

Figure 6.16: Distribution of the inefficiency for the RMD positrons.

Bundle width	N_{bundle}
100	4
49	2
36	2
25	2
16	8

Figure 6.17: Best configuration of the bundle width. Smaller widths are used in more central regions of the detector.

6.2.4 Prospects for reducing the inefficiency

The inefficiency due to the pileup is large even by using the best bundling configuration. In order to reduce the inefficiency, several possibilities are being considered. The first idea is to increase the total number of bundles as shown in Figure 6.18. This might be possible by modifying the detector layout. The second idea is to make a probability density function related to the after-pulse and implement it in likelihood analysis of MEG II. In provisional estimation, we assumed that the after-pulses are always present in the timing region of 120 1mmns. Therefore, further reduction of the inefficiency is possible by taking into account that the after-pulses are generated only randomly after the main pulse. In order to construct a probability density function, the characteristic of the after-pulse needs to be fully understood. The third idea is to use a staggered readout as shown in Figure 6.19. The inefficiency due to the pileup can be reduced by using this method. However, a high light yield at the single side is required to efficiently detect a positron signal.

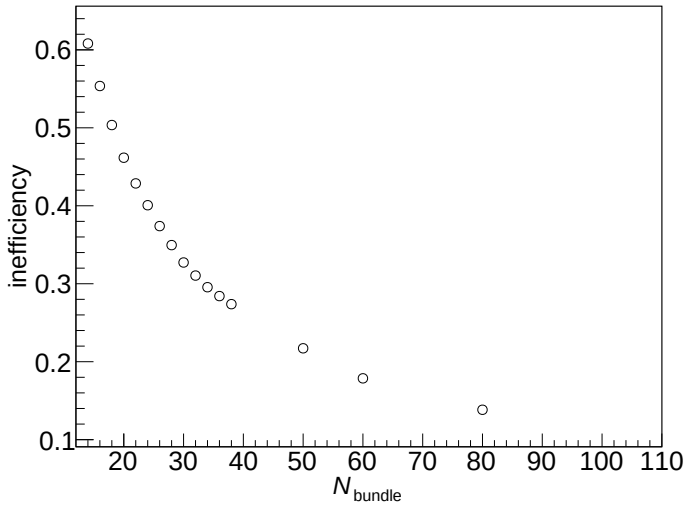

Figure 6.18: Total number of bundles and inefficiency for RMD positrons with the best bundling configuration.

(a) standard readout (b) staggered readout

Figure 6.19: Principle of the staggered readout. When there is a pileup event in the same bundle in (b) it is distinguishable in the right side of the SiPM.

6.3 Total detection efficiency for RMD positrons

Based on the studies in the previous sections, we next evaluated the detection efficiency for the RMD positrons. When the position enter the acceptance of the detector, the signal could not be detected due to following reasons.

A The positron goes through a fiber cladding and does not hit a fiber core.

B There is a pileup of beam muon.

C No scintillation photons are detected due to the small light yields of the scintillating fiber.

According to the catalog [22], the cladding of the 250 μm thick square shaped fiber is 5% (first cladding 3%, second cladding 2%). Therefore, we can assume that the probability of *A* is about 10% and the efficiency has to be calculated by considering mainly *B* and *C*.

6.3.1 Light yield of the scintillating fiber

The light yields of the positrons that we obtained in the prototype beam test is shown in Figure 6.20. If we assume that the number of the photoelectrons follows the Poisson distribution, the probability to detect no photoelectron can be calculated as 29%. By taking into account this, the mean of the number of photoelectrons is estimated to be about 1.2.

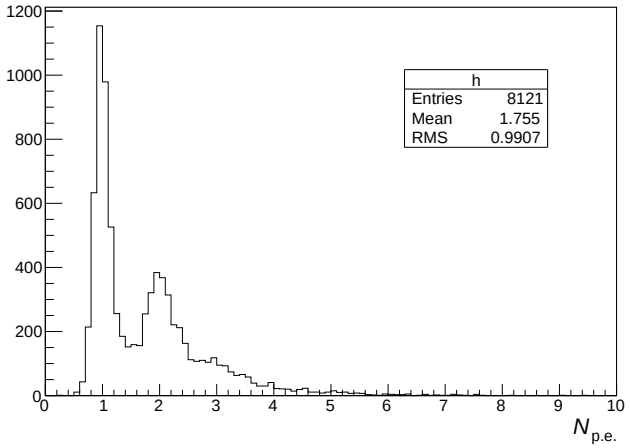

Figure 6.20: Distribution of the number of the photoelectrons observed at single side.

However, this value could not be realistic because we used the positron beam with the different momentum. Moreover, the optical coupling of the scintillating fibers and the SiPMs could be optimized. Therefore, we calculated the ideal number of the scintillation photons at fiber ends when the positron from RMD penetrates the center of the square shaped fiber. Following conditions were taken into account.

- Energy deposit of the positrons from RMD is ~ 38.5 keV (Figure 6.21).
- Light yields of the fiber is 8000 photons at 1 MeV [22].
- The photons are lost if their incidence angles to the cladding wall are less than 78.6° [22] (Figure 6.22).
- Attenuation length of the scintillating fiber is ~ 20 cm.
- Photon detection efficiency of the SiPM is 40% [16].

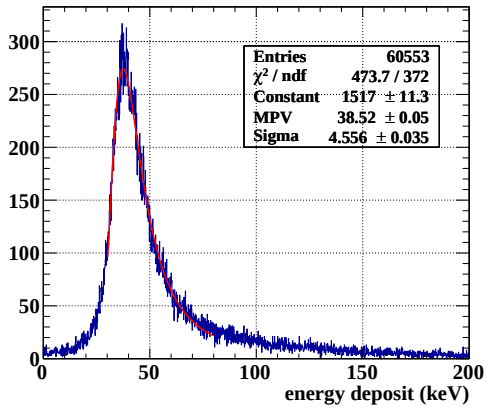

Figure 6.21: Simulated energy deposit of the positrons from RMD ($E_\gamma > 48$ MeV).

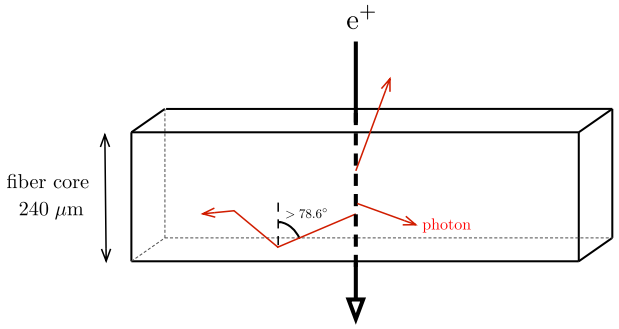

Figure 6.22: Schematic view of the transmission of the scintillation photons.

We calculated the number of photons event by event with above conditions by assuming that the emission angles of the scintillation photons were isotropic. The reflections at the cladding wall were calculated until the photon was reflected twice. This was because even if the photon was reflected at the cladding wall once, it could not be reflected at the vatical wall. As a result, about 4.3 photons were obtained on average at single side (Figure 6.23). It is known that attenuation length of the scintillating fiber has both short (15-60 cm) and long (1 m$\sim$) components. However, the short component, which largely affect the light yields, has not been precisely measured. Therefore, the result of the light yield calculation has a large uncertainty ($\sim$ 40%).

Because of the uncertainty of the light yields, it was calculated in different configurations. Based on the ideal case (4.3 photons at the single side), the other cases with smaller light yields were calculated with additional factors. The range of the factors is from 0.2 to 1.0 and it scaled the probabilities to detect a signal event by event. In the real case ($\sim$ 1.2 photons at the single side), the factor is about 0.3.

Figure 6.24 shows the probability to detect a signal at least one photon with the SiPMs. The probability to detect at the single side is written as P_{Single}. P_{OR} represents the probability to detect a signal at the either side of the fiber. P_{AND} represents the probability to detect a signal at both ends. If we use both fiber sides, the signal can be efficiently detected even if the mean light yields at the single side is small such as $\sim$1.2. However, the light yield or the attenuation could be degraded due to the radiation damage. Currently, irradiation test of the scintillating fiber is being planned at PSI in order to measure the effect.

6.3.2 Detection efficiency and sensitivity in different configurations

Next, the detection efficiency was calculated in several configurations of the light yields. The standard readout and staggered readout were compared in terms of the efficiency. In addition to the probabilities shown in the previous section, the effect of the pileup muons was also taken into account. By assuming the muon hit rate of $\sim 10^8$ Hz, the muon hit bundles and the timing were simulated. The hit bundles were decided by the position distribution, which was obtained in the simulation study (Figure 6.13). As described in section 6.2.3, we considered the case that the bundle widths were optimized to minimize the inefficiency due to the pileup, where the number of the bundles is 18. The efficiency was defined as :

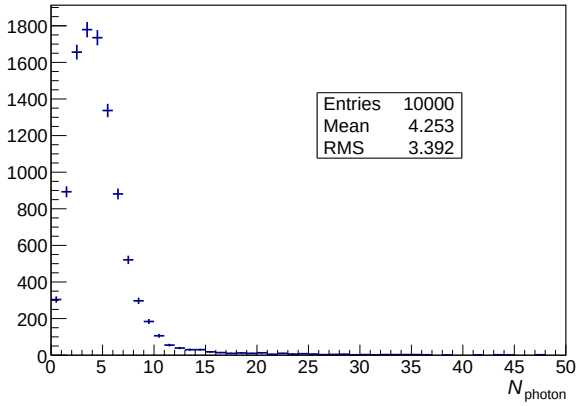

Figure 6.23: Calculated number of scintillation photons at the single side. The probability to detect no photons is also included in the first bin.

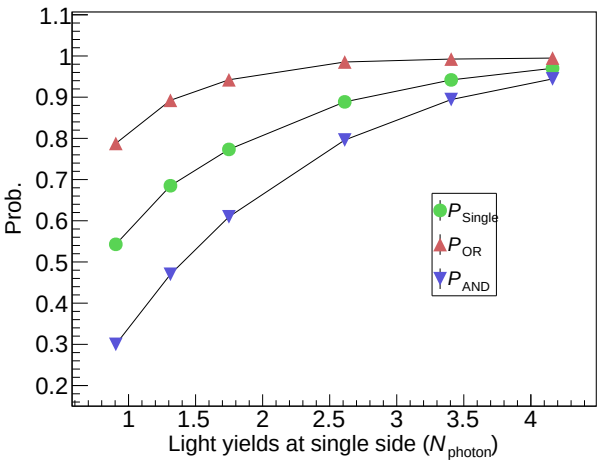

Figure 6.24: Light yields and the probabilities to detect a signal with the SiPMs.

$$\text{Efficiency} = \frac{\text{Number of detected events by the SiPMs (either side)}}{\text{Number of entered positrons in the upstream RDC}}. \tag{6.2}$$

In principle, the efficiency can be calculated by using the probabilities which were shown in Figure 6.24. However, the probability that we should consider (P_{Single} or P_{OR}) depends on the hit position and timing patterns of the muon. Following section describes how the efficiencies can be calculated in either standard or staggered readout.

Standard readout

In the standard readout, we can consider the muon hit patterns as shown in Figure 6.25. In the simulated RMD positron hit event, we first checked if there was a muon hit within $\Delta T = 120$ ns in the whole detector. If there was no muon hit within ΔT, we regarded the probability to detect a signal as P_{OR}. Actually, 99.7% of the RMD positron hit events had at least one muons within ΔT. For these case, we next checked the hit bundle of the muons. If there was no pileup muon in the same bundle, we regarded the probability as P_{OR}.

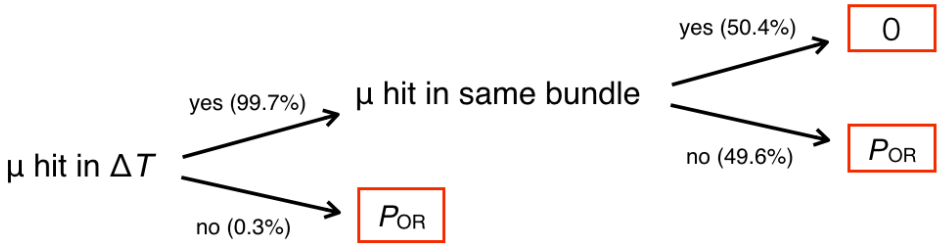

Figure 6.25: Hit patterns of the muon in the standard readout. The probabilities to detect a signal are shown in the red boxes. The fraction of each conditional branch is also shown.

Staggered readout

The muon hit patterns in the staggered readout is more complicated than that in the standard readout (Figure 6.26). When there is a muon hit within $\Delta T = 120$ ns in the whole detector, we can consider four hit position patterns as illustrated in Figure 6.27.

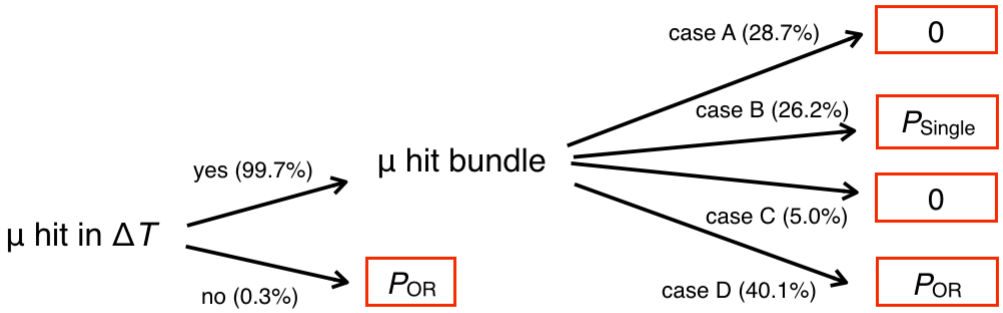

Figure 6.26: Hit patterns of the muon in the staggered readout. Details of the hit position patterns are shown in the next figure.

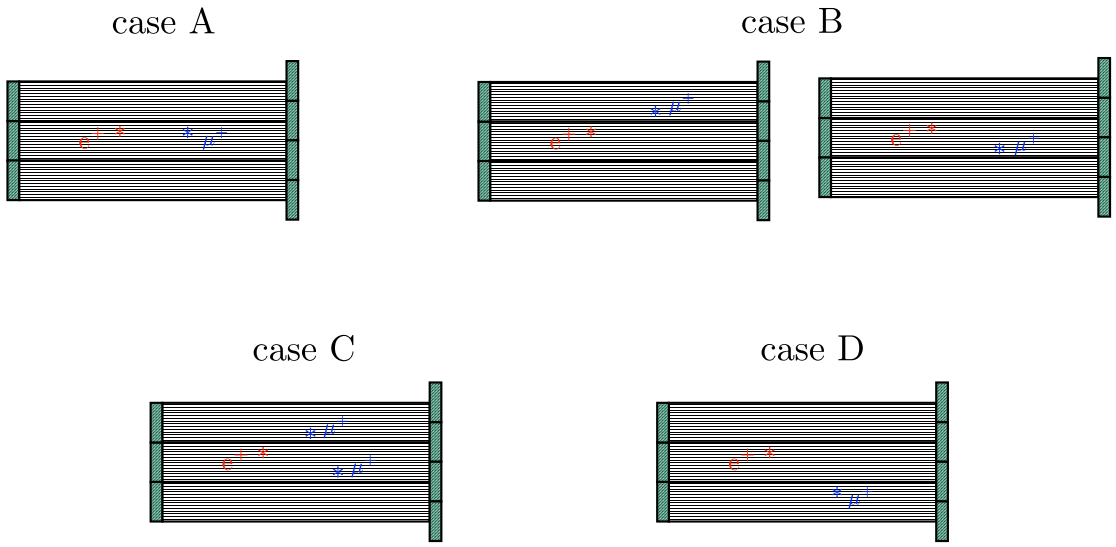

Figure 6.27: Four hit position patterns when there are muon hits within ΔT. Case A, C : Positron cannot be detected at both ends. Case B : Positron can be detected only at one end. Case D : Positron can be detected at both ends.

Figure 6.28 compares the efficiency for the RMD positrons with the different light yields between the standard readout and the staggered readout. Given the fact that the staggered readout can reduce the effect of the pileup (Figure 6.19), its total efficiencies are superior to that of the standard readout.

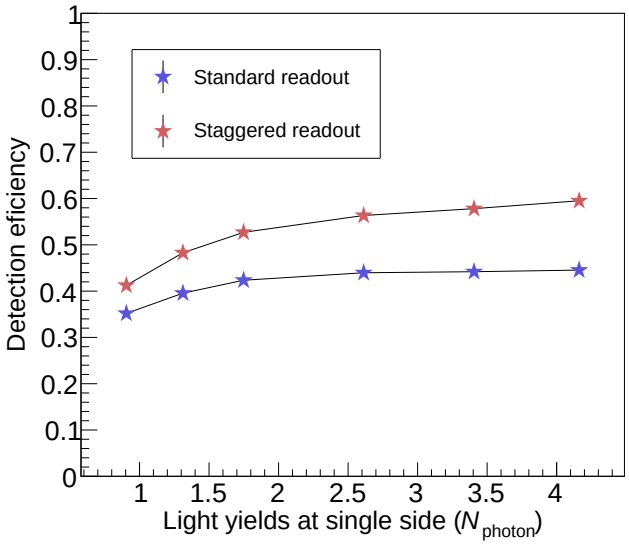

Figure 6.28: Expected detection efficiency for the RMD positrons.

Based on the calculated detection efficiency, we finally estimated the MEG II sensitivity with the upstream RDC. Previously, the sensitivity was calculated by making an ensemble of pseudo experiments to to extract the upper limit at 90% C.L. in three years data taking. If the upstream RDC is not installed, the sensitivity will be 4.3×10^{-14}. On the other hand, if the upstream RDC is installed and the detection efficiency is 100%, the sensitivity will be 3.9×10^{-14}. The sensitivity including the efficiency loss was calculated by assuming that the sensitivity becomes worse depending on the number of the remaining background events. Approximately, the change of the sensitivity is in proportion to the square root of the number of the remaining background events. Figure 6.29 shows the estimated sensitivities with above assumption in several configurations of the light yields.

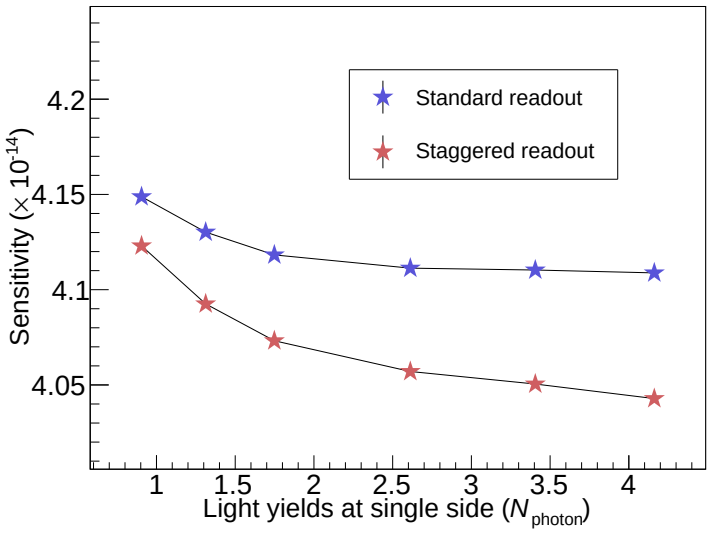

Figure 6.29: Expected sensitivity of the MEG II experiment.

Chapter 7

Summary and Outlook

7.1 Radiative Decay Counter

The Radiative Decay Counter is one of the key detectors of the MEG II experiment. It identifies the dominant source of the background photons from RMD by detecting time-coincident low momentum positrons. Two detectors are installed on the beam axis at both the downstream and the upstream of the stopping target. According to the simulation study, 41% of total background photons can be identified and thus the sensitivity is improved by 22% if both the downstream and the upstream detectors are installed. The installation of the downstream RDC detector was approved by the collaboration and the construction was already finished. The first commissioning was successfully performed by using a high intensity muon beam. Based on the issues revealed in the commissioning, the optimization of the downstream detector is in progress toward the final installation. The installation of the upstream detector has not been approved yet because it requires additional R&D concerning the operation in the muon beam. A series of studies has been performed in various ways as summarized in the following sections.

7.2 Downstream detector

We started from optimizing the calorimeter, which consists of the LYSO crystals and SiPMs. Performances of all the LYSO crystal was checked and we obtained the good energy resolution of $\sim 6\%$ for all channels. On the other hand, we observed afterglow of the LYSO crystals, which could affect the energy resolution. By studying with a room light and β-ray source, we concluded that the influence on the energy resolution would be small. We also optimized the optical coupling of the crystals and the SiPMs. By comparing the light yields of the crystal, we concluded that the coupling with grease is the best.

The first commissioning of the constructed detector was performed by using a high intensity muon beam and a BGO photon detector. The detector installation with the moving arm, trigger and DAQ were tested. The calibration of each detector was performed before the data taking. By triggering on the hit in the BGO detector, we observed a clear timing peak of the RMD events after event selections. Although the commissioning was successfully accomplished, few issues were found at the same time. Due to the discrepancy of the two calibration results of the BGO detector, we could not quantitatively evaluate the capability of the background identification. The cause has not been fully understood yet. In addition, we found that the connection of the PCBs and SiPMs in the timing counter were very fragile. Due to this, we

could not detect the signals in four channels. However, we can improve the mechanical strength with the reflow soldering.

Towards start of the physics data taking of MEG II, we will fix all the issues found in the commissioning. All the timing counters will be reassembled with the reflow soldering instead of the conductive epoxy. We are also going to prepare some spare counters so that we can quickly replace even if some problematic channels are found. Moreover, the detector layout will be modified in order to have a sufficient clearance for the movement of the detector.

For further quantitative analysis of the data acquired in the first commissioning, it is necessary to understand the correct energy scale of the BGO detector. We will check the linearity of each component such as the BGO crystal and the PMT.

7.3 Upstream detector

First, the influence on the muon beam was studied with a mockup RDC. The increase of the spot size was measured to be 16%. However, according to the simulation study, the increased beam spot does not significantly affect the performance of the positron spectrometer. The efficiency loss for the signal positron is less than 1% and the momentum resolution would not be changed. Moreover, the loss of the muon stopping rate would be less than 1%.

Another potential issue is the detection efficiency loss for the RMD positrons due to the pileup muons. Because there are after-pulses of the SiPM associated with the main pulse of the muon, the effect of the pileup with these after-pulses was also considered. In order to measure the minimum time difference to distinguish the muon and positron waveform (ΔT), we acquired each muon and positron waveform data by using a prototype detector. By mixing two waveforms randomly and analyzing it, ΔT was estimated to be 120 ns. The inefficiency due to the pileup was calculated with ΔT and the expected hit rate of muon and positron from RMD at each bundle, which was obtained in the simulation study. The configuration of the bundle widths was also optimized to minimize the inefficiency. Due to the high muon hit rate (~ 500 kHz at the central fiber) and large ΔT, the inefficiency is large ($\sim 50\%$) even by using the best bundling configuration. However, a further reduction of the pileup is possible in several ways.

We finally calculated the total detection efficiency for the RMD positrons and the sensitivity. Because the light yield of the scintillating fiber has not been completely understood yet, the efficiency was estimated with several possible configurations.

In order to evaluate the light yields more accurately, the attenuation length of the fiber is being measured. After the measurement, we will be able to calculate the efficiency and evaluate the sensitivity. Moreover, light yields loss due to the radiation damage has to be investigated. For this purpose, the irradiation test of the scintillating fiber is planned at PSI.

7.4 Outlook

The engineering run of the MEG II experiment is expected to start in 2017, which will be followed by the physics data taking. The downstream detector will be installed by fixing all the issues which were found in the commissioning. The performance evaluation of the upstream detector will be finished in this year, including the irradiation test and the attenuation length measurement of the scintillating fibers. After that, we will propose to install the upstream detector, and as soon as it is approved by the MEG II collaboration, we will start the construction. The MEG II experiment is expected to reach the sensitivity goal of $\sim 4 \times 10^{-14}$ after

three years data taking with both RDC detectors.

Appendix A

Characterization of SiPM

This chapter reviews the basic properties of the SiPM and introduces several measurements which were performed by using a S13360-1350CS from Hamamatsu Photonics. This SiPM was used in the prototype of the upstream RDC (Figure A.1). It has a small active area of 1.3×1.3 mm^2 and the crosstalk probability is suppressed compared to the previous model (S12825-050C). The basic properties are summarized in Table A.1. Although a lot of the SiPMs are mounted on the PCB, one of the SiPM was used in all of the following measurements.

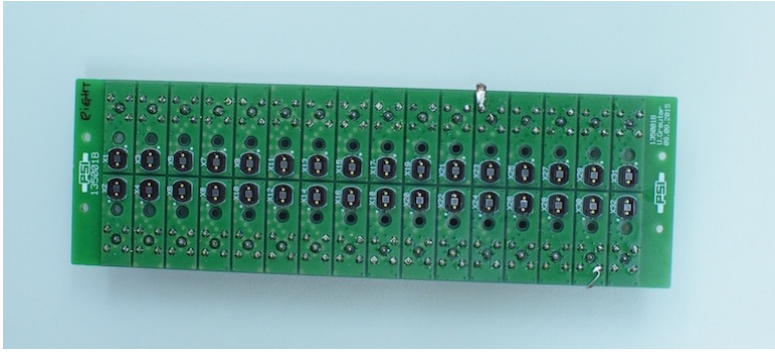

Figure A.1: PCB with 36 SiPMs.

Pixel pitch	50 μm
Breakdown voltage	53 ± 5 V
Photon detection efficiency	40%
Gain at V_{OP}	1.7×10^6
Fill factor	74%
Dark rate at V_{OP}	$90 \sim 270$ kcps
Crosstalk probability at V_{OP}	1%
Temperate coefficient	54 V/°C
Terminal capacitance	60 pF

Table A.1: Basic properties of S13360-1350CS [16]. V_{OP} is breakdown voltage + 3.0 V. The measurements were performed at 25 °C.

A.1 Principle of photon detection

The SiPM is a semiconductor photodiode in which multi-pixels are connected in parallel. Each pixel is operated in "Geiger mode" with the bias voltage which is larger than the breakdown voltage. This causes an avalanche signal and enables to detect photons at very low light level from a single photon. As illustrated in Figure A.2, each pixel has a structure of the p-n junction. When a photon hits the active area of the pixel and its energy is higher than the band gap energy, an electron is excited into the conduction band and thus it produces an electron-hole pair. The electron is accelerated with the bias voltage toward the avalanche region where the higher bias voltage is applied. When the energy of the election is large enough, it triggers an avalanche of the further electron-hole pair creations. Once the avalanche starts, the current of the quenching resistance starts to increase and the voltage of the pixel starts to go down. The avalanche stops when the bias voltage becomes below the break down voltage.

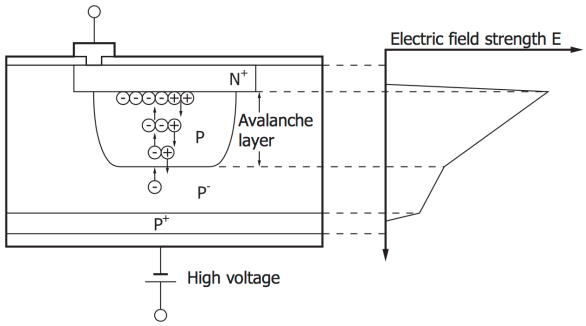

Figure A.2: Schematic diagram of avalanche multiplication [23].

A.2 Current-Voltage curve

Measuring a current-voltage curve (I-V courve) is one of the important characterization of the SiPM in order to extract parameters such as breakdown voltage or quenching resistance. The measurement was performed by using a picoammeter (Keithley, 6485) and recording software (LabView). The temperature was kept at 24 °C with a thermal chamber. Figure A.3 shows the measured I-V curves in both negative and positive bias voltage regions.

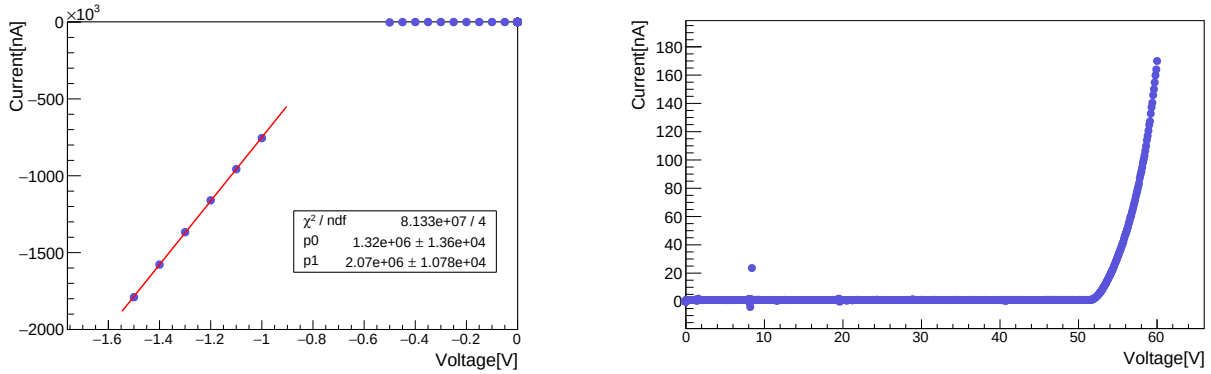

Figure A.3: I-V curve of the SiPM. Left : Negative bias voltage. Right : Positive bias voltage. Due to the current limitation, we did not use the software below −1 V, but we read the value on the display of the picoammeter.

When we apply the negative bias voltage which corresponds to the forward voltage, we can measure the quenching resistance of each pixel from the slope. In Figure A.3, the quenching resistance was measured to be 322.2 kΩ. Moreover, the recovery time of the pixel can be calculated as a product of the combined quenching resistances of all the pixels and the terminal capacitance. It was measured to be 29 ns. By applying the positive bias voltage, we can extract the breakdown voltage of the SiPM (Figure A.4). The curve was fitted with two functions independently and we can extract the breakdown voltage at the crossing point. For example in Figure A.3, the breakdown voltage was measured to be 51.5 V which is equivalent to that in the spec sheet.

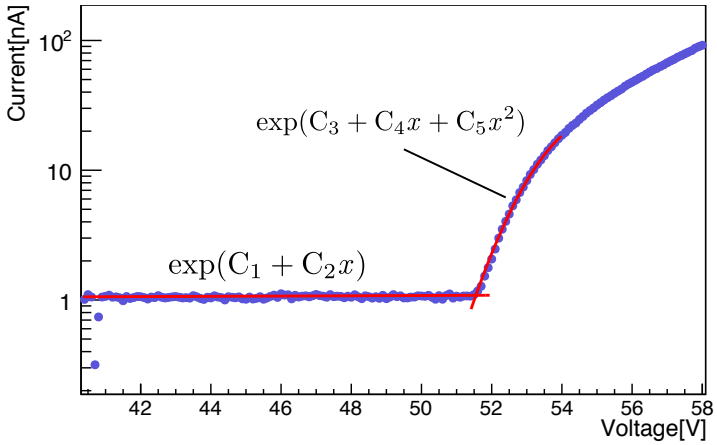

Figure A.4: Example of fitting I-V curve.

A.3 Dark noise

The electron-hole pair is not only created by the incident photon, but it is also thermally generated. It triggers the avalanche and induces an undistinguishable signal from the photon signal. This is called a dark noise. Although the dark noise is induced randomly, the rate of the dark noise is related to the temperature and the bias voltage. Figure A.5,A.6 and A.7 show the results of the dark rate measurements with different configuration. It was measured by using a discriminator (PHILIPS, 708), scaler (CAEN, Mod. M145) and 30 dB pre-amplifier which was developed in PSI. The temperature was controlled with a thermal chamber.

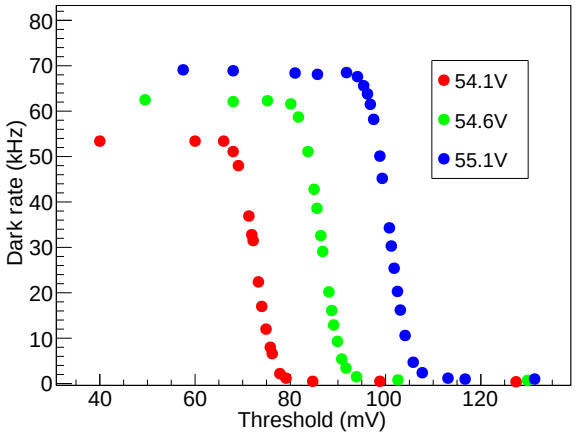

Figure A.5: Dark rate vs. threshold of the discriminator with different bias voltages (at 24 °C).

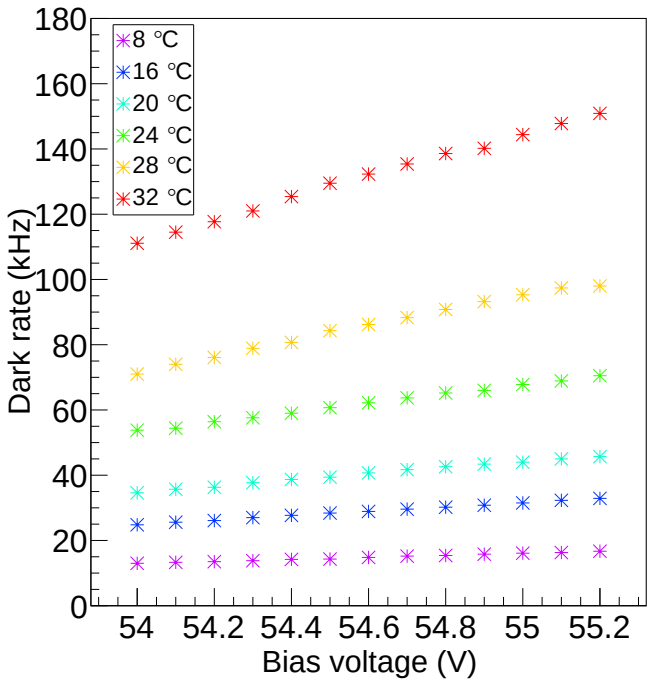

Figure A.6: Dark rate vs. bias voltage with different temperatures. The threshold of the discriminator was always set to the signal amplitude of the half photoelectrons.

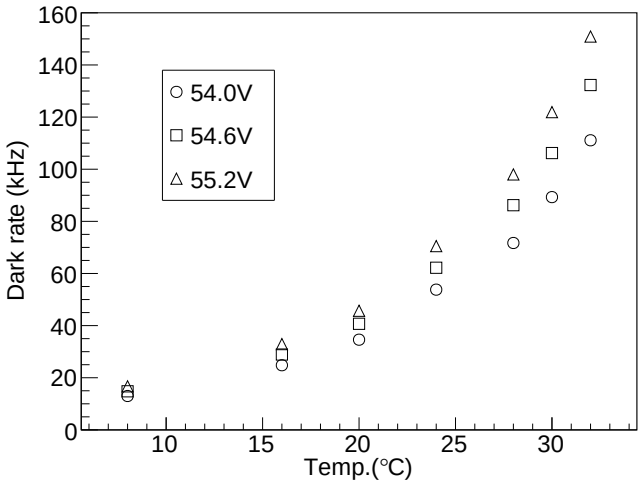

Figure A.7: Dark rate vs. temperature with different bias voltages.

A.4 Crosstalk and after-pulse

A crosstalk and an after-pulse are also important characteristics of the SiPM. The crosstalk is occurred when a triggered pixel induces an avalanche in neighboring pixels. In the S13360-1350CS, the crosstalk probability is suppressed in the S13360-1350CS by inserting an isolation trench between the pixels. On the other hand, the after-pulse is occurred when a carrier in the primary avalanche is trapped and released after quenching.

The upper limit of the probability to induce the crosstalk and after-pulse can be measured by acquiring the spectrum of the dark noise. Figure A.8 shows the charge spectrum which

was acquired with a DRS evaluation board in the room temperature. The upper limit can be calculated as :

$$\text{Probability} = \frac{\text{Fraction of } > \text{ 1.5 p.e.}}{\text{Fraction of } > \text{ 0.5 p.e.}}. \tag{A.1}$$

Note that the probability of the accidental coincidence of the dark signals is also included in the definition. It was calculated to be about 1.3%.

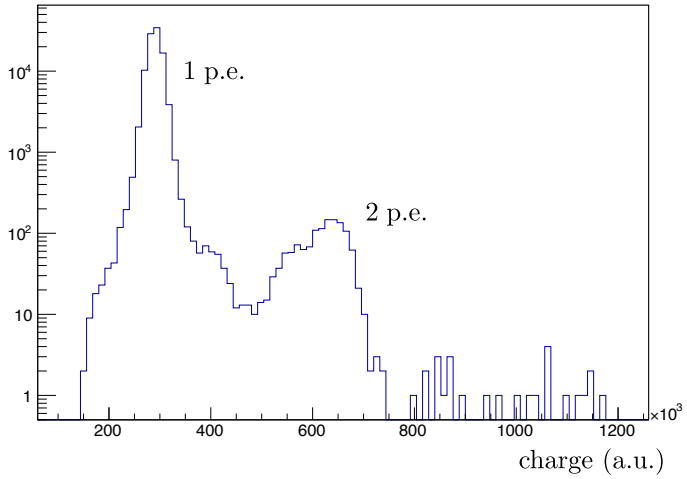

Figure A.8: Spectrum of the dark noise.

A.5 Gain

Thanks to the operation with Geiger mode, the SiPM obtains a high gain which enables the photon counting. We measured the gain with different bias voltages and temperatures by acquiring the charge spectrum. In principle, the gain can be calculated as the distance of two photo-peaks in the spectrum. However, it is difficult to use the dark spectrum because the fraction of the second or third photo-peak is very small. Therefore, we used a LED and pulse generator (TTI, TGP100-10 MHz) to collect actual photons. The waveform data was acquired with the DRS evaluation board by triggering on the synchronization signal of the pulse generator. An example of the spectrum is shown in Figure A.9. By fitting first two photo-peaks, the gain was calculated. Figure A.10 shows the gain which was measured with different bias voltages and temperatures. The fluctuation at the high temperature probably comes from the fluctuation of the temperature.

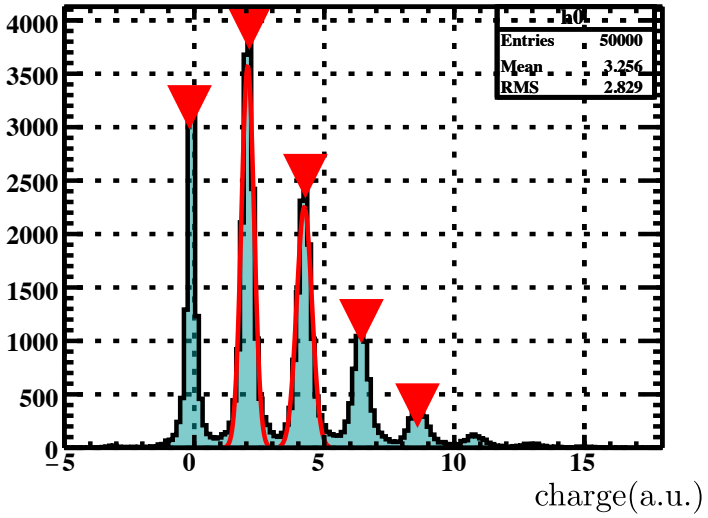

Figure A.9: Measured spectrum at 24 °C. The bias voltage is 53.9 V. The left peak corrrenponds to a pedestal.

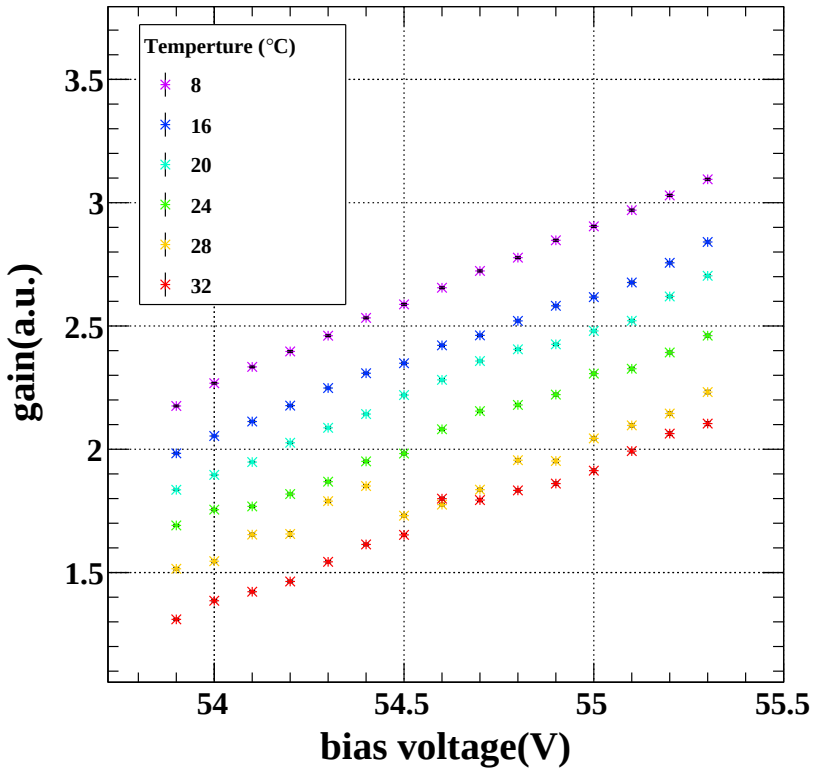

Figure A.10: Gain vs bias voltage with different tempertures.

Bibliography

[1] ATLAS Collaboration, "Observation of a new particle in the search for the Standard Model Higgs boson with the ATLAS detector at the LHC", Phys.Lett. B716 (2012) 1-29

[2] CMS Collaboration, "Observation of a new boson at a mass of 125 GeV with the CMS experiment at the LHC", Phys.Lett. B716 (2012) 30-61

[3] Particle Data Group, "Review of Particle Physics", Chin. Phys. C, 40, 100001 (2016)

[4] F. Boehn and P. Vogel, "Physics of Massive Neutrinos", Cambridge Univerity Press, 1992 (2012)

[5] S. Antusch, E. Arganda, M.J. Herrero and A.M. Teixeira, J. High Energy Phys. 11 (2006) 090

[6] Baldini, A.M., Bao, Y., Baracchini, E. et al., "Search for the lepton flavor violating decay $\mu^+ \to e^+\gamma$ with the full dataset of the MEG experiment", Eur. Phys. J. C (2016) 76: 434.

[7] S. Antusch, E. Arganda, M.J. Herrero and A.M. Teixeira, J. High Energy Phys. 11 (2006) 090

[8] A. M. Baldini et al, "MEG Upgrade Proposal", arXiv:1301.7225 (2013)

[9] W. Ootani, "An Experimental Review of Charged Lepton Flavor Violation in Muon Channel", J. Phys. Soc. Jpn., Vol.85, No. 9 (2016)

[10] https://www.psi.ch/rf/hipa

[11] https://www.psi.ch/num/facilities

[12] Stefan Ritt et al, "Application of the DRS Chip for FastWaveform Digitizing", Nucl. Instr. Meth. A 623, 486-488 (2010)

[13] Y. Fujii, "Development of Radiative Decay Counter to reduce the background in the MEG experiment", IEEE NSS (2013)

[14] S. Nakaura, "Development of Radiative Decay Counter for ultimate sensitivity of MEG II experiment", Master Thesis, the University of Tokyo (2016)

[15] Saint-Gobain BC418-420-422 data sheet (http://www.crystals.saint-gobain.com/products/BC418-BC420-BC422-BC422Q)

[16] Hamamatsu Photonics, S13360-3050PE data sheet (2016) (http://www.hamamatsu.com/jp/en/S13360-3050PE.html)

[17] Shanghai Institute of Ceramics, LYSO crystal data sheet
(http://www.siccas.com/LYSOScintillatorCrystal.htm)

[18] Saint-Gobain, PreLudeTM 420 data sheet
(http://www.crystals.saint-gobain.com/products/prelude-420-LYSO)

[19] Chen, Jianmin et al., "Large size LSO and LYSO crystals for future high energy physics experiments", IEEE Trans.Nucl.Sci. 54 (2007) 718-724

[20] E. Browne, Huo Junde, NDS 84, 337 (1998).

[21] Hamamatsu Photonics, PMT handbook (2007)
(https://www.hamamatsu.com/resources/pdf/etd/PMT_handbook_v3aE.pdf)

[22] Saint-Gobain, Scintillating fiber data sheet
(http://www.crystals.saint-gobain.com/sites/imdf.crystals.com/files/documents/fiber-brochure.pdf)

[23] Hamamatsu Photonics, Semiconductor handbook, chapter3
(https://www.hamamatsu.com/resources/pdf/ssd/e03_handbook_si_apd_mppc.pdf)

Acknowledgements

First of all, I would like to thank my supervisor, Prof. Wataru Ootani for supporting me all the time. I am really delighted to keep studying under his supervision in the future. I would like to thank Prof. Toshinori Mori for giving me an opportunity to join the MEG II experiment. I am heartily thankful to the people in the team RDC for guiding my work with detailed advices. I learned so many things from Dr. Ryu Sawada and Dr. Kei Ieki. I would like to thank Mr. Shota Nakaura for inviting me to the MEG II experiment and the team RDC. I am very grateful for the people in the scintillating fiber group, especially, Dr. Angela Papa, Dr. Emanuele Ripiccini and Ms. Giada Rutar for giving me an opportunity to study in their group. I would like to thank all the MEG II collaborators, especially, Dr. Toshiyuki Iwamoto, Dr. Yusuke Uchiyama, Dr. Peter-Raymond Kettle, Dr. Malte Hildebrandt, Dr. Daisuke Kaneko, Mr. Felix Berg, Ms. Miki Nishimura, Mr. Shinji Ogawa, Mr. Kohei Yoshida, and Mr. Mitsutaka Nakao, for a great help. I would like to thank Mr. Naoya Shibata for giving me a lot of advices. I also thank to all friends in Switzerland for helping me a lot in a daily life. Finally, I am deeply thankful to my family for supporting me all the time.